Title	Study of Optimized Helical Axis Stellarators(Dissertation_)
Author(s)	Yokoyama, Masayuki
Citation	Kyoto University ( )
Issue Date	1996-07-23
URL	http://dx.doi.org/10.11501/3117177
Right	
Type	Thesis or Dissertation
Textversion	author

Study of Optimized Helical Axis Stellarators

Masayuki Yokoyama

1996

Abstract

In this thesis, optimization of the helical axis stellarator has been tried for compatibility between high MHD beta limit and good confinement of trapped particles for a new flexible experimental device. The helical axis stellarator is realized with an $l = 1$ helical coil which has been designed to satisfy several physics requirements for fusion reactors; (1) good magnetic surface, (2) high value of MHD stable beta, (3) good confinement of high energy particles, (4) reduction of neoclassical transport, (5) small bootstrap current and (6) divertor configuration. Three helical axis stellarators are presented in this thesis. One is the Helias-like configuration and the other is the Heliac-like one. These have four magnetic field periods and both magnetic configurations are possible in a single device by adjusting the currents in helical, poloidal and toroidal coils. The Helias concept itself has been developed for the large stellarator device, Wendelstein 7-X (W7-X) and the Heliac for the high beta plasma confinement such as TJ-II and H-1. The third magnetic configuration is the new helical axis stellarator or an optimized $l = 1$ stellarator, which is based on the modulated $l = 1$ helical coil and has also four periods. These configurations are characterized by the magnetic field spectrum with three dominant Fourier components, toroidal ripple (ϵ_t), helical ripple (ϵ_h) and bumpy component (ϵ_b). The Heliac-like configuration has $\epsilon_t \sim 0.08$, $\epsilon_h \sim 0.06$ and $\epsilon_b \sim -0.04$ at the plasma surface at zero beta. The highest MHD stable beta $\langle \beta \rangle \sim 7.3\%$ is obtained among these three magnetic configurations; however, the reduction of neoclassical transport is weak. Here, $\langle \beta \rangle$ denotes the volume average beta value. The Helias-like configuration has $\epsilon_t \sim 0.05$, $\epsilon_h \sim -0.18$ and $\epsilon_b \sim -0.50$ at zero beta. The toroidal effect ϵ_t is significantly reduced compared to its geometrical inverse aspect ratio; however, the reduction of neoclassical transport is not large due to the enhancement of the magnetic field ripple by the large bumpy component with the same sign as that of helical one. The critical condition to reduce the neoclassical transport is to realize $\epsilon_b/\epsilon_h < 0$ and $|\epsilon_b| \sim |\epsilon_h|$. The optimized $l = 1$ stellarator has $\epsilon_t \sim 0.12$, $\epsilon_h \sim 0.15$ and $\epsilon_b \sim -0.15$ at zero beta. This configuration has a vacuum magnetic well in the whole plasma region due to the large pitch modulation of the $l = 1$ helical coil. The obtained magnetic configuration has almost comparable characteristics to the W7-X from the point of views of beta limit, neoclassical transport, bootstrap current and high energy particle confinement, although vacuum magnetic surfaces are

different from those in the W7-X.

Even if the above physics requirements are satisfied, it is probable that the plasma confinement is governed by anomalous transport in the realistic situations. The established way to suppress the anomalous transport is the L (low mode) to H (high mode) transition. One of the explanations of the physical mechanisms for the L - H transition in tokamaks is based on the bifurcation of the radial electric field through the existence of a local maximum in the plasma viscosity as a function of poloidal velocity. The same theory is extended to stellarator configurations and applied to the present and next generation stellarators including an optimized helical axis configuration described in this thesis and thereby the possibility of the L - H transition in stellarators is shown.

Acknowledgements

Contents

1 Introduction

Recently interest in stellarators has been increased both because of their potential advantages as eventual steady state fusion reactors and because of the contributions that they can make to the general understanding of toroidal plasma confinement. Significant progress has been made in stellarator theory, experimental results, device technology and reactor concept.

For realizing an economical fusion reactor based on magnetically confined plasmas, the ratio of plasma pressure to magnetic energy, $\langle \beta \rangle$, must exceed 5%, where $\langle \ \rangle$ denotes a volume average. The highest beta value is $\langle \beta \rangle \sim 2.1\%$ in stellarators, which has been obtained in the CHS [1]. However, this value is less than the highest one in tokamaks, $\langle \beta \rangle \sim 12.5\%$ obtained in the DIII-D [2]. Therefore, the next generation stellarators aim at demonstrating the attractiveness of the stellarator concept with more reactor relevant parameters. Realization of $\langle \beta \rangle \sim 5\%$ is one of the important issues.

In order to determine a size of a fusion reactor, confinement time or radial particle and energy transport is the most critical issue. Recent concern in the stellarator research is the confinement of currentless plasmas. The experimental confinement time of currentless plasma roughly follows the LHD (Large Helical Device) scaling [3] or the Lackner-Gottardi scaling [4]. If the LHD scaling is applied to a reactor size device of stellarator, it is understood that the confinement improvement of about a factor of two is necessary to realize a reactor with a reasonable size. The LHD scaling is similar to the gyro-reduced Bohm scaling [5] which is predicted by the anomalous transport based on drift wave turbulence. The anomalous transport governs the plasma confinement in toroidal geometry; however, it has not been explained rigorously and it seems beyond the scope of the classical or neoclassical transport theory. It should be noted that a more comprehensive energy confinement scaling (International Stellarator Scaling, ISS95) has been presented recently [6] based on the international stellarator database comprising data from the devices Heliotron E [7], CHS [8], ATF [9], Wendelstein 7-A (W7-A) [10] and W7-AS [11]. The parameter dependencies are similar to those of the Lackner-Gottardi scaling.

For present stellarator devices the neoclassical transport does not govern the plasma confinement as mentioned above; however, design of a new stellarator to reduce or to minimize the neoclassical transport is important. The

neoclassical transport is the collisional transport process which is modified by particle orbits specific in the non-uniform magnetic field geometry (cf., Section 2.2) from those in the uniform magnetic field geometry (classical transport). There are several reasons for the requirement of neoclassical transport reduction. The first is that the neoclassical transport easily becomes comparable to the anomalous transport without efforts of optimization. The second is that the reduction of the neoclassical transport is correlated with good trapped particle confinement, and the third is that the bootstrap current predicted by the neoclassical transport theory has been already observed in stellarators [12].

Like the axisymmetric tokamak and reversed field pinch, stellarators are confinement devices that rely on helical magnetic fields to keep the equilibrium and stability of toroidal plasma. Stellarators create these fields with currents flowing only in external conductors, allowing a wide range of magnetic configurations and external control of the magnetic properties. Hence, stellarators have different coil configurations according to different optimization principles. Recent stellarator devices are designed to test these optimization principles.

It is possible to design a stellarator with the beta limit on the order of 5% based on the ideal magnetohydrodynamic (MHD) theory and with almost no confinement of trapped particles. However, this type of stellarator may not be acceptable as a next generation device.

The satisfaction of compatibility between the high beta limit and the good confinement of trapped particles has led to designs and constructions of next generation large stellarators such as the LHD [13] (National Institute for Fusion Science, Japan) and the W7-X [14] (Max-Planck Institute, Germany). These devices have different coil configurations based on different optimization principles. In the LHD which is the optimized heliotron configuration, $l = 2$ helical coils have been designed for both an ideal MHD beta limit on the order of 5% and no trapped particle loss within one third radius at zero beta. Here l is a pole number of the helical field. On the other hand, the W7-X, which is based on a quasi-helically symmetric stellarator shown by Nührenberg and Zille [15], uses the carefully designed modular non-planar coils. The magnetic configuration of the W7-X is also optimized to realize a stable high beta equilibrium with sufficiently good confinement of energetic particles. The concept of the Modular Helias-like Heliac (MHH) has

also been developed for a stellarator reactor in the United States Stellarator Power Plant Study (SPPS) [16]. It is noted that the W7-X and the MHH belong to the helical axis stellarator with the $l = 1$ helical field dominantly.

The modular coil system in the W7-X has been designed by solving the boundary value problem for the specified shape of the plasma boundary. It is appropriate for the stellarator reactor when its mentenance is considered and after the most desirable magnetic configuration is obtained from the wide range of investigations for plasma confinement. However, there is a disadvantage to lose flexibility of magnetic configuration for a given coil system, which is required for an experimental device to study stellarator physics and to pursue the most desirable magnetic configurations for plasma confinement. Thus for investigating wide parameter range of helical axis stellarator in a single device, it has been tried to develop a new stellarator configuration using a pitch modulated $l = 1$ helical coil, poloidal and toroidal coils. In this thesis, several new helical axis stellarator configurations, Helias-Heliac Hybrid Stellarator (HHHS) [17] and an optimized $l = 1$ stellarator [18], are presented, which have been obtained by theoretical guidances for compatibility between the high beta limit and the good trapped particle confinement. The physics requirements for the optimization are the stable high beta plasma on the order of 5%, the good trapped particle confinement and the reduction of neoclassical diffusion and bootstrap current. Both Helias-like and Heliac-like configurations are possible in a HHHS by adjusting the currents in helical, poloidal and toroidal coils. Among these two representative configurations in a HHHS, Heliac-like configuration has $\langle \beta \rangle_{st} \sim \langle \beta \rangle_{eq} \sim 7.3\%$, but the neoclassical transport is not optimized due to the broad spectrum of the magnetic field, although the particle diffusivity is about one order magnitude smaller than that of Helias-like configuration by controlling the bumpy component which is large and has the same sign as the helical one, resulting in the enhancement of the magnetic field ripple in the region of $\theta \sim 0$, i.e., in the weak magnetic field region. Here, θ is a poloidal angle. The more optimized helical axis configuration is obtained by changing the sign of the pitch modulation of $l = 1$ helical coil and realizing the bumpy field component with the opposite sign to the $l = 1$ helical field to weaken the field ripple in the region of $\theta \sim 0$. In this case, the reduction of neoclassical transport is successful and its plateau level of particle diffusivity is almost comparable to that of equivalent tokamak. Capability of this magnetic configuration is similar

to the W7-X from the point of views of beta limit, neoclassical transport, bootstrap current and high energy particle confinement, although vacuum magnetic surfaces are somewhat different from the W7-X.

In addition to the above favorable properties for plasma confinement in an optimized helical axis configuration, the large clearance between the helical coil and the outermost magnetic surface, and the one between the chamber surface and the outermost magnetic surface are advantageous for plasma heating and diagnostics and the reduction of plasma - wall interaction in designing a new experimental device.

One weak point of the above mentioned optimization is that the understanding of the anomalous transport governing the plasma confinement in the realistic situations is not sufficient. Even if the anomalous transport is dominant in the helical axis stellarator, the confinement improvement based on the L (low mode) - H (high mode) transition will be expected under certain conditions. The H mode is the discharge with improved energy confinement found in tokamaks [19, 20] and recently similar discharges have been observed in stellarators, for example, W7-AS [21] and CHS [22]. Since there is a significant difference in the magnetic configuration between tokamaks and stellarators, H mode experiments in present stellarators are important in clarifying the physics of the L - H transition and in developing the L - H transition theory, if the mechanism is the same for both types of device. One of the explanations of the physical mechanisms for the L - H transition in tokamaks is based on the bifurcation of the radial electric field E_r through the exsistence of a local maximum in the plasma viscosity as a function of poloidal flow velocity [23, 24, 25, 26]. The qualitative results based on this theory are in good agreements with the experimental observations of the L - H transition in DIII-D [23] or JFT-2M [24]. It is noted that the radial electric field is also effective to improve the trapped particle confinement and reduce the neoclassical transport.

This thesis is organized as follows. First the approach for the optimization of the helical axis stellarator will be shown in Chapter 2. In order to clarify physics requirements for optimizing the helical axis stellarator, MHD equilibrium and stability, collisionless particle orbits and neoclassical ripple transport will be briefly described in Chapter 2. Analyses of collisionless particle are required to clarify the behavior of high energy particles with sufficiently small collision frequency which are sensitive to the magnetic and

electric field itself and give a good indication for the confinement of high temperature plasma. Eventually, it is necessary to investigate the confinement properties of 3.52 MeV α particles produced by D - T fusion reaction and to assess an efficiency of α heating when the stellarator reactor is considered. Moreover, for realizing a steady state operation of a fusion reactor, continuous exhaust of heat and ash by a divertor is inevitable. From this point of view, behavior of magnetic field line in the outside region of the last closed magnetic surface will be also discussed briefly. In Chapter 3, details of characteristics of the obtained helical axis stellarators are described from the points of view of MHD beta limit, trapped particle confinement, neoclassical transport coefficient and bootstrap current. Physics requirements are almost satisfied in an optimized $l = 1$ stellarator or the particular one of HHHS. In Chapter 4, the L - H transition theory mentioned above is extended to stellarator configurations including the helical axis stellarator to clarify the characteristics of present and next generation stellarator devices from the L - H transition point of view [27]. Concluding remarks of this thesis will be given in Chapter 5.

2 Strategy of Configuration Optimization for Stellarator

2.1 Principles of the Optimization

The configuration optimization is necessary for realizing an efficient and compact stellarator fusion reactor. An example of the optimized stellarators is the quasi-helically symmetric stellarator [15], which shows that the magnetic spectrum of a stellarator can be controlled with modular coils.

The magnetic field in the confinement region can be optimized by noting that geometry of the last closed magnetic surface completely determines properties of MHD equilibrium. Thus the fixed boundary MHD equilibrium is solved during the optimization procedure, where the parameters of the boundary are the optimization valuables. It is shown that the boundary value problem is the basic ingredient of the optimization procedure employed in the design of the W7-X [14]. For the configuration optimization, the following set of criteria is useful:

1. High quality of the vacuum magnetic surfaces: low order rational surfaces should be carefully avoided.

2. Good finite beta equilibrium properties: a small Shafranov shift and a small variation of the rotational transform for finite beta currentless plasmas will yield a high equilibrium beta limit. This is equivalent to the reduction of Pfirsch-Schlüter current (PSC).

3. Good MHD stability properties: MHD stability in low shear stellarators is mainly provided by a magnetic well. A vacuum magnetic well can be created by suitably chosen indentation and triangularity of the magnetic surfaces. Figure 2.1 shows the magnetic surface cross section in the W7-X at $\langle \beta \rangle = 5\%$. It changes from bean shaped to tear-drop to triangular in one-half period.

4. Reduced neoclassical transport in the long mean free path ($lmfp$) $(1/\nu)$ regime, where ν is a collision frequency: the existence of the quasi-helically symmetric stellarators implies that the toroidal stellarators without the $1/\nu$ transport regime exist. The conventional nonaxisymmetric stellarators can be characterized by a normalized ripple transport coefficient $D_R = 1.65\delta_e^{\frac{3}{2}}L^*$ ($L^* \propto 1/\nu$ is the normalized mean free

path) with the magnitude of the equivalent ripple δ_e determined by Monte Carlo simulation of electron transport in the $lmfp$ regime [28]. This δ_e must be kept small to guarantee sufficiently good neoclassical confinement.

5. Small bootstrap current in the $lmfp$ regime: the bootstrap current changes the rotational transform and, therefore, it is particularly dangerous in low shear stellarators, in which the rotational transform has to be carefully adjusted to avoid low order rational surface. It is possible to reduce the bootstrap current by a proper combination of the helical, toroidal and bumpy components [29]. Fourier spectrum of the magnetic field in the W7-X is shown in Fig. 2.2. It is considered that the spectrum is significantly pure. The suitable combination of the three components (helical, toroidal and bumpy) is essential for reducing the bootstrap current as described later. It is noted that the reduction of the bootstrap current has also been considered in the MHH configurations [30].

6. Good collisionless α particle or high energetic particle confinement: for α particle confinement in a stellarator reactor, a situation similar to bumpy ripple induced orbit losses in tokamaks may arise. Lotz et al. evaluated the collisionless α particle losses in the W7-X configuration as functions of the time of flight [31]. An example of the obtained results is shown in Fig. 2.3. Each symbol indicates the loss of one α particle for $\langle \beta \rangle = 0\%(\bullet)$, $2.4\%(\times)$ and $4.9\%(\triangle)$. Deviation from the quasi-helical symmetry for reducing the bootstrap current causes the α particle losses similar to conventional stellarators at vacuum field. However, the diamagnetic effect in W7-X finite beta plasmas without the significant magnetic axis shift tends to improve the drift orbit confinement, which results in the reduction of α particle loss fraction in the operating regime of beta value.

7. Good modular coil feasibility: generally, strong geometrical shaping of the plasma boundary will improve confinement and stability properties while it requires a complicated coil system. Important issues for selecting the coil geometry are the minimum distance between the coils and the plasma and the minimum radius of the curvature of the coils.

In designing an optimized stellarator, compromization between some criteria is usually necessary. For example, in designing the W7-X magnetic configuration, the necessity of the small bootstrap current requires some deviation from quasi-helical symmetry, resulting in an enhanced collisionless particle orbit loss and the neoclassical ripple transport.

It is noted that the bootstrap current increases as plasma pressure or beta value increases. However, its effects are not so significant in low beta plasmas. The HSX device [32, 33] aims to demonstrate experimentally the confinement performance of the quasi-helically symmetric stellarator configuration in low beta plasmas. Figure 2.4 shows the cross sections of magnetic surfaces of the HSX at $\langle \beta \rangle = 0.7\%$. It is noted that they are not so different from those of the W7-X in the real space as shown in Fig. 2.1, however, the magnetic spectrum in the Boozer coordinates is significantly different compared to the W7-X case as shown in Fig. 2.5. It is clearly seen that the main spectrum is the helical component and the others are negligible, which means the quasi-helical symmetry. If large bootstrap current flows with the opposite direction to that in tokamaks as is predicted by neoclassical transport theory [34], it will be observed experimentally in the HSX.

The experimental realization of such magnetic configurations involves the problem of finding a distribution of the external coil currents which produces a magnetic field maintaining the plasma equilibrium and satisfying the boundary conditions at the plasma boundary $\boldsymbol{B}_v \cdot \boldsymbol{n} = 0$ and $\boldsymbol{B}_v^2 = \boldsymbol{B}_p^2 + 2p$, where $\boldsymbol{n}$ is the exterior normal vector to the boundary and p is the plasma pressure. Calculation of the magnetic field in the vacuum region (outside the plasma) leads to a boundary value problem, which is not well posed for an elliptic partial differential equation for the magnetic potential. Moreover, it often happens that the singularities, which correspond to the currents, appear too close to the plasma surface.

These difficulties may be resolved if one does have an interest in an approximate solution of the boundary value problem as shown by Merkel [35]. The external vacuum field can be represented by superposing harmonic functions such as Dommaschk potentials [36] for such a solution. This solution yields a vacuum field which is regular in the whole domain bounded by the chosen outer surface. This vacuum field uniquely determined by the shape of the plasma boundary can be used to find the position of the coils. The current lines on the outer surface may be shaped in such a way that closed

current lines are discretized into a finite number of coils. Figure 2.6 shows an example of the surface current lines without net current distribution in the toroidal direction. The poloidally closed current lines can be easily discretized and represented by a finite number, 15 in this case, of modular coils. Such a modular coil configuration with 15 finite size modular coils per field period designed for the W7-X is shown in Fig. 2.7.

In this thesis, the object is to realize a helical axis stellarator configuration satisfying the above criteria based on an $l = 1$ helical coil with additional poloidal and toroidal coils. This coil system is different from modular coil system and has an advantage to change the coil current ratio among three types of coil. Characteristics of the obtained helical axis configurations will be described in Chapter 3 from the points of view of MHD beta limit, properties of trapped particle confinement and neoclassical transport.

The rest of this chapter is devoted to describe the plasma physics for optimizing the helical axis stellarator and numerical methods for quantitative analyses of several physics properties such as MHD equilibrium and stability, collisionless particle orbit confinement and neoclassical transport.

2.2 Collisionless Particle Orbit Confinement and Neoclassical Transport

In tokamaks, the breaking of the axisymmetric property due to the bumpy field by discretized toroidal coils has a significant influence on the α particle confinement, resulting not only in the degraded efficiency of fuel plasma heating by α particles but also in the localization of heat load on the first wall. On the other hand, in stellarators, it seems to be inevitable to have significant α particle losses because of its proper three dimensionality. Recently, it is shown that there are some configurations to confine α particles sufficiently. The HSX device [32, 33], which is now under construction at the University of Wisconsin-Madison [37], has a quasi-helical symmetry and sufficiently good α particle confinement property is predicted at least for low beta plasmas. In the W7-X, α particle losses decrease as beta is increased [31] as discussed in Section 2.1. Since high energy particles such as 3.52 MeV α particles produced by D-T fusion reactions have extremely low collisionality, they can be treated as collisionless particles. They essentially move due to the magnetic field, therefore, their orbit properties greatly depend on the field structure itself. The investigation of such high energy particle orbits is one of the basic subjects for the optimization of the stellarator magnetic field configuration.

When the Coulomb collisions are taken into account in quiet stationary plasmas, the particle behaviors become to be governed by diffusion processes, which is simply expressed by

$$D \sim \nu \Delta^2, \tag{2.1}$$

where D is the collisional diffusion coefficient, ν is the collision frequency and Δ is the characteristic step width especially estimated in radial direction. For the configuration optimization, the neoclassical diffusion property is compared in several magnetic configurations, especially in the low collisional regime, where the trapped particle orbits are clearly seen. In this thesis the neoclassical diffusion process is considered appropriate only in the plasmas, in which MHD equilibrium and stability are guaranteed.

Drifts of plasma particles across magnetic surfaces are induced by variations of the magnetic field strength along the magnetic field lines. Ideal confinement of particle orbits could be achieved in a configuration where the magnetic field strength is a function of magnetic surface, which is so called an

'omnigenous' or 'isodynamic' configuration [38]. However, Bernardin et al. [39] showed that toroidal isodynamical equilibria can possibly exist only in limits in which the magnetic field strength on the magnetic axis vanishes or the magnetic surfaces become open. Since neither of these limits are practical for plasma confinement, toroidal isodynamic equilibria may not be realized.

Figures 2.8 show the variation of the magnetic field strength along the magnetic field line for (a) axisymmetric tokamak, (b) conventional stellarator and (c) quasi-helically symmetric stellarator and they can be expressed by

$$B = B_0[1 - \epsilon_t \cos \theta], \tag{2.2}$$
$$B = B_0[1 - \epsilon_t \cos \theta - \epsilon_h \cos(l\theta - M\zeta)], \tag{2.3}$$
$$B = B_0[1 - \epsilon_h \cos(l\theta - M\zeta)], \tag{2.4}$$

respectively, where ϵ_t denotes the modulation of the magnetic field strength by the toroidicity and ϵ_h by the helical component with l and M, where l is a pole number and M is a number of the field period. In the axisymmetric tokamak the banana particle reflects at the same poloidal position because there is no variation of the magnetic field strength in the toroidal direction as shown by Eq. (2.2). Therefore, the step width Δ in Eq. (2.1) is banana orbit width $\Delta_b \sim \frac{\rho_L}{\iota\sqrt{\epsilon_t}}$, where ρ_L is the Larmor radius, resulting in the diffusion coefficient derived by Galeev and Sagdeev [40]. Contrary to this simple variation of the magnetic field strength in axisymmetric tokamak, conventional stellarator has two kinds of modulation from the toroidicity and the helical component as expressed by Eq. (2.3). In this case, the magnetic field strength depends on both poloidal and toroidal angles. Therefore, the reflection point changes in poloidal direction as the trapped banana particle moves in toroidal direction with repeating the bounce motion. In this case, the step width is determined by the toroidal drift motion of the helically trapped particle, $\Delta_h \sim \frac{V_\perp}{\nu_{eff}}$, where ν_{eff} is the effective collision frequency $\nu_{eff} = \nu_{ei}/\epsilon_h$ and $V_\perp$ is the toroidal drift velocity. The diffusion coefficient in this regime is inverse proportional to ν_{eff}, which is so called $1/\nu$ ripple diffusion. This dependence of the diffusivity on the collision frequency means that the neoclassical diffusivity has a tendency to become larger as the collision frequency decreases, for example, due to the increase of the plasma temperature. This is a serious problem for the stellarator concept. Therefore, the reduction or disappearance of $1/\nu$ ripple transport is an important issue in optimizing the stellarator configurations. One example for resolving

this problem is the quasi-helically symmetric stellarator [15] such as the HSX [32] in which the magnetic field strength can be approximated by Eq. (2.4). In the quasi-helically symmetric configuration, the toroidal ripple is greatly reduced. These simple models of the variation of the magnetic field strength along the magnetic field line are useful for understanding physics to reduce the $1/\nu$ ripple transport sufficiently and to realize a tokamak like neoclassical transport property in the low collisional regime.

Studies of collisionless particle orbits in stellarator configurations have often been pursued with the guiding center equations. This approach relies on the adiabatic invariants to average over bounce motion for particles trapped in the local magnetic ripple well. In the derivation it is assumed that the rotational transform per field period ι/M is small and that there is only one magnetic ripple well per period. Although there are multiple ripple wells in the realistic situations, it is not feasible to extend the bounce averaging procedure to include multiple ripple wells. It is also necessary to treat accurately the transitions between various trapping states. Collisionless trapping/detrapping occurs here [41, 42].

Description of the particle drifts is the most appropriate with the guiding center drift equations in the Boozer coordinates (ψ, θ_B, ϕ_B) [43]. The magnetic field can be described as $\boldsymbol{B} = \nabla\chi$ in the covariant form for the vacuum field case; however, $\boldsymbol{B} = \nabla\chi + \tilde{\beta}\nabla\psi$ for the finite beta case, where χ is a scalar potential of the magnetic field and $2\pi\psi$ is the toroidal flux. The guiding center drift equations for the finite beta case are [44]

$$
\begin{aligned}
\dot{\psi} &= \frac{\delta}{\gamma}\left(\frac{\partial B}{\partial \phi_B}I - \frac{\partial B}{\partial \theta_B}g\right), \\
\dot{\theta_B} &= \frac{g}{\gamma}\left(\delta\frac{\partial B}{\partial \phi_B} + e\frac{\partial \Phi}{\partial \psi}\right) - \frac{e^2 B^2}{m}\rho_c\left(\frac{\rho_c g' - \iota}{\gamma}\right), \\
\dot{\phi_B} &= -\frac{I}{\gamma}\left(\delta\frac{\partial B}{\partial \phi_B} + e\frac{\partial \Phi}{\partial \psi}\right) + \frac{e^2 B^2}{m}\rho_c\left(\frac{\rho_c I' + 1}{\gamma}\right), \\
\dot{\rho_c} &= \frac{\delta}{\gamma}\left[\frac{\partial B}{\partial \theta_B}\left(\rho_c g' - \iota\right) - \frac{\partial B}{\partial \phi_B}\left(\rho_c I' + 1\right)\right],
\end{aligned}
\tag{2.5}
$$

where $2\pi I(\psi)$ is the toroidal current within a magnetic surface, $2\pi g(\psi)$ is the poloidal current outside a magnetic surface, $\Phi(\psi)$ is the radial electrostatic potential, $\rho_c = mv_\parallel/eB$, and θ_B (ϕ_B) is the poloidal (toroidal) angle in the Boozer coordinates, respectively. The prime denotes the derivative with

respect to ψ. The functions δ and γ are defined by

$$
\begin{aligned}
\delta &= e^2\rho_c^2 B/m + \mu, \\
\gamma &= e[g(\rho_c I' + 1) - I(\rho_c g' - \iota)],
\end{aligned}
$$

where μ is the magnetic moment. Since currentless equilibria are assumed throughout in this thesis, $I = 0$ is standard in these equations. Moreover, $g' = 0$ for the vacuum filed case, where the field is curl-free. In these equations, the strength of the magnetic field is the only necessary data from the MHD equilibrium besides surface quantities.

The neoclassical transport theory for stellarators has been intensively studied for a simple magnetic field model:

$$
B = B_0[1 - \epsilon_t\cos\theta - \epsilon_h\cos(l\theta - m\phi)],
$$

where B_0 is the magnetic field strength on the magnetic axis, ϵ_t and ϵ_h are the toroidal and helical ripples, respectively, and l (m) is the poloidal (toroidal) mode number. However, the magnetic field of stellarators usually have more than one helical component, especially in finite beta cases. In the low collisionality regime, where the effective collision frequency ν_{eff} of the helically trapped particles is less than their bounce frequency ω_b, the collisionless particle orbits, and thus the neoclassical ripple transport are affected significantly by the multiple helicity effect. Shaing and Hokin showed that for a class of stellarator equilibria with only one toroidal mode number, the magnetic field model can be reduced to a simple form [45]. Consequently, the particle orbits and transport processes in such a system can be treated analytically provided $m/\iota \gg l$.

The magnetic configurations described in this thesis satisfy this condition because $m = 4$, $0.7 \lesssim \iota \lesssim 1.8$ and $l = 1$. In order to find the approach to reduce the neoclassical ripple transport, the analytical expression is applied to obtain the appropriate magnetic field structure. This is a generalization of previous work so called σ-optimization by Mynick [46] to include a broader range of realistic magnetic configurations.

In Ref. [45] the magnetic field strength B is approximately expressed by

$$
B/B_0 = 1 - \epsilon_t\cos\theta - \epsilon_d\cos l\theta - \sum_{n=-\infty}^{\infty} \epsilon^{(n)}\cos(n\theta + \eta),
\tag{2.6}
$$

where $\epsilon^{(n)}$ are the amplitudes of the corresponding harmonics and $\eta = l\theta - m\phi$. It is noted that $\epsilon^{(0)}$ describes the usual helical modulation ϵ_h. In order

to calculate the second adiabatic invariant J which may describe the trapped particle orbit, Eq. (2.6) assumes a single toroidal mode number m. Without loss of generality, $n = 0, n = \pm 1$ and ± 2 terms are only kept in Eq. (2.6). Using the mathematical formula

$$\cos(\pm n\theta + \eta) = \cos n\theta \cos \eta \pm \sin n\theta \sin \eta \,,$$

Eq. (2.6) can be simplified to

$$
\begin{aligned}
B/B_0 &= 1 - \epsilon_t \cos\theta - \epsilon_d \cos l\theta \\
&- \sqrt{C^2 + D^2}\left(\frac{C}{\sqrt{C^2 + D^2}}\cos\eta - \frac{D}{\sqrt{C^2 + D^2}}\sin\eta\right),
\end{aligned}
\tag{2.7}
$$

where $C = \epsilon^{(0)} + [\epsilon^{(+1)} + \epsilon^{(-1)}]\cos\theta + [\epsilon^{(+2)} + \epsilon^{(-2)}]\cos 2\theta$ and $D = [\epsilon^{(+1)} - \epsilon^{(-1)}]\sin\theta + [\epsilon^{(+2)} - \epsilon^{(-2)}]\sin 2\theta$. If a phase angle χ is defined as

$$\cos\chi = \frac{C}{\sqrt{C^2 + D^2}}, \quad \sin\chi = \frac{D}{\sqrt{C^2 + D^2}},$$

a simple model for a stellarator with multiple helical components is given as

$$B/B_0 = 1 - \epsilon_T - \epsilon_H \cos(\eta + \chi), \tag{2.8}$$

where $\epsilon_T = \epsilon_t \cos\theta + \epsilon_d \cos l\theta$ and $\epsilon_H = \sqrt{C^2 + D^2}$. It is noted that the magnetic field model given by Eq. (2.8) can be reduced to a model proposed by Mynick by setting $\epsilon^{(+1)} = \epsilon^{(-1)}$ and $\epsilon^{(+2)} = \epsilon^{(-2)} = 0$. Then

$$B/B_0 = 1 - \epsilon_t \cos\theta - (1 - \sigma \cos\theta)\cos\eta \,,$$

where σ is a parameter related to the position of the magnetic ripple localization.

With the model magnetic field given by Eq. (2.8), the second adiabatic invariant J for the helically trapped particles can be obtained as

$$J = (16R_0/m)(\mu B_0 \epsilon_H/m_p)^{1/2}[E(k) - (1 - k^2)K(k)], \tag{2.9}$$

where R_0 is the major radius, μ is the magnetic moment, m_p is the mass of the relevant particle and K and E are complete elliptic integrals of the first and second kind with the pitch angle parameter

$$k^2 = [W - \mu B_0(1 + \epsilon_T - \epsilon_H)]/2\mu B_0 \epsilon_H \,,$$

where W is a particle energy. For the helically trapped particles, $0 \leq k^2 \leq 1$ is satisfied. To obtain Eq. (2.9), $m/\iota \gg l$ is assumed and this assumption

implies that the field line is mainly directed in the toroidal direction within one helical period due to a small rotational transform per field period.

Then the bounce averaged drift velocity for the helically trapped particle are

$$
\begin{aligned}
r\dot\theta &= \frac{\mu B_0}{m_p\Omega}\left[\frac{\partial \epsilon_H}{\partial r}\left(\frac{2E}{K} - 1\right) - \frac{\partial \epsilon_T}{\partial r}\right], \\
r\dot r &= -\frac{\mu B_0}{m_p\Omega}\left[\frac{\partial \epsilon_H}{\partial\theta}\left(\frac{2E}{K} - 1\right) - \frac{\partial \epsilon_T}{\partial\theta}\right],
\end{aligned}
\tag{2.10}
$$

where Ω is the gyrofrequency. The bounce averaged drift kinetic equation associated with the above drift equations leads to the expression of the particle flux in $1/\nu$ regime,

$$
\begin{aligned}
\Gamma &= -\frac{4}{\pi}\frac{1}{m_p^{7/2}\Omega^2 r^2}\int_0^\infty dW \frac{W^{5/2}}{\nu}\frac{\partial f_M}{\partial r} \\
&\times\left\{\int_0^{2\pi} d\theta\, \epsilon_H^{3/2}\left[G_1\left(\frac{\partial \epsilon_T}{\partial\theta}\right)^2 - 2G_2\frac{\partial \epsilon_T}{\partial\theta}\frac{\partial \epsilon_H}{\partial\theta} + G_3\left(\frac{\partial \epsilon_H}{\partial\theta}\right)^2\right]\right\},
\end{aligned}
\tag{2.11}
$$

where f_M is a Maxwellian and $G_i(i = 1, 2, 3)$ are the numerical coefficients given by

$$G_1 = 16/9 \,, \quad G_2 = 16/15 \,, \quad G_3 = 0.684 \,.$$

In the case of magnetic configuration considered in this thesis, the main modulations of the magnetic field arise from the toroidal field (ϵ_t), the helical field ($\epsilon^{(0)} = \epsilon_h$) and the bumpy field ($\epsilon^{(-1)} = \epsilon_b$) and can be expressed as

$$B/B_0 = 1 - \epsilon_t \cos\theta - \epsilon_h \cos(\theta - 4\phi) - \epsilon_b \cos 4\phi \,,$$

where the toroidal mode number is assumed four for helical axis configurations considered in Chapter 3. Applying the above theory to this model magnetic field, ϵ_T and ϵ_H become

$$
\begin{aligned}
\epsilon_T &= \epsilon_t \cos\theta \,, \\
\epsilon_H &= \sqrt{\epsilon_h^2 + 2\epsilon_h\epsilon_b\cos\theta + \epsilon_b^2} \,,
\end{aligned}
\tag{2.12}
$$

respectively. The product of ϵ_h and ϵ_b appears in the expression of ϵ_H, which implies that the particle flux is affected by the sign of $\epsilon_h\epsilon_b$ as discussed in Chapter 3.

Hirshman et al. developed the DKES (Drift Kinetic Equation Solver) code to solve the drift equation for stellarator configurations [47]. In this code, the drift kinetic equation is numerically solved in the phase space, where the perturbed distribution function is expanded with Legendre polynomials for the pitch angle in the velocity space and with Fourier modes in

the poloidal and toroidal coordinates on a given magnetic surface. With respect to the Coulomb collision operator, only the pitch angle scattering term is retained or the energy diffusion term is neglected for simplification. The application of the DKES code is, therefore, valid in the *lmfp* regime, namely the banana regime where the trapping/detrapping process governs the neoclassical transport. In the DKES code, three components of the transport matrix [48], corresponding to diffusivity, viscosity and bootstrap current, are calculated as functions of the two independent parameters — the mean free path at a fixed particle energy, $(\nu/v)^{-1}$, and the radial electric field devided by the particle velocity, E_r/v, where ν is the collision frequency, v is the monoenergetic particle velocity and E_r is the radial electric field. The upper and lower bounded values of the three components of the transport matrix are obtained by a variational principle and the other components of the transport matrix may be derived from these three values. The outline of this code and some applications are mentioned in Appendix A.

The W7-AS team has made comprehensive comparisons between experimentally observed thermal diffusivities and those calculated by the DKES code [49]. In ATF experiments, controllability of the bootstrap current with the quadrupole magnetic field has been clearly demonstrated, and experimental results are in good agreement with DKES calculations [50].

It is noted that numerical simulations with a Monte Carlo technique are also useful for the neoclassical transport in stellarators as shown by various authors [28, 51, 52].

2.3   MHD Equilibrium and Stability

Stellarator plasmas are required to treat as three dimensional (3D) configurations because there is no geometrical symmetry. However, for heliotron devices, MHD equilibria were analyzed based on the simplification of its 3D configuration to two dimensional one by an averaging. Stellarator expansion [54, 55] and averaging method are such examples and these two methods are essentially equivalent, which lead to a Grad-Shafranov type MHD equilibrium equation [56]. These approaches come from that stellarators are envisioned to operate with a large aspect ratio and are based on the assumption that the nonaxisymmetric part of the magnetic field is small and periodic length in the toroidal direction is much shorter than the major radius of the system. The stellarator expansion, after the averaging over the magnetic ripples in the lowest order, gives an axisymmetric Grad-Shafranov type equilibrium equation. Here, the expansion parameter is $\delta \sim B_h/B_0 \sim \epsilon^{\frac{1}{2}} \sim \beta^{\frac{1}{2}}$, where $B_h = |\boldsymbol{B}_h|$ is the external helical field and ϵ is an inverse aspect ratio. Since they have only minor mathematical differences from the Grad-Shafranov equation for an axisymmetric tokamak, it is useful to modify the PEST equilibrium code [57], which is used to study tokamak equilibria, to solve the stellarator equilibria. The modified code is called STEP code [55].

On the other hand, according to the development of supercomputers, analyses of 3D configurations have become possible, and the pioneer work was done by Garabedian et al. [58]. They developed the 3D MHD equilibrium code BETA based on the finite element method to obtain the minimum state of variational principle. The BETA code requires the large memory size and has a strong dependence of the numerical solution on mesh sizes. Therefore, it is required to extrapolate the numerical solutions with finite mesh sizes to a zero mesh size solution. For supplementing this disadvantage, Hirshman et al. have introduced the moment (spectral) method, which had been used in the inverse spectral equilibrium solver for tokamaks, to the approach of BETA code. This code is called VMEC (Variational Moment Equilibrium Code) [59]. When the spectral method based on Fourier expansion in the angle variables is introduced, the convergence problem is much improved in the VMEC. It is noted that the poloidal angle variable is chosen such as to minimize the number of Fourier modes. The VMEC is now commonly used to calculate MHD equilibria for the stellarators and the description of the magnetic configuration for VMEC computations becomes standard for the

stellarator database activity [6]. The VMEC has been used to investigate MHD equilibrium properties of the helical axis stellarator configuration in this thesis. The outline of this code is given in Appendix B.

It should be noted that the existence of nested magnetic surfaces has not been proved for toroidal stellarator MHD equilibrium, and its proof seems to be negative according to the KAM theorem [60]. However, since the existence of the equilibrium in the straight stellarator configuration is guaranteed by the helical symmetry, the existence of nested magnetic surfaces is often assumed if the toroidal effect is sufficiently small. In other words, it is accepted in practice that the equilibrium exists when magnetic islands and stochastic behavior of magnetic field line are negligible in the calculation of the vacuum magnetic field by field line tracing calculation. In particular, the most commonly used 3D MHD equilibrium codes such as BETA and VMEC employ algorithms which assume the existence of the nested magnetic surfaces.

The more complicated problem is the behavior of magnetic islands in finite beta plasmas. Recently, 3D equilibrium codes, which do not a priori require the existence of nested magnetic surfaces, HINT [61] and PIES [62] codes have been developed. These codes are based on quite different numerical algorithms. For example, the parallel motion of plasma is solved separately from the perpendicular motion, which ensures that pressure is constant along magnetic field lines in the Eulerian grid in the HINT code and an iteration scheme of MHD equilibrium equations is employed in the magnetic coordinates in the PIES code [63]. With the HINT code, fragility of the magnetic surfaces at finite beta plasmas and possible methods to keep good surfaces in large shear $l = 2$ equilibria were investigated in detail [61]. The HINT code has also been applied to study the finite beta effect on an isolated magnetic island chain in a low shear Helias equilibria. Sizes and phases of the particular island chain at $\iota = 5/6$ were studied for their dependencies on external vacuum field parameters, which led to the discovery of the self-healing phenomenon. When the X point of vacuum magnetic island is overlapped by the O point of pressure-driven magnetic island, the island width becomes quite thin over an appreciable range of beta values [61]. Application of the PIES code to Helias equilibria has also begun [64] and resulted in a demonstration of the existence of nested magnetic surfaces by suppressing the island chain at $\iota = 5/6$.

With regard to MHD stability in currentless stellarator plasmas, the ideal

pressure driven instabilities are crutial for evaluating the critical beta value. The currentless equilibrium means that the toroidal current averaged over each magnetic surface is zero, although the local current density is non-zero. The interchange mode has the property that the Mercier criterion gives a good indication of the stability beta limit [65, 66].

For obtained MHD equilibria, 3D Mercier stability criterion [67] is evaluated for local interchange modes,

$$D_M = D_S + D_W + D_I + D_G \geq 0 \,,$$

where

$$
\begin{aligned}
D_S &= \frac{(\psi_P'' \psi_T')^2}{4} \frac{s}{\iota^2 \pi^2} \,, \\
D_W &= \frac{s}{\iota^2 \pi^2} \int \int g d\theta d\zeta \frac{B^2}{g^{ss}} p' \left(V'' - p' \int \int \frac{g d\theta d\zeta}{B^2} \right) , \\
D_I &= \frac{s}{\iota^2 \pi^2} \left[\int \int g d\theta d\zeta \frac{B^2}{g^{ss}} \psi_P'' I' - (\psi_P'' \psi_T') \int \int \frac{g(\boldsymbol{J} \cdot \boldsymbol{B}) d\theta d\zeta}{g^{ss}} \right] , \quad (2.13) \\
D_G &= \frac{s}{\iota^2 \pi^2} \left[\int \int g d\theta d\zeta \frac{(\boldsymbol{J} \cdot \boldsymbol{B})}{g^{ss}} \right]^2 \\
&\quad - \frac{s}{\iota^2 \pi^2} \left[\int \int g d\theta d\zeta \frac{(\boldsymbol{J} \cdot \boldsymbol{B})^2}{g^{ss} B^2} \right] \left(\int \int g d\theta d\zeta \frac{B^2}{g^{ss}} \right) .
\end{aligned}
$$

Here, ψ_T and ψ_P are the toroidal and poloidal magnetic flux functions, g is the Jacobian, p is the scalar plasma pressure, I is the toroidal current within a magnetic surface, and $g^{ss} = |\nabla s|^2$ is the corresponding metric element. The radius like variable s is given by the toroidal flux normalized at the plasma edge, and the primes indicate derivatives with respect to s. This form for the Mercier criterion is the same as the one given in Ref. [58]. In this stability criterion, D_S gives the stabilizing contribution of the magnetic shear, D_W is the contribution of the magnetic well or hill, D_I gives the contribution of net plasma current, and D_G the contribution of the local geodesic curvature. In configurations with a magentic well, the term D_W is positive and stabilizing. The term D_G is always negative and, therefore, destabilizing. As the pressure is increased, the D_W term becomes more positive; however, the D_G term becomes more negative. Thus, the Mercier stability criterion $D_M \geq 0$ is usually a fine balance of these two terms. In Ref. [68], dependence of the D_M value on the D_W term is investigated for TJ-II Heliac [69] in detail by using the VMEC by changing the vacuum magnetic well depth for fixed values of rotational transform.

For currentless plasmas, $D_I = 0$ is always valid. The three helical axis stellarator configurations discussed in this thesis have low shear in the vacuum. Thus, for very low beta plasmas, the magnetic well formation is necessary to satisfy the Mercier stability. This concept to stabilize interchange modes with magnetic well is the same as in Helias and Heliac configurations, in which the magnetic shear is generally very low for a wide range of beta values.

The investigation of MHD stability has been restricted only to ideal Mercier stability as the first insight. For the Mercier stable case, more detailed investigations of, for example, resistive interchange modes and ballooning modes, are required to determine the stability beta limit more precisely [70].

It should be noted that the parallel current calculated directly from the components of the magnetic field in the VMEC ('direct method') is used in the above Mercier criterion. However, there have been arguments that the Mercier criterion should be evaluated with the parallel current obtained by solving a magnetic differential equation derived from the local equilibrium equation ('indirect method' [71, 72]), Eq. (19) in Ref. [72],

$$\left(\frac{\boldsymbol{j} \cdot \boldsymbol{B}}{B^2}\right)_{m,n} = \left(\frac{P'}{\psi'_P J - \psi'_T I}\right)\left(\frac{mI - nJ}{m\psi'_P - n\psi'_T}\right)(\sqrt{g})_{m,n} . \qquad (2.14)$$

When nested magnetic surfaces are assumed, a singular parallel current may appear in the vicinity of a rational surface satisfying $m\psi'_P - n\psi'_T = 0$ to satisfy the local MHD equilibrium [73]. In reality, the magnetic island will appear and the pressure profile will be flattened. Then the singular parallel current on the rational surface may disappear, even if its width is sufficiently small. This means that the resonant parallel current given by Eq. (2.14) may not be realized in an actual plasma, although the pressure profile becomes complicated.

The equilibrium obtained by the VMEC may be interpreted as the one after the singular parallel current is smeared out by magnetic islands with the width comparable to a mesh size. From the view point of the smearing of singularity, the parallel current calculated with the 'direct method' seems natural. The Mercier criterion using the 'direct method' has been applied to configurations with strong magnetic shear such as Heliotron E [74] or LHD, and have shown that Mercier parameter, normalized such that the shear term becomes 1/4, predicts the behavior of low-n ideal interchange

modes. Therefore, the Mercier criterion considered is reliable at least for an equilibrium with a finite magnetic shear. From the numerical point of view, Eq. (2.14) has an advantage, since the radial derivative, which sometimes degrades numerical accuracy, is not necessary. However, it has a disadvantage that the number of magnetic surfaces, where the resonant parallel current flows increases for an equilibrium whose magnetic shear is finite. According to several comparisons of the Mercier criterion between 'direct' and 'indirect' methods have shown that the difference between them is fairly small for the regions apart from the low order rational surfaces in the magnetic sheared configurations [75]. Therefore, the 'direct method' is considered to be plausible in this thesis.

2.4 Divertor

Concerning the particle and energy exhaust for steady state operation of stellarator fusion reactors, there is the concept of a natural divertor [13, 76]. All coils in the LHD are superconducting and, therefore, a steady state ($\sim$ 1 day) operation will be possible provided that impurity concentration is kept small. For this purpose, a divertor configuration is required to control the impurity level. Also, the divertor will be important in enhancing the core energy confinement like the H mode. Tokamak experiments have shown that an effective divertor requires a divertor configuration that the plasma in the divertor region plugs neutrals recycled at the divertor plate through ionization, which minimizes the neutral flux into the main plasma. This is particulary important in·realizing a high density, cold divertor plasma and for access to the H mode regime [77]. Edge recycling control by the divertor seems to be the key factor to trigger and maintain the H mode phase in tokamaks and stellarators as expected from L - H transition theory explained in Chapter 4. The LHD energy confinement scaling [3] predicts that a factor of 2-3 improvement will be needed to have a stellarator fusion reactor with a reasonable size (major radius $\lesssim$ 20 m). Thus, an enhancement of the energy confinement is one of the major experimental subjects in the LHD project.

The field line structure has also been investigated in the design activity of the W7-X [14]. It is governed by the formation of five helical edges at the plasma boundary as a consequence of the optimization procedure [78]. These helical edges are given by the lines connecting positions of the strongest poloidal curvature on the plasma boundary; the edges run from the lower end of the bean shaped cross section via the tip of the triangular cross section to the upper end of the bean shaped cross section one period apart. The field line diversion (in the stochastic region outside the last closed magnetic surface) occurs close to these edges so that regions at a distance of about 1/5 plasma radius away are envisaged as an open divertor. A critical issue for controlling the divertor region is the modification of the magnetic field structure by finite plasma pressure, as pointed out in Ref. [14]. Therefore, divertor plates or neutralizer plates must be designed to cover finite beta equilibrium configurations. In this thesis, the magnetic field line structure is studied only for vacuum helical axis configurations.
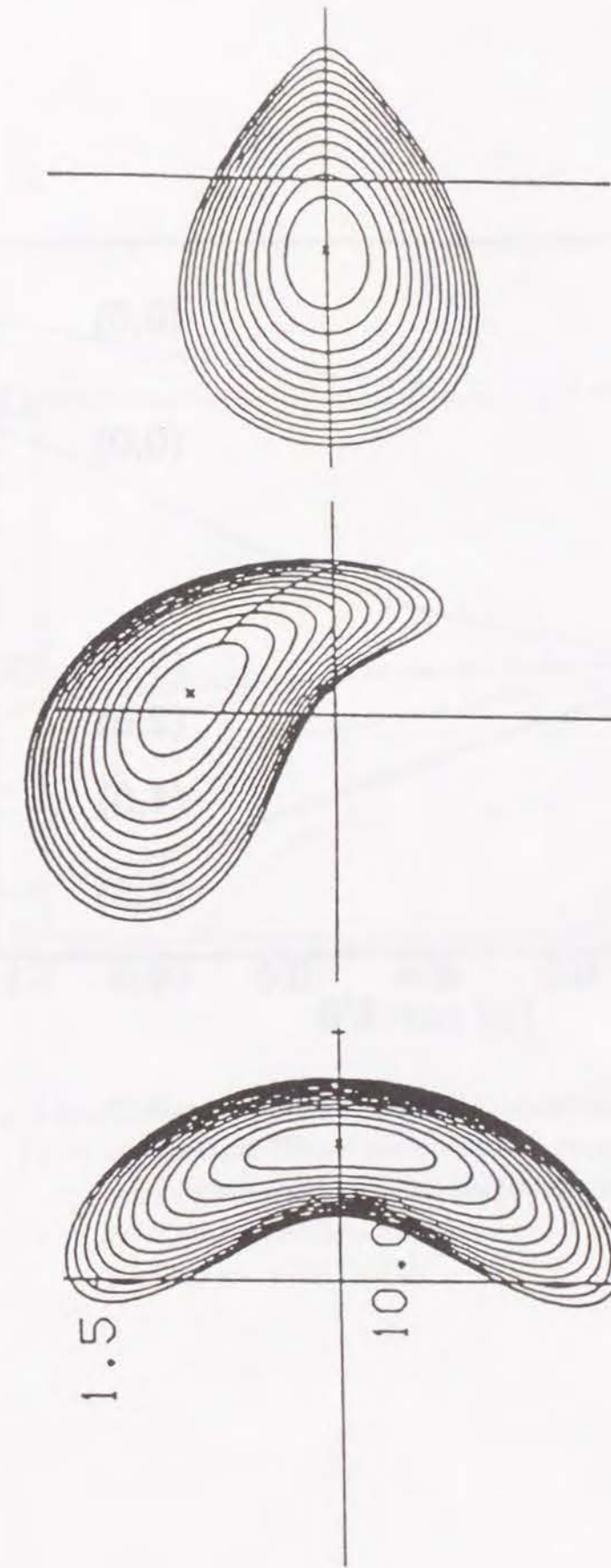

Fig. 2.1: Cross sections of magnetic surfaces of the W7-X at $\langle \beta \rangle = 5\%$. Plasma radius is normalized as approximately unity [14].
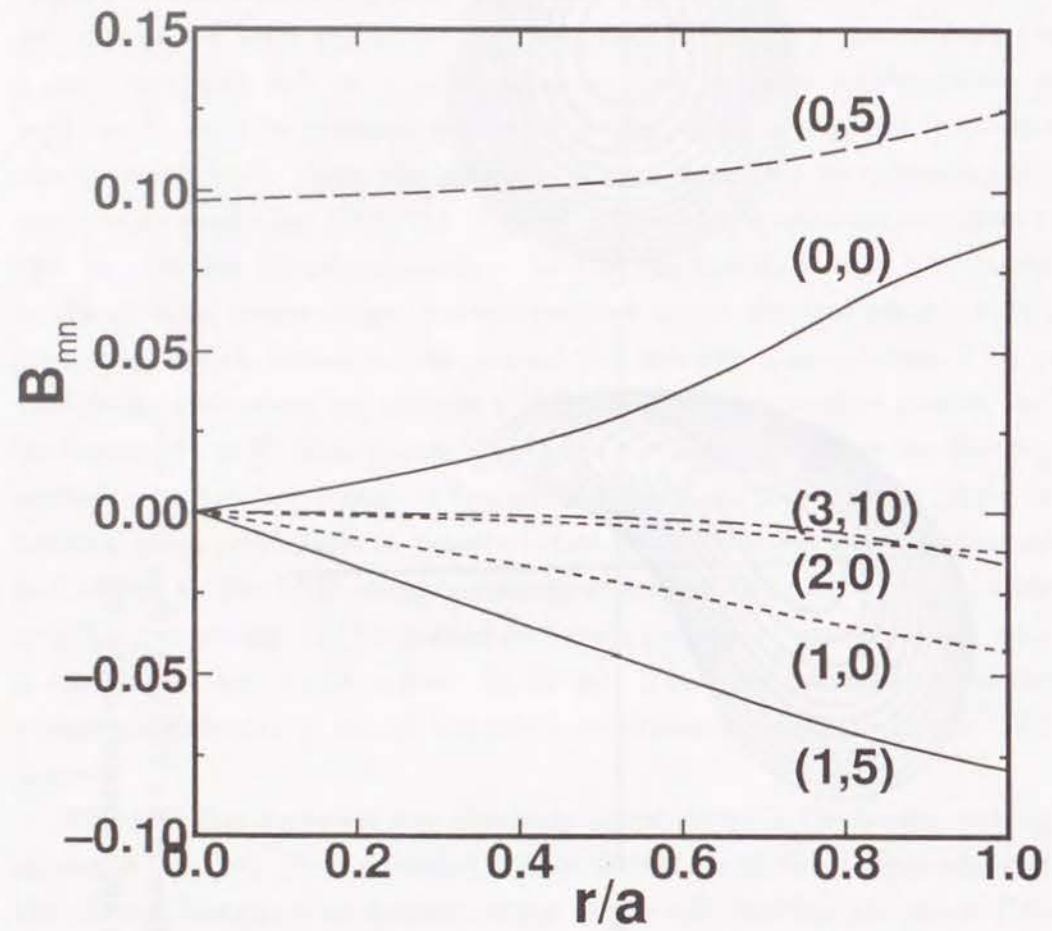
B$_{mn}$ 0.15

(0,5)

0.10

(0,0)

0.05

0.00

(3,10)

(2,0)

−0.05

(1,0)

(1,5)

−0.10

0.0 0.2 0.4 0.6 0.8 1.0

r/a

Fig. 2.2: Fourier spectrum of the magnetic field strength $\{B_{mn}\}$ in the Boozer coordinates for the W7-X [14], where m (n) denotes a poloidal (toroidal) mode number.
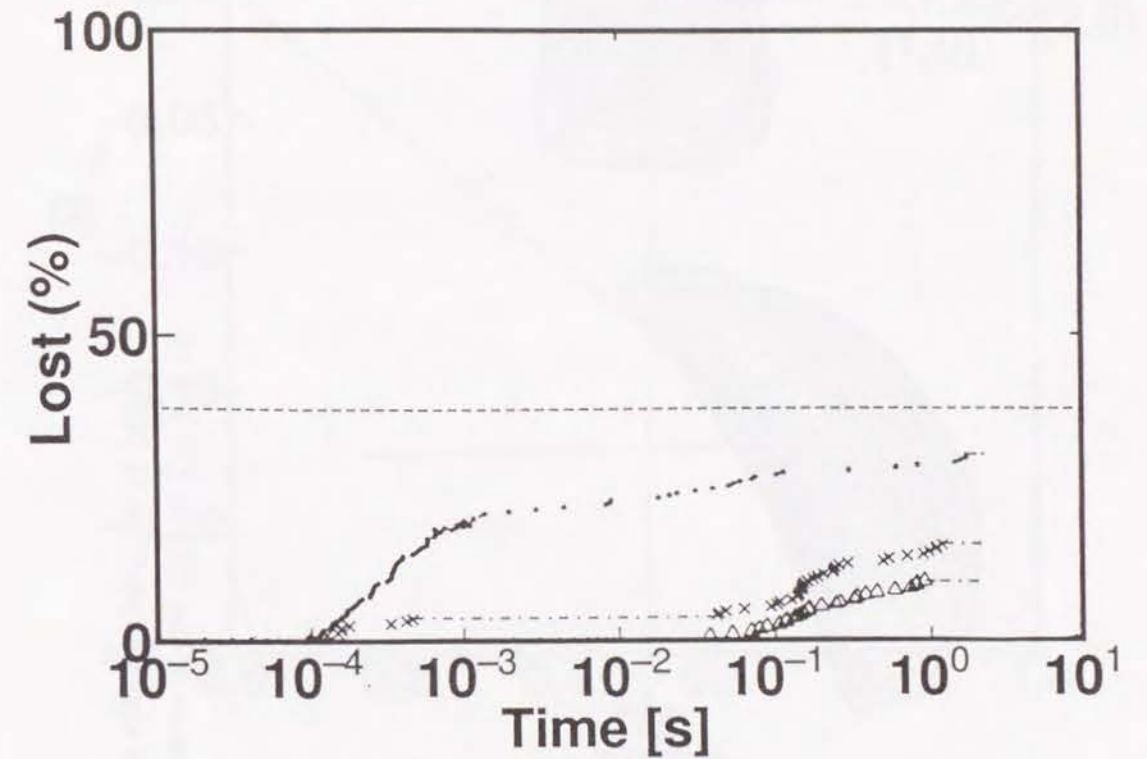
100

Lost (%) 50

0

10^{-5} 10^{-4} 10^{-3} 10^{-2} 10^{-1} 10^0 10^1

Time [s]

Fig. 2.3: Collisionless α particle losses in the W7-X magnetic configuration as a function of time of flight. Particles are launched from aspect ratio 40. The dashed line shows the fraction of trapped particles. Each symbol indicates the loss of one α particle for $\langle \beta \rangle = 0\%(\bullet)$, $2.4\%(\times)$ and $4.9\%(\triangle)$ [31].
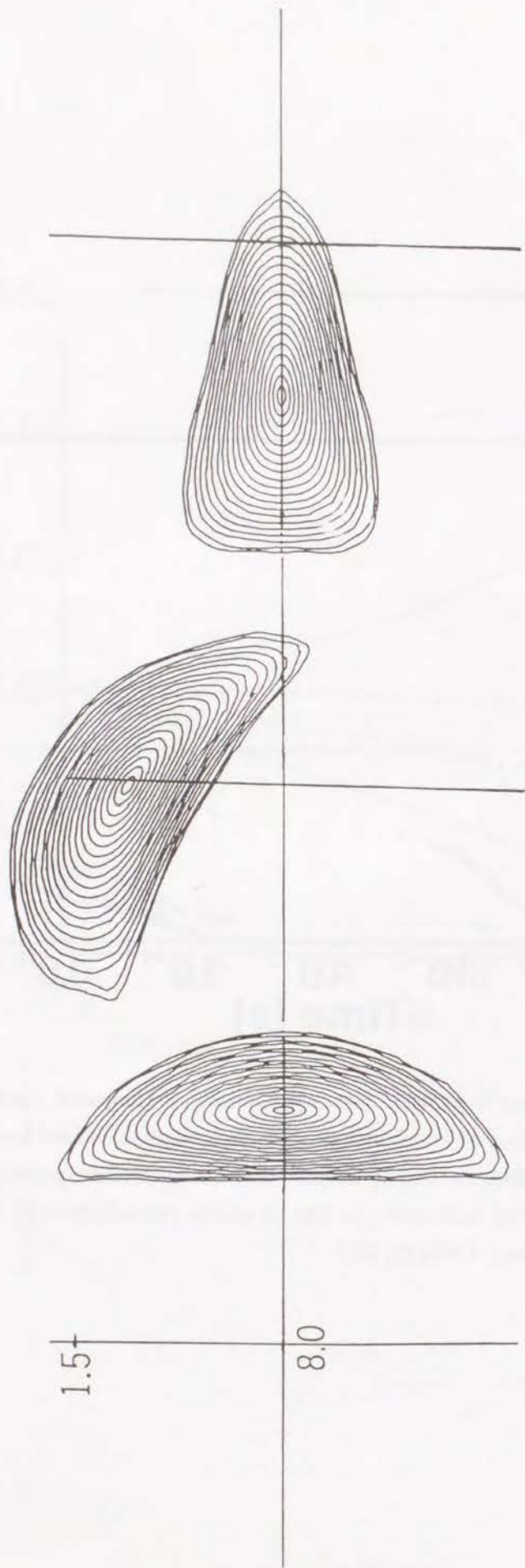
Fig. 2.4: Cross sections of magnetic surfaces of the HSX at $\langle \beta \rangle = 0.7\%$. Plasma radius is normalized as approximately unity [32].
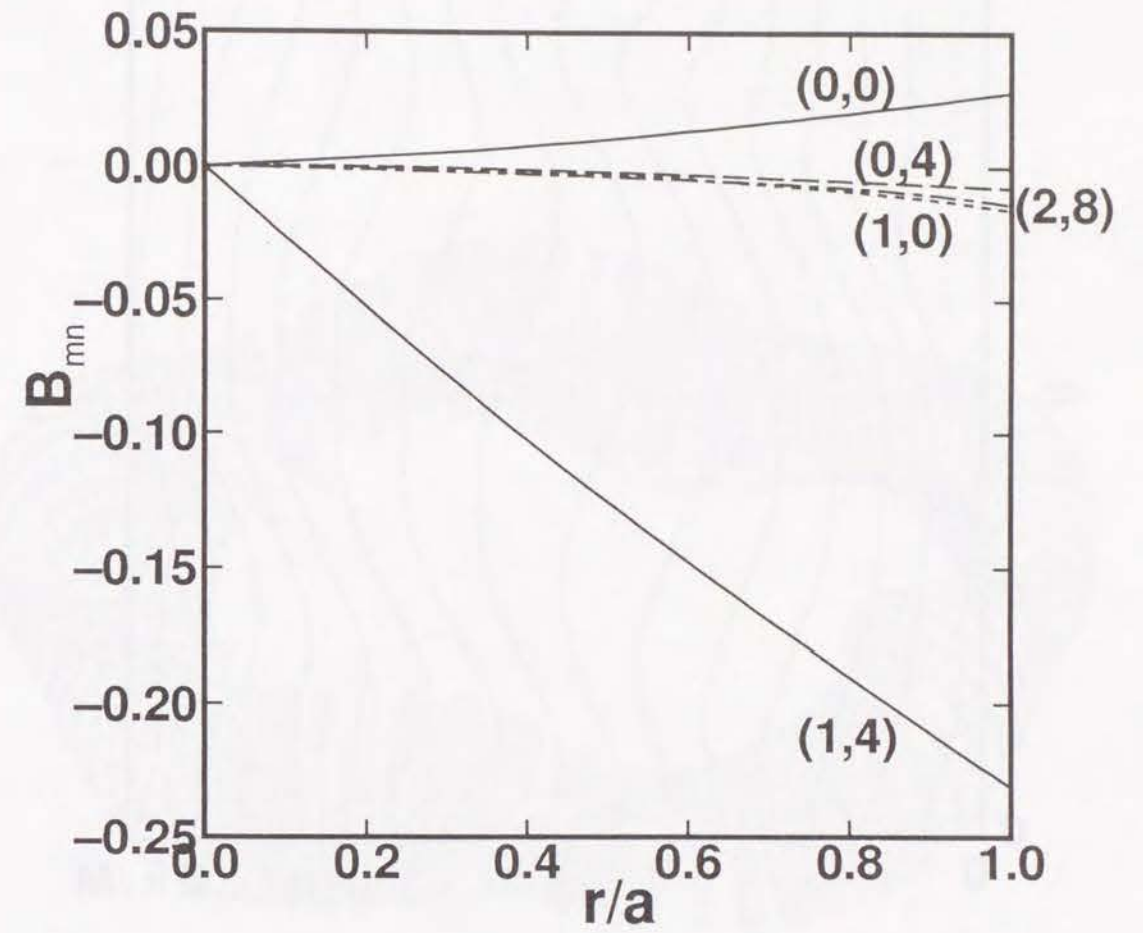

Fig. 2.5: Fourier spectrum of the magnetic field strength in the Boozer coordinates for the HSX [32].
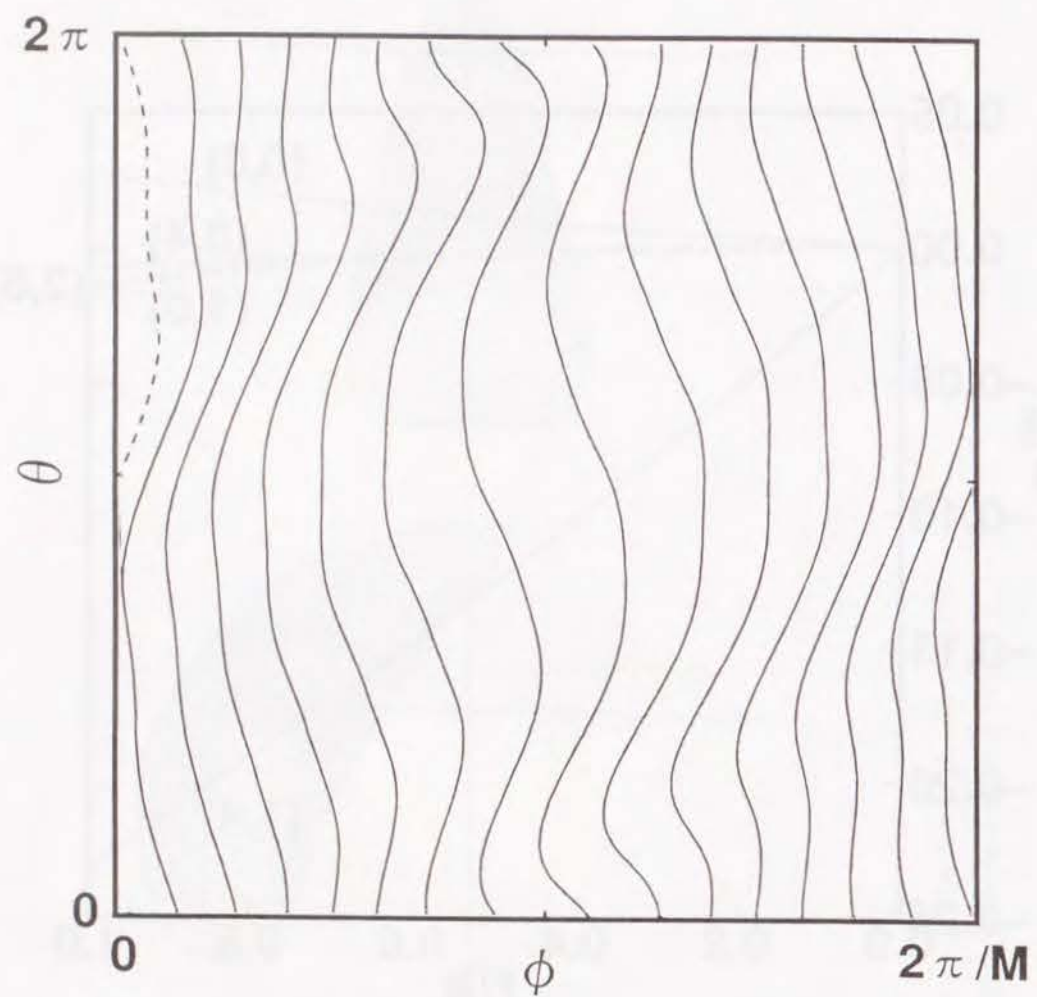
Fig. 2.6: Surface current lines of Helias vacuum magnetic field in the geometrical toroidal (ϕ) and poloidal (θ) plane [35].
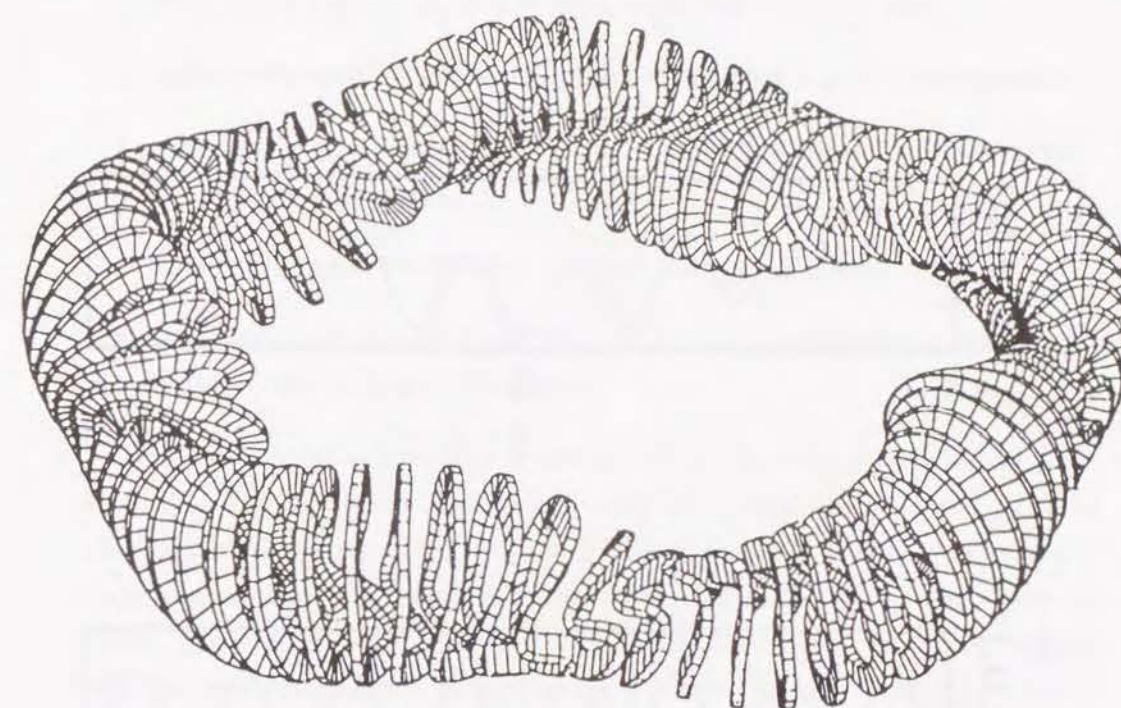

Fig. 2.7: Modular coils for the W7-X based on the surface current lines in Fig. 2.6. Number of coils per period is 15 and the aspect ratio of coil configuration is 6.5 [35].
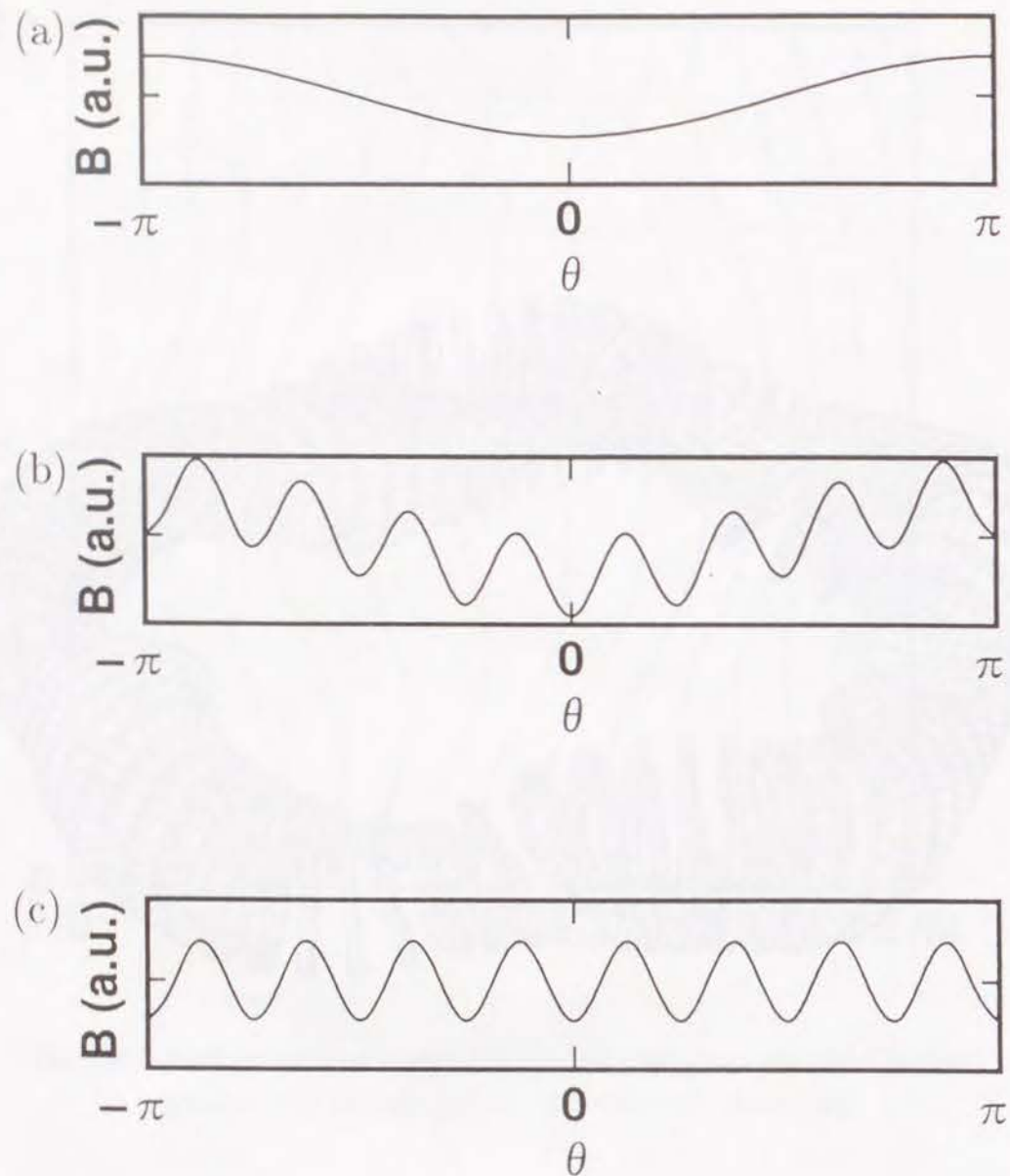
Fig. 2.8: Variation of the magnetic field strength along the field line for (a) axisymmetric tokamak, (b) conventional stellarator and (c) quasi-helically symmetric stellarator, respectively.

3 Helical Axis Stellarator Configurations Based on the $l = 1$ Helical Coil

3.1 Introduction

For an optimized stellarator configuration, the following conditions are primarily necessary:

1. sufficiently high beta MHD equilibrium and stability limit,

2. sufficiently small neoclassical plasma losses for a good confinement,

3. sufficiently small bootstrap current for keeping good magnetic surfaces in finite beta plasmas,

4. sufficiently good confinement of high energy particles,

5. good technical feasibility of the coil system and sufficiently large space between the coils and the plasma.

Here, the object is to realize a helical axis configuration with above properties based on an $l = 1$ helical coil with additional toroidal and poloidal coils for flexible experiments. It is well known that the helical magnetic axis configuration can be produced by an $l = 1$ helical coil [79] and there are several experimental devices with helical magnetic axis. In Heliac devices [80], the toroidal coils are placed along a helical line surrounding a central ring and bean shaped magnetic surfaces are produced with both the toroidal coils and the central ring.

The main criteria for the first optimization are as follows:

(a) quality of vacuum magnetic surfaces,

(b) realization of the simple field spectrum in the Boozer coordinates,

(c) the magnetic well in the whole plasma region in the vacuum configuration.

Here, the criterion (a) means to avoid low order resonant surfaces and to make the width of the magnetic island narrow, which are significant for good MHD equilibrium. Criterion (b) is relevant for good particle orbit confinement and

reduction of neoclassical transport and (c) is inevitable for MHD stability in the weak shear configuration.

It has been tried to suppress the toroidal component of the magnetic spectrum in the Boozer coordinates, as pursued in the optimization procedure of the W7-X magnetic configuration. In Section 3.2, relations between the characteristics of the magnetic field spectrum and the $l = 1$ helical coil system are explained. The investigation of the $l = 1$ helical coil system has led to a new helical axis stellarator called Helias-Heliac Hybrid Stellarator (HHHS) [17]. Both Helias-like and Heliac-like configurations are possible by adjusting the coil currents. For the Heliac-like configuration, the volume average stability beta limit is greater than 7.3% and neoclassical transport is reduced to some extent due to the reduction of the magnetic field ripple by controlling the bumpy field component.

However, the neoclassical transport is not optimized due to the enhancement of magnetic field ripple in the outside of a torus or the large bumpy field component with the same sign as the $l = 1$ helical one, although the toroidal component in the magnetic field is reduced significantly in the Helias-like configuration. Therefore, the other stellarator configuration has been investigated with the pitch modulation of an $l = 1$ helical coil different from that in HHHS to realize the bumpy component having the opposite sign to the $l = 1$ helical one to weaken the magnetic field ripple, which results in the reduction of neoclassical transport. The obtained magnetic field configuration is almost comparable to the W7-X from the point of views of beta limit, neoclassical diffusivity, bootstrap current and high energy particle confinement, although vacuum magnetic surfaces look different from the W7-X in the real space.

The coil configuration and the vacuum magnetic surfaces are described in Section 3.2. Characteristics of MHD equilibrium and Mercier stability are explained in Section 3.3, and the collisionless particle orbit confinement and neoclassical transport properties are described in Section 3.4, where collisionless particle orbits, their modifications due to finite beta and radial electric field effects are investigated. It is also shown that the bumpy field component is essential for the reduction of neoclassical diffusivity and the control of bootstrap current. Concerning particle and energy exhaust for the long pulse or steady state operation as will be pursued in the next generation experimental devices, divertor configuration will be an important ingredient.

Therefore, magnetic field line structure outside the nested magnetic surfaces is studied in Section 3.5. A brief summary for the optimized helical axis configurations will be given in Section 3.6.

3.2 Relations Between the $l = 1$ Coil System and the Vacuum Magnetic Surfaces

The major radius of the $l = 1$ helical coil wound on a axisymmetric torus R_{maj} is assumed 2.3 m, which is comparable to that of the Heliotron E [7]. This value is chosen for reference of a medium size experimental device. The winding law of the filament helical coil is as follows:

$$\theta = -\theta_0 + \frac{M}{l}\phi - \alpha \sin \frac{M}{l}\phi, \qquad (3.1)$$

where θ (ϕ) is the geometrical poloidal (toroidal) angle, respectively, and α is the pitch modulation parameter. When α is positive and becomes fairly large, the helical coil winds rapidly in the poloidal direction at outside of a torus. This pitch modulation plays an important role to control the magnetic field spectrum and/or to form the vacuum magnetic well as explained below.

In addition to the $l = 1$ helical coil, at least one pair of vertical field (or poloidal field) coils and toroidal coils are necessary to produce nested magnetic surfaces. The vertical field coils are placed at 3.5 m of radius and 1.2 m of height, symmetrically up and down the equatorial plain. Their positions are also the same as those in the Heliotron E.

The axisymmetric toroidal field component is characterized by the parameter

$$\gamma \equiv B_{t\phi}(0)/B_{h\phi}(0),$$

where $B_{h\phi}(0)$ is the average toroidal field produced at $R = 2.2$ m by the helical coils and $B_{t\phi}(0)$ by the toroidal coils.

The first aim is to suppress the toroidal field component in the magnetic spectrum and to realize a similar magnetic field configuration to that of the W7-X. The toroidal field component denoted by ϵ_t can be reduced by setting α positive as shown in Table 3.1, where examples with the field period of $M = 6$ are given. Here the average position of the magnetic axis $\langle R_{ax} \rangle$ is adjusted at 2.2 m to compare several magnetic configurations systematically. It is seen that the geometrical inverse aspect ratio for the outermost magentic surface and the value of ϵ_t at the plasma edge $\epsilon_t(a)$ obtained from the magnetic field spectrum in the Boozer coordinates are almost the same for the case of $\alpha = 0$ (no pitch modulation). On the other hand, in the case of $\alpha = 0.7$, $\epsilon_t(a)$ is reduced to about 1/6 of the geometrical inverse aspect ratio, although the average plasma minor radius becomes small.

These results are favorable to realize the magnetic configuration with a suppressed toroidal field component. However, as listed in Table 3.1, larger α makes the magnetic hill higher, which is the unfavorable direction to the MHD stability. Therefore, the next aim is the formation of the vacuum magnetic well or the reduction of the vacuum magnetic hill by changing other coil parameters for the fixed $\alpha = 0.7$.

The following coil parameters are changed to control the magnetic hill:

(a) the number of the field period (M),

(b) the minor radius of the helical coil (a_c),

(c) the axisymmetric toroidal field strength (γ)

for the fixed $\langle R_{ax} \rangle = 2.2$ m.

Figures 3.1 show the variation of vacuum magnetic hill height as a function of average radius when the above parameters are changed. These figures suggest that smaller M, a_c and γ are compatible with lowering the magnetic hill height. However, smaller M, a_c and γ make the excursion of the magnetic axis Δ larger. Here Δ is defined by the radial distance between the outermost position of the magnetic axis and the innermost one. The variation of Δ is shown in Fig. 3.2.

Figure 3.3 shows the coil system generating both the Helias-like and Heliac-like configurations schematically (HHHS with $l = 1$ and $M = 4$). The outer $l = 1$ helical coil has been included to form the magnetic well at the vacuum, although the coil current is relatively small compared to that of the inner one [81]. In Fig. 3.3, the finite coils are shown to clarify shape and structure of the helical coils, although filamentary coils are used to calculate the magnetic field.

For the toroidal field, four toroidal coils are placed per field period with the same interval in the toroidal direction as shown in Fig. 3.3, where they are shown only for one field period for simplicity. The toroidal coil currents are distributed as

$$I_{TF} = I_0(1 + C_4 \cos 4\phi + C_8 \cos 8\phi) \qquad (3.2)$$

for controlling the bumpy field component actively to reduce the neoclassical transport and to control the bootstrap current especially in the *lmfp* regime.

For the case of $\alpha > 0$, both the Helias-like and Heliac-like configurations are possible by controlling parameters γ, C_4 and C_8. Some coil parameters

are summarized in Table 3.2 in the case of the average magnetic field of 1 T on the magnetic axis for both (a) Helias-like and (b) Heliac-like configurations. Figures 3.4 show the cross section of vacuum magnetic surface for both (a) Helias-like and (b) Heliac-like configurations at $\phi = 0$, $(1/4)(2\pi/M)$ and $(1/2)(2\pi/M)$ obtained by the field line tracing code. The magnetic surfaces change from the bean shaped to tear-drop shaped to triangular in one half of a field period as shown in Fig. 3.4(a). This behavior is similar to Helias configuration for the W7-X. On the other hand, in Fig. 3.4(b), the bean shaped magnetic surfaces rotate in the toroidal direction, which looks like the Heliac configuration such as the TJ-II and the H-1 [82]. It is noted that the excursion of the magnetic axis for both configurations is fairly large, especially in Helias-like configuration. The distance between the outermost position of the axis (at the $\phi = 0$ cross section) and the innermost position (at the $\phi = (1/2)(2\pi/M)$ cross section) is about 1.3 m, which is about half of the major radius of this device. Therefore, the inner $l = 1$ helical coil may be considered as the central ring in the coil system of Heliac, although the large pitch modulation of the $l = 1$ helical coil with $M = 4$ makes a square shape from the bird's-eye view as shown in Fig. 3.3.

It is possible to suppress the toroidal field component ϵ_t with positive pitch modulation α; however, the bumpy field component ϵ_b has a tendency to have the same sign as the helical field component ϵ_h, resulting in an enhancement of the magnetic field ripple along the magnetic field line. This is unfavorable to reduce the neoclassical transport and, therefore, it has been tried to make the sign of ϵ_b opposite to that of ϵ_h.

The bumpy field component can be controlled by changing the pitch modulation parameter α as shown in Table 3.3, where the ratio of the bumpy field component to the helical one at minor radius of 0.12 m, ϵ_b/ϵ_h, is listed for different α. Here the average position of the magnetic axis $\langle R_{ax} \rangle$ is adjusted at 2.3 m with the other coil parameters fixed. The negative value of ϵ_b/ϵ_h corresponds to that the bumpy component has the opposite sign to the helical one. Although this ratio is still positive, it seems that the negative pitch modulation has a tendency to make the sign of ϵ_b opposite to that of ϵ_h, where ϵ_h is negative. It should be noted that in addition to α, the parameters C_4 and C_8 in Eq. (3.2) are also utilized to realize $\epsilon_b/\epsilon_h < 0$.

The vacuum magnetic hill height at average radius of 0.12 m is also listed in Table 3.3. It is suggested that the negative pitch modulation has a ten-

dency to form the vacuum magnetic well. This is because the magnetic field lines have a tendency to advance mainly in the toroidal direction and, therefore, stay longer inner side of a torus or in the region of the strong magnetic field due to the pitch modulation of the helical coil. For the $\alpha < 0$ case, the outer helical coil, which is introduced to make the vacuum magnetic well for positive pitch modulation case such as HHHS (cf., Fig. 3.3), is not necessary. Thus the coil system becomes much simpler than that of HHHS and gives a wider space for the heating and diagnostics. This is a significant advantage of this coil system for designing a new experimental device.

From these properties of magnetic surface, it is expected to obtain a helical axis configuration with a reduced neoclassical ripple transport and a good Mercier stability simultaneously based on the $l = 1$ helical coil having the negative pitch modulation. This configuration will be called as the "optimized" helical axis configuration in this thesis. The coil parameters for the optimized helical axis configuration are summarized in Table 3.4 and the schematic view of the coil system is shown in Fig. 3.5.

The cross section of the vacuum magnetic surfaces are shown in Fig. 3.6 at $\phi = 0$, $(1/4)(2\pi/M)$ and $(1/2)(2\pi/M)$. The cross section changes from the triangular to tear-drop and to bean shaped in one half of a field period, which has a similarity to magnetic surfaces of the W7-X or the Helias-like configuration in HHHS. However, the bean shaped magnetic surface is located in the inner region of a torus with respect to the position of the $l = 1$ helical coil in contrast to the W7-X, where it is located in the outer region of a torus.

In Fig. 3.6, contours of magnetic field strength are also shown, and the center of the concentric circles corresponds to the position of filamentary $l = 1$ helical coil. It is seen that the space between the outermost magnetic surface and the helical coil is rather wide and this is desirable for the reduction of impulities from the plasma facing components.

Finally, it should be mentioned that, for example, the finite size $l = 1$ helical coil with cross section of 10 cm × 10 cm does not affect the vacuum magnetic characteristics significantly.

In the following of this chapter, the three magnetic configurations mentioned above are discussed. They are characterized as follows from the point of view of the magnetic field spectrum as shown later:

Helias-like: significantly reduced ϵ_t
                and large ϵ_b with the same sign as ϵ_h.
Heliac-like: ϵ_t almost comparable to the geometrical inverse aspect
                ratio and several small helical magnetic field components,
Optimized: ϵ_t almost comparable to the geometrical inverse aspect
                ratio and large ϵ_b with the opposite sign to ϵ_h.

3.3 Currentless MHD Equilibria and Mercier Stability

The 3D MHD equilibrium code VMEC [57] has been applied to calculate currentless equilibria and Mercier criterion. The pressure profile is assumed as

$$P = P_0(1 - \psi_T^2)$$

for the Helias-like and Heliac-like configurations and

$$P = P_0(1 - \psi_T^2)^2$$

for the optimized helical axis configuration, where ψ_T is a normalized toroidal flux function.

It is noted that the average minor radius of the last closed magnetic surface of the vacuum configuration is about 0.25 m in Fig. 3.6, which gives an aspect ratio less than 9. However, as seen from Fig. 3.6, the peripheral magnetic surfaces are distorted by the $(m, n) = (5, 4)$ magnetic islands at $\iota = 0.8$ and these highly shaped magnetic surfaces are difficult to be treated in the VMEC with limited number of Fourier modes for representing the outermost magnetic surface. Therefore, the average minor radius is assumed to be about 0.20 m for the input data for the VMEC. It may be interpreted that a pressureless plasma exists in the region between 0.20 m and 0.25 m. However, the fixed boundary condition at 0.20 m is assumed in the VMEC for simplicity. As a future study, a free boundary equilibrium calculation of the considered helical axis stellarators is needed to check the assumption of a fixed boundary. For the currentless equilibria of the LHD, it is confirmed that the difference between the free boundary and the fixed boundary is small, if the plasma column position is fixed by the vertical field control [83].

Figures 3.7 show the rotational transform profiles for (a) Helias-like, (b) Heliac-like and (c) optimized helical axis configurations. The rotational transform is high at around 1.8 and the profile almost does not change as the beta value is increased for the Helias-like configuration. On the other hand, in the Heliac-like and optimized helical axis configurations, the rotational transform is medium at around 0.7 with weak shear at the vacuum and the profile changes significantly as the beta is increased. This implies that PSC is not reduced compared to the standard stellarator or the toroidal component in the magnetic spectrum is not reduced from the geometrical inverse

aspect ratio as shown later. This characteristic is totally different from that of the W7-X, in which PSC is significantly reduced to yield high $\langle \beta \rangle_{eq}$ limit by suppressing the toroidal component in the magnetic spectrum.

The PSC causes the magnetic axis shift or Shafranov shift which depends on beta value as shown in Figs. 3.8 for (a) Helias-like, (b) Heliac-like and (c) optimized helical axis configurations. It is extremely small for the Helias-like configuration as shown in Fig. 3.8(a). This means that the significantly reduced PSC is realized due to negligibly small toroidal component in the magnetic spectrum. By assuming that the equilibrium beta limit $\langle \beta \rangle_{eq}$ corresponds to the magnetic axis shift or Shafranov shift equal to the half of minor radius, $\langle \beta \rangle_{eq} \sim 7.3\%$ is obtained for the Heliac-like configuration and $\langle \beta \rangle_{eq} \sim 4.5\%$ for the optimized helical axis configuration, which are satisfactory for an aim of obtaining $\langle \beta \rangle_{eq} \sim 5\%$. Also, the finite magnetic axis shift contributes to the magnetic well in finite beta plasmas, which is favorable to the stabilization of pressure-driven modes.

When an MHD equilibrium is obtained numerically, it is useful to evaluate Mercier criterion [84] for localized interchange instabilities which is shown as $D_M > 0$ for stability. The value of D_M is negative for the Helias-like configuration even in the low beta equilibrium, which means that this configuration is unstable to Mercier modes. The main stabilizing term in the low shear configuration like the Helias-like configuration is the magnetic well term. Therefore, the Helias-like configuration requires a deeper vacuum magnetic well for stabilizing the Mercier modes. On the other hand, the Heliac-like configuration is stable to Mercier modes up to at least $\langle \beta \rangle_{eq} \sim 7.3\%$ as seen from Fig. 3.9. For less broad pressure profile such as $P = P_0(1 - \psi_T^2)^2$ and $P = P_0(1 - \psi_T)^2$, $\langle \beta \rangle_{eq} \sim \langle \beta \rangle_{st} \sim 4.6\%$ and 2.3% are obtained for this configuration, respectively. This behavior that the broader pressure profile gives the higher beta limit is different from the Mercier stability for the TJ-II [68].

The optimized helical axis configuration is stable to Mericer modes up to $\langle \beta \rangle_{eq}$ due to the formation of the vacuum magnetic well ($\sim 0.2\%$) and an enhancement of the magnetic well due to the Shafranov shift. Thus $\langle \beta \rangle_{st} \sim \langle \beta \rangle_{eq} \gtrsim 4.5\%$ is obtained in this configuration.

These beta limit for the Heliac-like and optimized helical axis configurations are close to that of the W7-X, although a little broader pressure profile is favorable here and only the ideal Mercier criterion is considered.

3.4 Collisionless Particle Orbit and Neoclassical Transport

Collisionless particle orbit has been studied by using the guiding center drift equations in the Boozer coordinates for both the vacuum and finite beta plasmas. Since the coordinate system used in the VMEC is not the Boozer coordinates, the coordinate transformation of the magnetic field strength to the Boozer coordinates is necessary particularly for finite beta plasmas.

The magnitude of the magnetic field is expressed as

$$B = \sum_{mn} B_{mn}(r) \cos(m\theta_B - n\zeta_B),$$

where θ_B (ζ_B) is the poloidal (toroidal) angle in the Boozer coordinates and r denotes an average radius. The Fourier spectra of the magnetic field strength in the Boozer coordinates are shown in Figs. 3.10 for both (a) Helias-like and (b) Heliac-like vacuum configurations and Figs. 3.11 for (a) vacuum and (b) $\langle \beta \rangle \sim 4.5\%$ for the optimized helical axis configuration. Here it is noted that B_{00} line denotes the difference of B_{00} between at r and the magnetic axis, $B_{00}(r) - B_{00}(0)$. All other components are normalized with $B_{00}(0)$. The significant feature in the Helias-like configuration is the extremely small toroidicity B_{10} and the large bumpy component B_{04} with the same sign as the helical component B_{14}. On the other hand, in the Heliac-like configuration, the reduction of B_{10} is rather weak, although the B_{04} is reduced substantially.

In the optimized helical axis configuration, the large bumpy component B_{04} has the opposite sign to helical component B_{14}, and this structure is similar to that of the W7-X [14] except that B_{10} is not reduced from the geometrical inverse aspect ratio. This relation of B_{04} and B_{14} makes the magnetic field ripple localized inside of a torus i.e., in the strong magnetic field region with $\theta \sim \pi$, which improves the trapped particle confinement. It is noted again that the B_{00} line, which represents the difference $B_{00}(r) - B_{00}(0)$, has a tendency to have a large gradient toward the plasma edge in the finite beta case as seen in Fig. 3.11(b). This behavior reflects the diamagnetic effect and it is the main effect of the finite beta in the optimized helical axis configuration. The broadening of the spectrum which is often considered in conventional stellarators [45] is not seen.

For studying collisionless particle orbits, 1500 protons with a kinetic energy of 1 keV are followed under the assumptions that the average magnetic

field strength of 1 T on the magnetic axis and $\rho_i/R \sim 2 \times 10^{-3}$. Here ρ_i is the proton Larmor radius and R is the major radius. It is noted that $\rho_i/R \sim 2 \times 10^{-3}$ corresponds to 53 keV proton in the W7-X with the average magnetic field strength of 5 T. They were initially launched from the magnetic surface located at $r/a = 0.5$ with a uniform distribution in the pitch angle of the velocity space (15 points), in the poloidal (10 points) and in the toroidal (10 points) angles. The particle orbits were followed for 2 ms (a particle with only parallel velocity or $v_\perp = 0$ initially makes about 60 circuits of the torus) or until they cross the plasma boundary. It is better to follow them for the order of one second in order to study the particle confinement corresponding to α particles definitively. For studying the direct loss, the orbit following for 2 ms is an allowable choice, which also saves computational time. Since the radial electric field E_r is effective in confining trapped particles in heliotron/torsatrons [85], the E_r is included in the orbit following calculation. A parabolic profile of the electric potential Φ is assumed to give E_r,

$$\Phi = \Phi_0(1 - \psi_T), \tag{3.3}$$

where ψ_T is a normalized toroidal flux function. The particle loss rates for several conditions for the three types of helical axis configuration are summarized in Table 3.5. It is clarified that the radial electric field is necessary to obtain the good particle confinement for low beta plasmas; however, the particle confinement may be improved without radial electric field for finite beta plasmas. These results are similar to the particle confinement property of Helias for the W7-X [31].

In obtaining the loss rates shown in Table 3.5, particles are assumed to be lost when they cross the plasma boundary. In reality, there is a possibility that some particles reenter the plasma without striking the plasma facing components [86]. Therefore, it is probable that the loss rates listed in Table 3.5 are overestimated.

The reason for the large loss fraction in Helias-like configuration at the vacuum may be understood by a simple analytic model. From Fig. 3.10(a), the magnetic field strength in the Helias-like configuration is simply approximated by

$$B = B_0[1 - \epsilon_b \cos 4\phi - \epsilon_h \cos(\theta - 4\phi)],$$

where $B_0 = B_{00}(0)$, and $\epsilon_b = B_{04}/B_0$ and $\epsilon_h = B_{14}/B_0$ are bumpy and dominant helical field components, respectively. Then the banana center

drift equations are expressed approximately as

$$\dot{\theta} \propto -\cos\theta,$$
$$\dot{r} \propto r\sin\theta,$$

under the conditions that $|\epsilon_b| \gg |\epsilon_h|$, and ϵ_b and ϵ_h have the same sign [45]. This set of equations has the same (r, θ) dependence as that for the usual toroidal drift of the guiding center. Therefore, it is said that the reduction of toroidal component in the magnetic spectrum is not effective to improve the trapped particle orbits when the bumpy field component is large and has the same sign as the dominant helical field component.

It should be noted that the loss rate in the vacuum case for the optimized helical axis configuration without radial electric field E_r becomes smaller than that of the Helias-like configuration by realizing the bumpy field component with the opposite sign to the helical one to make the variation of the magnetic field strength along a field line flat - bottomed like σ - optimization [46].

The physical mechanism for the results listed in Table 3.5 is understood from orbit modifications due to finite beta and radial electric field effects in the optimized helical axis configuration as an example.

Figures 3.12 show the contours of the magnetic field strength $|B|$ on the outermost magnetic surface for one field period (left) and the variation of the magnetic field strength along the magnetic field line on that surface (right) for (a) vacuum and (b) $\langle \beta \rangle \sim 4.5\%$ cases. There is a large modulation of the envelop in the vacuum case, although the minimum point of $|B|$, which determines the deeply trapped particle orbit, is almost aligned by the control of the bumpy field component. However, the modulation amplitude of the envelop decreases in the $\langle \beta \rangle \sim 4.5\%$ case, mainly due to the decrease of both the toroidal and helical field components compared to the bumpy component and the realization of "quasi-bumpy symmetry" as shown in Fig. 3.11(b). This variation of the magnetic field strength along a field line is similar to that of axisymmetric tokamak (Fig. 2.8(a)) or quasi-helically symmetric stellarator (Fig. 2.8(c)). Therefore, it is expected that the trapped particle orbit confinement is improved for finite beta plasmas.

Figures 3.13 show typical orbit of (a) untrapped, (b) trapped and (c) transition particle in the vacuum field. The pitch angles, $\eta \equiv \cos^{-1}(v_\parallel/v)$, are 0, $\pi/2$ and $17\pi/24$, respectively. Here, "E_{para} [keV]" denotes the parallel energy measured in keV taking into account the relative direction of the particle velocity to the magnetic field and "phi" and "$theta$" denote ϕ_B and θ_B

in the Boozer coordinates, respectively. The circle on (r, z) plane corresponds to the outermost magnetic surface in the Boozer coordinates. The transition particle experiences both trapping and detrapping states during the particle motion.

The particle classification in the velocity space is also shown for the vacuum field case. Figures 3.14 show the classification of particles which start from (a) $\theta_{B0} = 0$ and (b) $\theta_{B0} = \pi$. The notation $\bigcirc$ denotes the untrapped particle, $\triangle$ the trapped particle and $\times$ the loss particle. It is obvious that the loss cone has a tendency to become wider as the particle starting points become located nearer to the outermost magnetic surface. This is due to the increase of the trapped particle fraction mainly because B_{10} increases radially. This tendency is the same as that typically seen in conventional stellarators. It should be noted that the particles starting from $(\theta_{B0}, \phi_{B0}) = (\pi, 0)$ do not cross the outermost magnetic surface within the orbit following time of 2 ms, and trapped particle fraction is extremely small compared to other cases even for $r/a = 0.8$. Therefore, this region seems appropriate for the neutral beam injection (NBI), although it is located inner side of a torus.

It is well known that the radial electric field is effective to improve particle orbit confinement in stellarators due to $\boldsymbol{E} \times \boldsymbol{B}$ poloidal drift [85]. Typical drift orbits of the trapped particle with $\rho_i/R \sim 2 \times 10^{-3}$ in the presence of the electrostatic potential, Eq. (3.3), are shown in Figs. 3.15 for several Φ_0 values. It is noted that the positive Φ_0 value means the outward radial electric field. In the absence of the radial electric field ($\Phi_0 = 0$), the trapped particle drifts vertically and leaves the confinement region (this particle is the same one as in Fig. 3.13(b)). However, the electric potential of either sign whose value is relatively small compared to the kinetic energy of particles gives sufficient poloidal rotation by the $\boldsymbol{E} \times \boldsymbol{B}$ drift faster than the ∇B drift, and the trapped particle moves around the magnetic axis without loss.

In order to see clearly the influence of finite beta effects on the trapped particle orbits, orbits of deeply trapped particles with $\rho_i/R \sim 6 \times 10^{-4}$ are shown in Figs. 3.16 for several beta values. This value of ρ_i/R corresponds to the proton with kinetic energy of 0.1 keV in the case of average magnetic field strength of 1 T on the magnetic axis. They cross the outermost magnetic surface in a few ms for (a) $\langle \beta \rangle = 0\%$ and (b) $\langle \beta \rangle = 1.4\%$; however, it takes about 80 ms to cross it for (c) $\langle \beta \rangle = 2.9\%$ and (d) $\langle \beta \rangle = 4.5\%$. It is noted that the B_{00} line denotes the difference, $B_{00}(r) - B_{00}(0)$, in Fig. 3.11 and it

has a larger gradient in finite beta case than in vacuum case, which reflects the diamagnetic effect. Contours of $min_{\phi_B} |B|$ have a tendency to be closed due to the diamagnetic effect and thus the deeply trapped particles may be confined for a longer time in finite beta plasmas, where $min_{\phi_B} |B|$ denotes the minimum of $|B|$ averaged over ϕ_B coordinate in the Boozer coordinates. It is noted that the deeply trapped particles with 1 keV may cross the outermost magnetic surface in a time shorter than about 80 ms for 0.1 keV in the case of the average magnetic field strength of 1 T on the magnetic axis or $\rho_i/R \sim 6 \times 10^{-4}$. In order to realize a compact stellarator reactor with a reasonable magnetic field, more optimization for high energy trapped particle confinement should be pursued with a careful control of the bumpy field.

In order to study transport properties, the DKES code [47] has been used to evaluate neoclassical transport coefficients, particle diffusion and bootstrap coefficients. They can be evaluated as functions of inverse mean free path at a fixed particle velocity, ν/v, where ν is the collision frequency and v is the particle velocity. Figure 3.17 shows particle diffusivity D calculated at the magnetic surface corresponding to the half radius as a function of ν_*, where D denotes diffusivity normalized with the plateau value of diffusivity of each equivalent tokamak and ν_* is the effective collision frequency obtained by multiplying the connection length qR or R/ι with ν/v, where q is a safety factor. Here the equivalent tokamak has the same aspect ratio, the same rotational transform and the same average magnetic field strength as each helical axis configuration considered here. For comparison, the results for the W7-X [14] and the TJ-II [87] are also shown. In the Helias-like configuration, the bumpy component B_{04} has the same sign as the helical component B_{14} as shown in Fig. 3.10(a), which enhances the magnetic field ripple in the weak magnetic field region or in the outer region of a torus. Therefore the diffusivity becomes larger than the plateau value of its equivalent tokamak.

On the other hand, diffusivity of the Heliac-like configuration is reduced to some extent by the bumpy field control, especially by the parameter C_4, and is almost comparable to the TJ-II results. However, the neoclassical diffusivity is still larger than the W7-X in which the plateau level is almost the same or less than that of its equivalent tokamak. Further suppression of the neoclassical diffusivity has been tried in the optimized helical axis configuration by controlling the bumpy field component based on the analytical results for $1/\nu$ ripple transport described in Chapter 2.

The particle flux in the low collisional regime, Eq. (2.11), includes the product of ϵ_h and ϵ_b in the expression of ϵ_H, which implies that the $1/\nu$ particle flux is affected by the relative sign of ϵ_h and ϵ_b. To confirm this, the contours given by the integral in the bracket of Eq. (2.11) which depends only on the geometrical parameters are shown in Fig. 3.18. The horizontal axis denotes ϵ_t/ϵ_h and the vertical one ϵ_b/ϵ_h. The origin $(0,0)$ corresponds to the configuration with $\epsilon_t = \epsilon_b = 0$, i.e., quasi-helically symmetric stellarator such as the HSX. Around the origin, the particle flux Γ has a minimum value. The normalized contour values are $4, 2, 1, 1, 2, 4, 6, 8, 10$ successively on the line from the point $(\epsilon_t/\epsilon_h, \epsilon_b/\epsilon_h) = (0.0, -2.0)$ to the point $(1.0, 1.0)$. For reference, the W7-X case is also plotted by a symbol $\bullet$ in the same figure. The main characteristics of the magnetic field structure of the W7-X is the reduction of the toroidicity ($\epsilon_t/\epsilon_h \sim 0.5$) and the bumpy component with almost the same magnitude and with the opposite sign to the helical one ($\epsilon_b/\epsilon_h \sim -1.2$). This combination makes the $1/\nu$ particle flux small, although there are two other field components (i.e., ϵ_t and ϵ_b) breaking the helical symmetry. It is clearly seen that not only the reduction of ϵ_t but also ϵ_b with the opposite sign to ϵ_h is effective to reduce the neoclassical ripple transport especially at $|\epsilon_t/\epsilon_h| \sim 1$ case. Thus it has been tried to obtain ϵ_b with the opposite sign to ϵ_h for the optimized helical axis configuration.

It should be noted that Fig. 3.18 is applicable only for magnetic configurations with $l = 1$ helical component dominantly and, therefore, $l = 2$ stellarators such as the LHD and the Heliotron E can not be considered with this figure. That is because the side bands of the main helical component with $(m, n) = (2, M)$ are not toroidicity with $(m, n) = (1, 0)$ and the bumpy component $(m, n) = (0, M)$ in $l = 2$ stellarators.

Figure 3.19 shows diffusivity D calculated by the DKES code at the magnetic surface corresponding to the half radius as a function of an effective collision frequency ν_*, where the radial electric field is assumed to be negligibly small. Here the results for Heliac-like configuration is also shown again for reference. It is noted that D denotes diffusivity normalized by the plateau value of its equivalent tokamak. It is seen that the plateau diffusion is almost comparable to that of its equivalent tokamak. When the bumpy component B_{04} is disregarded artificially in the DKES code (cf., "$B_{04} = 0$" line) to see the role of B_{04} clearly, the plateau diffusion and $1/\nu$ diffusion increases with a factor of 2-3. Therefore, it is confirmed that the bumpy

component with the opposite sign to the helical one is effective to reduce the neoclassical transport as expected from analytical results described above. The optimized helical axis configuration is plotted with a symbol $\bigcirc$ in Fig. 3.18, and it is not far from the W7-X. It is noted that the Helias-like and Heliac-like configurations are beyond this range of ϵ_t/ϵ_h and ϵ_b/ϵ_h.

The effect of the radial electric field on the $1/\nu$ ripple transport is also studied with the DKES code by assuming non-zero value of E_r/v. From Fig. 3.15, it is seen that the electric potential with $\Phi_0 \sim \pm 0.2$ kV affects the trapped particle orbits significantly. Therefore, $E_r/v \sim 3 \times 10^{-3}$ V·s/m^2 is assumed, which corresponds to $\Phi_0 \sim 0.25$ kV for protons with kinetic energy of 1 keV. This can be explained as following. The velocity of 1 keV proton is about 4.4×10^5 m/s. When E_r/v is taken to be 3×10^{-3} V·s/m^2, $E_r \sim E_r/v \times (4.4 \times 10^5) \sim 1.3 \times 10^3$ V/m. On the other hand, from the simple calculation, the radial electric field is $E_r \sim \Phi_0/a \sim 1.25 \times 10^3$ V/m for $\Phi_0 \sim 0.25$ kV and plasma minor radius $a \sim 0.2$ m. The diffusivity in the $lmfp$ regime is shown in Fig. 3.20 at the magnetic surface corresponding to the half radius as function of an effective collision frequency ν_*, where the results for zero E_r/v case is also shown for reference. The $1/\nu$ diffusivity reduces about a factor of 2-3 even with a relatively small electric potential compared to the particle energy in the low collisionality regime. In this regime, the approximation of "collisionless" is rather well valid, and therefore, the physical mechanism for the diffusivity reduction is seen from Fig. 3.15 that the $\boldsymbol{E} \times \boldsymbol{B}$ poloidal drift suppresses the radial motion of particles due to ∇B drift. It is noted that the radial electric field is less effective to reduce $1/\nu$ diffusivity of particles with much higher energy.

The existence of the bootstrap current has been experimentally confirmed in both tokamaks [88] and stellarators [12] and it is reported that the bootstrap current is well described by the neoclassical transport theory [89]. In tokamaks, the bootstrap current is additive to the Ohmic current. In stellarators, both the direction and the magnitude depend on the magnetic configuration [48]. In particular, in quasi-helically symmetric configuration such as the HSX, the bootstrap current is expected to flow in the opposite direction, which reduces the external rotational transform. In the ATF, the magnetic configuration was changed by superimposing a quadrupole field, resulting in the change of direction of the total bootstrap current [90].

A small or negligible bootstrap current is required in the low shear config-

uration whose rotational transform is chosen to avoid the low order rational surface. The low order rational surface appeared within the plasma may degrade the confinement property due to the formation of magnetic islands. In order to avoid the low order resonance to obtain a fairly fixed rotational transform profile, the finite pressure effects on the vacuum rotational transform must be kept small. Maassberg et al. showed the contours of the bootstrap current coefficient on the $(\epsilon_t/\epsilon_h, \epsilon_b)$ space by the DKES code under the assumption of monoenergetic particles. They clarified that the optimum region is close to $\epsilon_t/\epsilon_h \sim 0.5$ and $\epsilon_b \sim 0.1$ to realize the small bootstrap current for a wide range of collisionality [29]. The contribution of the toroidal component ϵ_t drives tokamak like bootstrap current which is approximately counterbalanced by the contribution from the helical component ϵ_h [91]. These values of magnetic spectrum, $\epsilon_t/\epsilon_h \sim 0.5$ and $\epsilon_b \sim 0.1$, is very close to those of the W7-X. Unfortunately, it is difficult to control the toroidal and bumpy components separately in the continuous $l = 1$ helical coil system because they are both satellite components of the main helical field.

Figure 3.21 shows the bootstrap current coefficient (in arbitrary unit) versus ν_* at $r/a = 0.5$ in the optimized helical axis configuration. Negative values denote that the bootstrap current flows in the same direction as that in tokamaks. The results for two cases are shown; a solid line corresponds to the results obtained by using 465 Fourier components of the magnetic spectrum and a broken line corresponds to those by assuming $B_{04} = 0$ with keeping other components in the DKES code. It is clearly seen that B_{04} has a significant effect to control the bootstrap current especially in the banana-plateau regime. Therefore, a careful control of the bumpy field component is necessary to minimize effects due to the bootstrap current on plasma confinement.

3.5 Divertor Structure

Concerning the particle and energy exhaust for realizing a steady state operation of stellarator reactor, there is the concept of a natural divertor in the heliotron device [13, 76]. The magnetic field lines outside the outermost magnetic surface are followed to investigate the possibility of a divertor configuration. They start from the points being positioned in the planes with $\phi = 0$, $(1/4)(2\pi/M)$ and $(1/2)(2\pi/M)$ and at a distance of one third of a plasma minor radius from the outermost magnetic surface in the vacuum configuration. A simple toroidal vacuum chamber is assumed with a major radius of 2.2 m and a minor radius of 1.4 m for the Helias-like and Heliac-like configurations and 1.2 m for the optimized helical axis configuration as a boundary for the field line tracing. It is noted that the inner $l = 1$ helical coil is inside this chamber. The line tracing calculation has been done for the length up to 760 m for each magnetic field line. Thus the field line which does not intersect the chamber surface has a length longer than 760 m. It should be also noted that the inner $l = 1$ helical coil is assumed to be a filamentary coil and, therefore, even if the magnetic field line strikes the finite size helical coil, the field line tracing is continued.

Traces on the magnetic field lines in the $\phi = 0$ plane are shown in Fig. 3.22(a) and traces on the toroidal chamber in Fig. 3.22(b) for the Helias-like configuration, Fig. 3.23 for the Heliac-like configuration and Fig. 3.24 for the optimized helical axis configuration.

In the Helias-like configuration, the whisker structure is clearly seen in Poincaré plots of the magnetic field lines, Fig. 3.22(a). It is expected from Fig. 3.22(b) that the traces of magnetic field lines striking the toroidal chamber are concentrated at $\theta \sim 0$ (or $\theta \sim 2\pi$), i.e., in the outer vacuum region in the toroidal chamber. Therefore, this field line structure outside the outermost magnetic surface is envisaged as an open divertor.

On the other hand, in the Heliac-like configuration, the explicit whisker structure does not exist and the magnetic surfaces are surrounded by a wide stochastic layer. These different magnetic structures outside the outermoset magnetic surface between the Helias-like and Heliac-like configurations may be useful to investigate the role of the divertor structure to, for example, the improvement of the plasma confinement. The magnetic field lines striking the chamber are concentrated at $\theta \sim 0$ (or $\theta \sim 2\pi$) also in the Heliac-like configuration. Therefore, it is easy to set up the divertor chamber in the

outer region of a torus in HHHS at least for low beta plasma experiments.

As for the optimized helical axis configuration, it is clearly seen that five whiskers are diverging from the stochastic region surrounding the nested magnetic surfaces. This structure may be related to $n/m = 4/5$ magnetic islands at $\iota = 0.8$. It is seen from Fig. 3.23(b) that magnetic field lines reaching the chamber surface are concentrated around $\theta \sim \pi/2$ and $3\pi/2$, i.e., top and bottom region of the chamber near $\phi = 1/2$ period. A typical connection length of diverted magnetic field lines to the chamber surface is longer than 100 m, which is typically comparable to that of Heliotron E. The behavior of diverted magnetic field lines in Fig. 3.23(b) may be favorable for a divertor.

3.6 Summary

It has been tried to obtain a helical axis stellarator configuration based on $l = 1$ helical coil system for a new flexible experimental device.

Wide range of magnetic configurations including the Helias-like and Heliac-like configurations are possible in the Helias-Heliac Hybrid Stellarator (HHHS) by controlling the coil currents in helical, toroidal and poloidal coils.

The main characteristics of Helias-like and Heliac-like configurations are as follows:

- **Helias-like configuration**

    – aspect ratio ~ 7,

    – high rotational transform, almost no shear, unchangeable for finite beta plasmas,

    – rather small axis shift (or Shafranov shift) for finite beta and low $\langle \beta \rangle_{st}$,

    – sufficiently reduced ϵ_t and large ϵ_b with the same sign as ϵ_h,

    – higher collisionless particle orbit loss rate,

    – large particle diffusion coefficient and small bootstrap current,

    – clear whisker structure outside the outermost magnetic surface,

- **Heliac-like configuration**

    – aspect ratio ~ 11,

    – medium rotational transform, weak shear at vacuum, easily changeable for finite beta plasmas,

    – high $\langle \beta \rangle_{eq}$ and $\langle \beta \rangle_{st}$,

    – ϵ_t is almost comparable to the geometrical inverse aspect ratio and several field components with small amplitude,

    – lower collisionless particle orbit loss rate,

    – particle diffusion coefficient comparable to TJ-II; however, large bootstrap current,

    – wide stochastic layer outside the outermost magnetic surface.

These wide range of magnetic configurations are useful for studying the role of ideal and resistive interchange modes in relation to stability beta limit by comparing the magnetic configurations between with sufficient vacuum magnetic well and without it. The experimental results in the Heliotron E [92] and the ATF [93] show that the transport is anomalous particularly in the outer edge region, where turbulent characteristics are observed. It is pointed out that the most probable candidate for the edge turbulence is the resistive interchange instabilities [53]. Therefore, it is worthwhile to study this problem experimentally with exploiting the wide range of magnetic configurations of HHHS. The consistent relation between trapped particle orbit loss and radial electric field may also be investigated by changing the beta value.

For the Helias-like configuration, since the bumpy component has the same sign as the helical component, collisionless particle orbit confinement is not good and the neoclassical ripple transport is not reduced sufficiently. Moreover, the vacuum magnetic well is not enough for the Mercier stability. The Heliac-like configuration is more attractive from the point of views of MHD stability and neoclassical ripple transport, since the magnetic well depth is sufficiently deep even in the vacuum configuration and the small bumpy component has the opposite sign to the helical component, resulting in the reduction of the magnetic field ripple in the weak magnetic field region. However, the neoclassical diffusivity is still several times larger than that of the W7-X.

The optimized helical axis configuration based on the modulated $l = 1$ helical coil has also been described, although the sign of pitch modulation of the $l = 1$ helical coil has been changed from that for the Helias-like and Heliac-like configurations. The main characteristics of the optimized helical axis configuration are as follows:

- **Optimized helical axis configuration**

  - aspect ratio ~ 8,

  - medium rotational transform, weak shear at vacuum, easily change-able for finite beta plasmas,

  - high $\langle \beta \rangle_{eq}$ and $\langle \beta \rangle_{st}$,

  - ϵ_t is almost comparable to the geometrical inverse aspect ratio and large ϵ_b with the opposite sign to ϵ_h,

  - lower collisionless particle orbit loss rate than Heliac-like configuration (cf., Table 3.5),

  - particle diffusion coefficient reduced to plateau level of its equivalent tokamak and bootstrap current controllable by the bumpy component,

  - clear whisker structure outside the outermost magnetic surface.

These approaches and obtained characteristics are essentially the same as those developed in the W7-X; however, the coil system is different from the elaborated modular coils of the W7-X, which may realize a flexible experimental device. It is different from the W7-X that the toroidal component in the magnetic spectrum is not reduced from the geometrical inverse aspect ratio, which causes a fairly large Shafranov shift. Therefore, one of future studies is to decrease this B_{10} component and to realize a more optimized magnetic configuration.

In addition to the above favorable properties for plasma confinement, the large clearance between the helical coil and the outermost magnetic surface is advantageous for plasma heating and diagnostics in designing a new experimental device.

α	0.0	0.4	0.7
$a/\langle R_{ax}\rangle$	0.164	0.075	0.072
$\epsilon_t(a)$	0.153	0.038	0.011
Hill (%) (at 0.2 m)	4.05	5.10	7.02

Table.3.1 The geometrical inverse aspect ratio ($a/\langle R_{ax}\rangle$) and toroidal field component $\epsilon_t(a)$ and magnetic hill (%) v.s. pitch modulation α with the average position of the magnetic axis $\langle R_{ax}\rangle = 2.2$ m fixed for $M = 6$ case.

Coil type		θ_0	α	maj, min radii [m]	current [MA]
helical	inner	$-\pi$	0.7	2.3, 0.19	2.805
	outer	0.0	-0.8	2.2, 1.40	-0.047
vertical					-0.383
toroidal	4/period	center [m]	radius [m]	γ, I_0 [MA], C_4, C_8	
		$R = 2.2$	1.8	0.5, 0.067, 0.0, 0.0	

Table.3.2(a) Coil parameters for the Helias-like configuration with the average magnetic field of 1 T on the magnetic axis.

Coil type		θ_0	α	maj, min radii [m]	current [MA]
helical	inner	$-\pi$	0.4	2.3, 0.19	0.556
	outer	0.0	-0.9	2.2, 1.40	-0.185
vertical					0.011
toroidal	4/period	center [m]	radius [m]	γ, I_0 [MA], C_4, C_8	
		$R = 2.2$	1.8	8.0, 0.732, 1.50, 0.0	

Table.3.2(b) Coil parameters for the Heliac-like configuration with the average magnetic field of 1 T on the magnetic axis.

α	0.0	-0.3	-0.45
ϵ_b/ϵ_h (at 0.12 m)	2.65	1.90	1.53
Hill (%) (at 0.12 m)	0.50	0.34	0.24

Table.3.3 The ratio of the bumpy component to the helical one, ϵ_b/ϵ_h, and magnetic hill (%) both at $r = 0.12$ m v.s. pitch modulation parameter α with the fixed average position of the magnetic axis $\langle R_{ax}\rangle = 2.3$ m.

Coil type		θ_0	α	maj, min radii [m]	current [MA]
helical		$-\pi$	-0.45	2.3, 0.37	1.458
vertical					-0.729
toroidal	4/period	center [m]	radius [m]	γ, I_0 [MA], C_4, C_8	
		$R = 2.2$	1.2	1.4, 0.389, 0.75, -0.875	

Table.3.4 Coil parameters for the optimized helical axis configuration with the average magnetic field of 1 T on the magnetic axis.

	Conditions	loss (%)
	$(\langle\beta\rangle(\%), \Phi_0 \text{ (kV)})$	
Helias-like	(0.0, 0.0)	31.3
	(6.4, 0.0)	14.1
	(0.0, 0.5)	0.0
Heliac-like	(0.0, 0.0)	19.5
	(4.1, 0.0)	2.2
	(0.0, 0.5)	0.0
Optimized	(0.0, 0.0)	18.1
	(2.9, 0.0)	7.3
	(0.0, 0.25)	0.4

Table.3.5 Particle loss rates for several conditions for the Helias-like, Heliac-like and optimized helical axis configurations.

(a) $(a_c=0.3[m], \gamma=1.0)$

(b) $(M=4, \gamma=1.0)$

(c) $(M=4, a_c=0.19[m])$
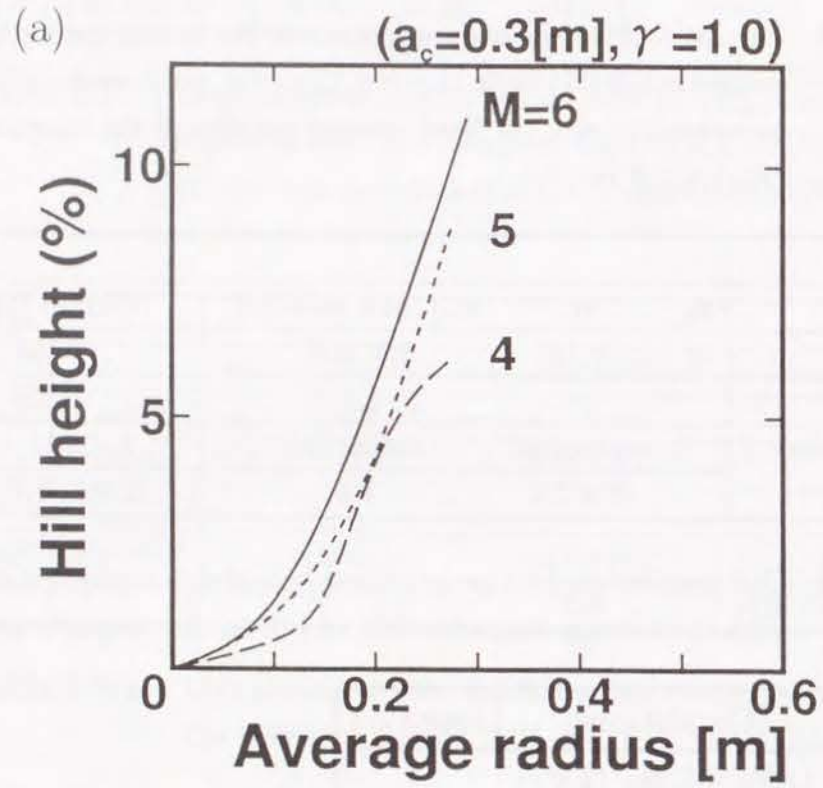
Fig. 3.1: Variations of vacuum magnetic hill as a function of average radius when (a) the number of the field period M, (b) the minor radius of the helical coil a_c and (c) the axisymmetric toroidal field strength γ are changed.
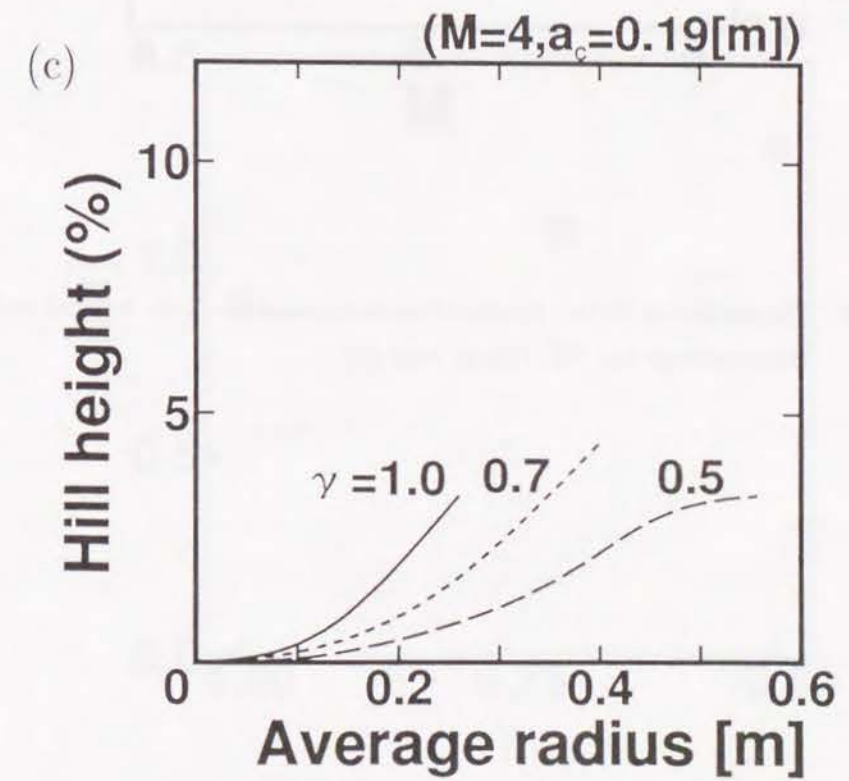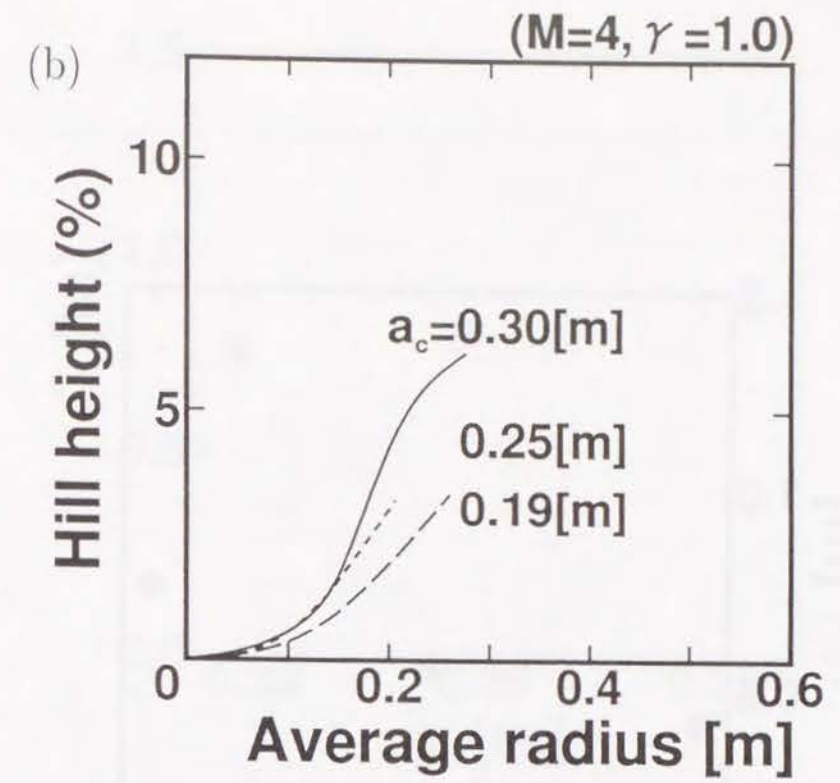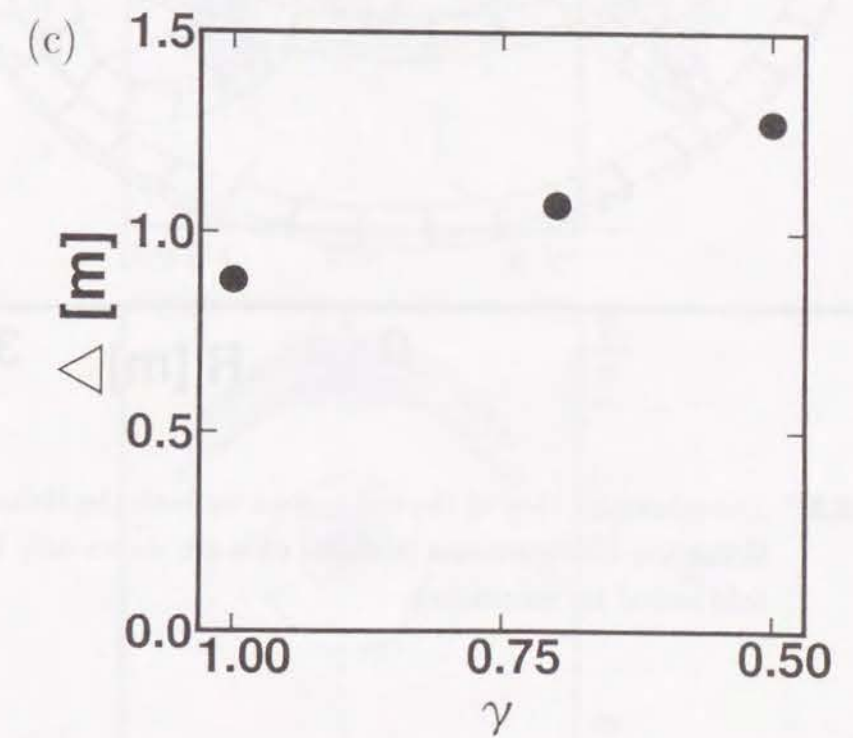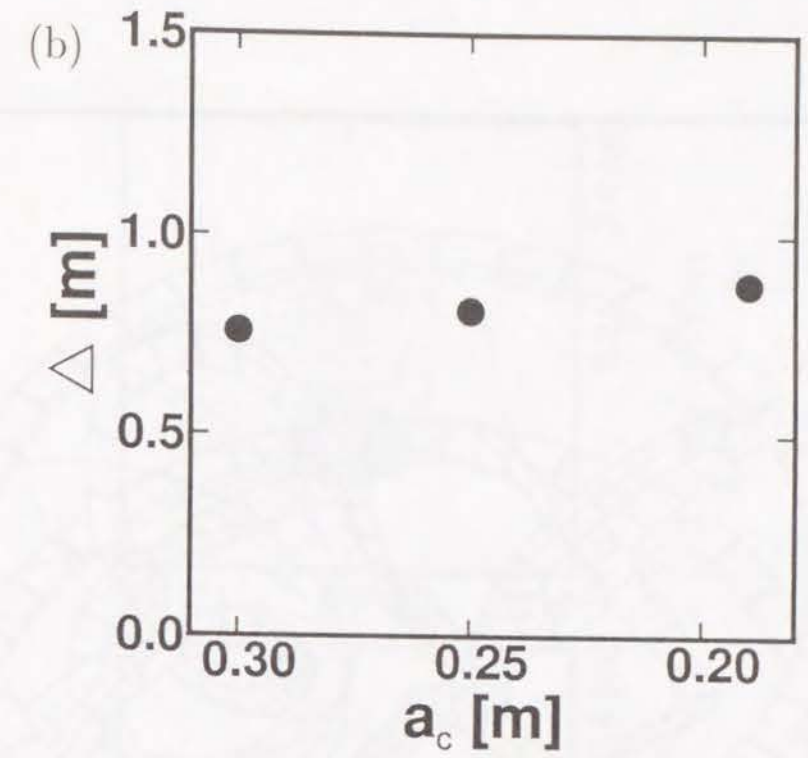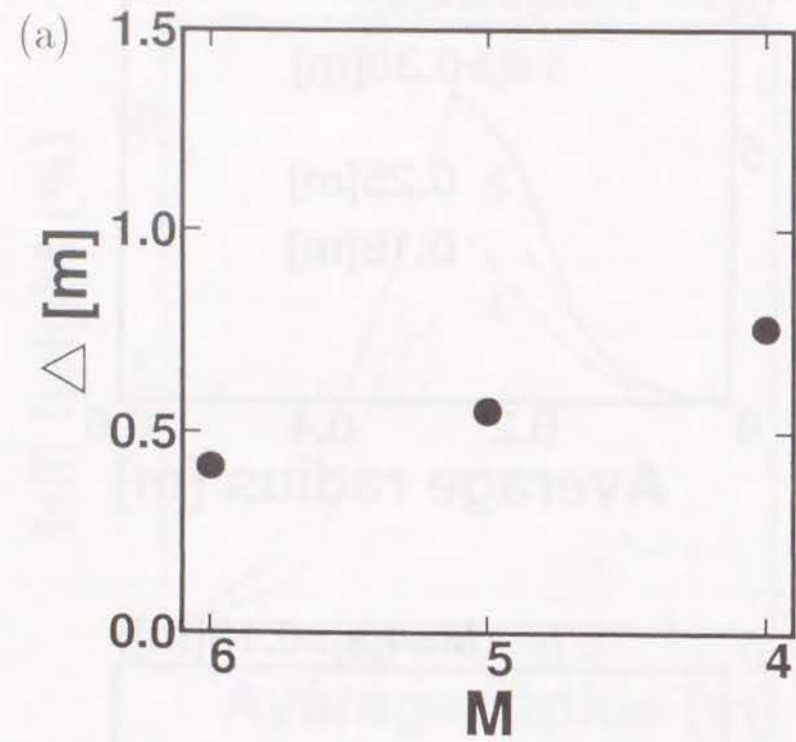
Fig. 3.2:   Dependence of the magnetic axis excursion Δ on helical coil
parameters: (a) M, (b) a_c and (c) γ.
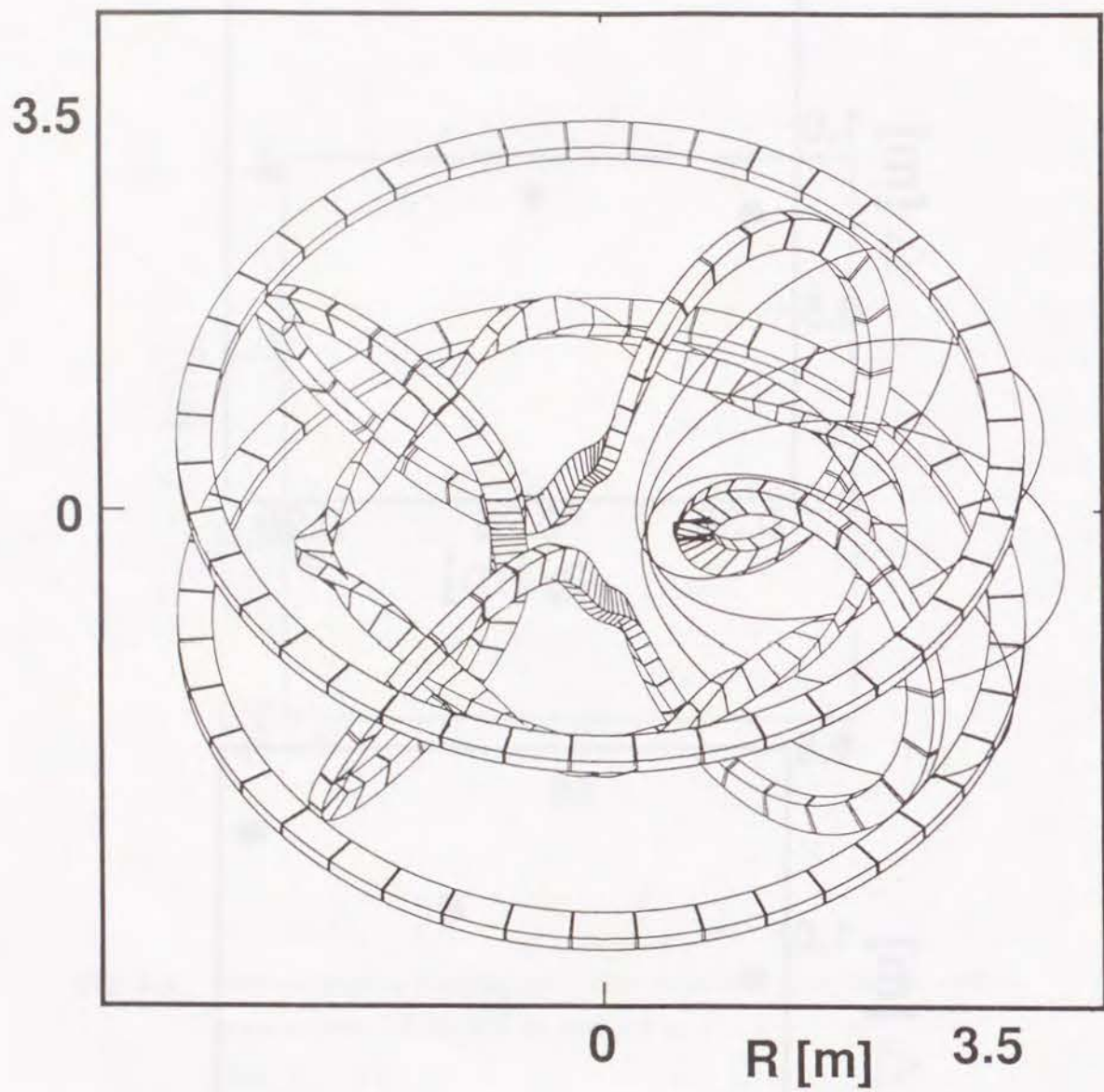
Fig. 3.3: The schematic view of the coil system for both the Helias-like and Heliac-like configurations (toroidal coils are shown only for one field period for simplicity).

$\phi = 0$ $\phi = (1/4)(2\pi/M)$ $\phi = (1/2)(2\pi/M)$

(a)
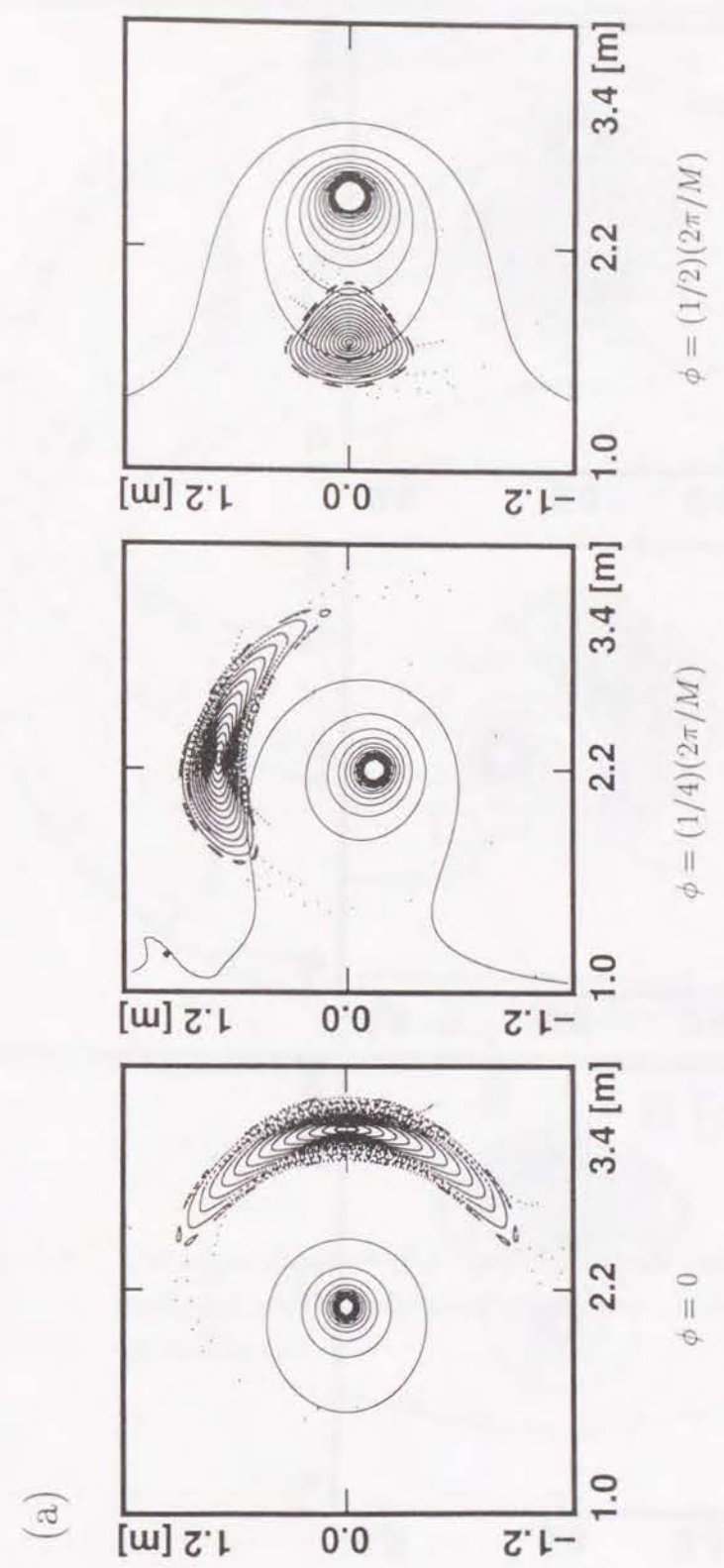
Fig. 3.4: Cross sections of vacuum magnetic surfaces of (a) Helias-like and (b) Heliac-like configurations.

(b)

$\phi = 0$

$\phi = (1/4)(2\pi/M)$

$\phi = (1/2)(2\pi/M)$
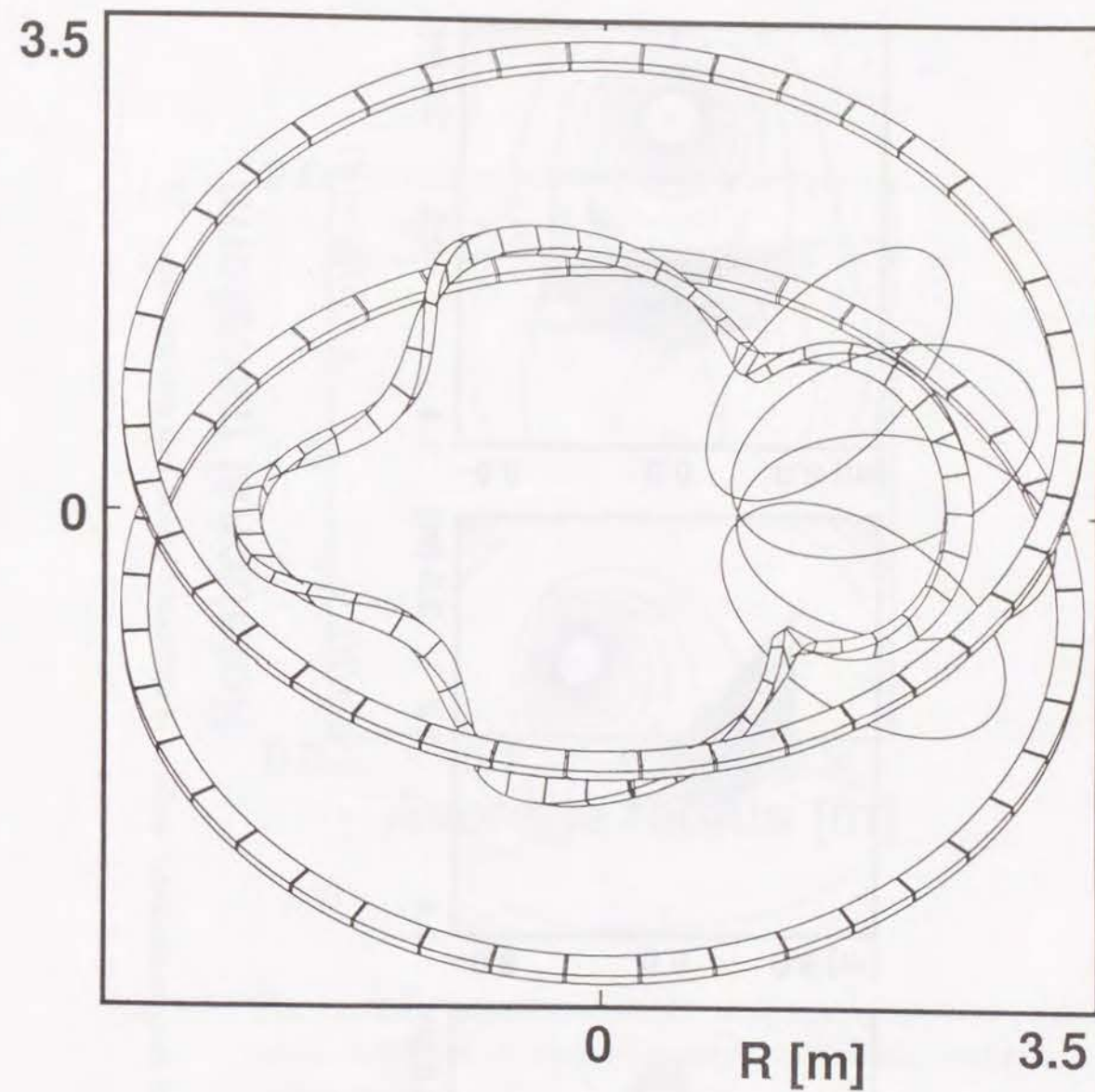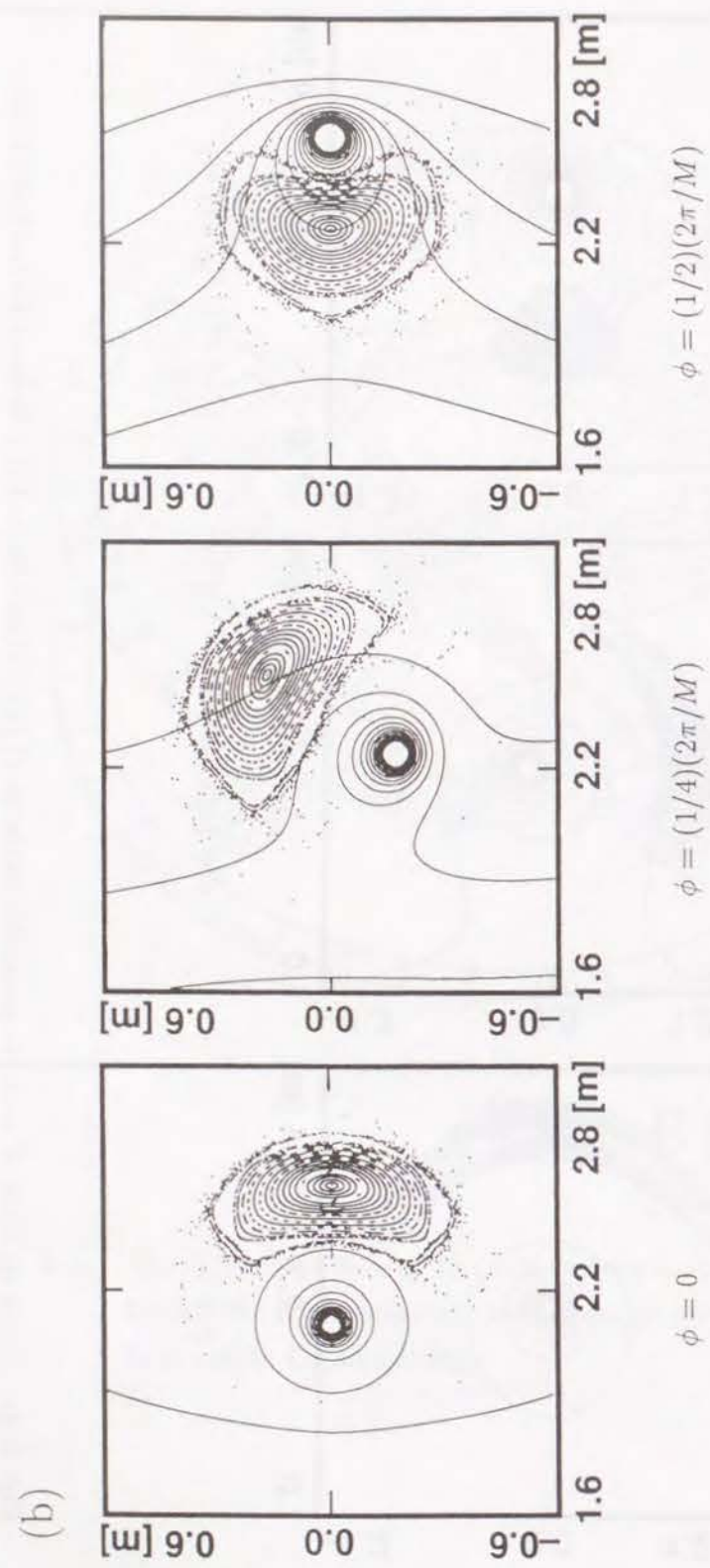
Fig. 3.5: The schematic view of the coil system for optimized helical axis configutation (toroidal coils are shown only for one field period for simplicity).
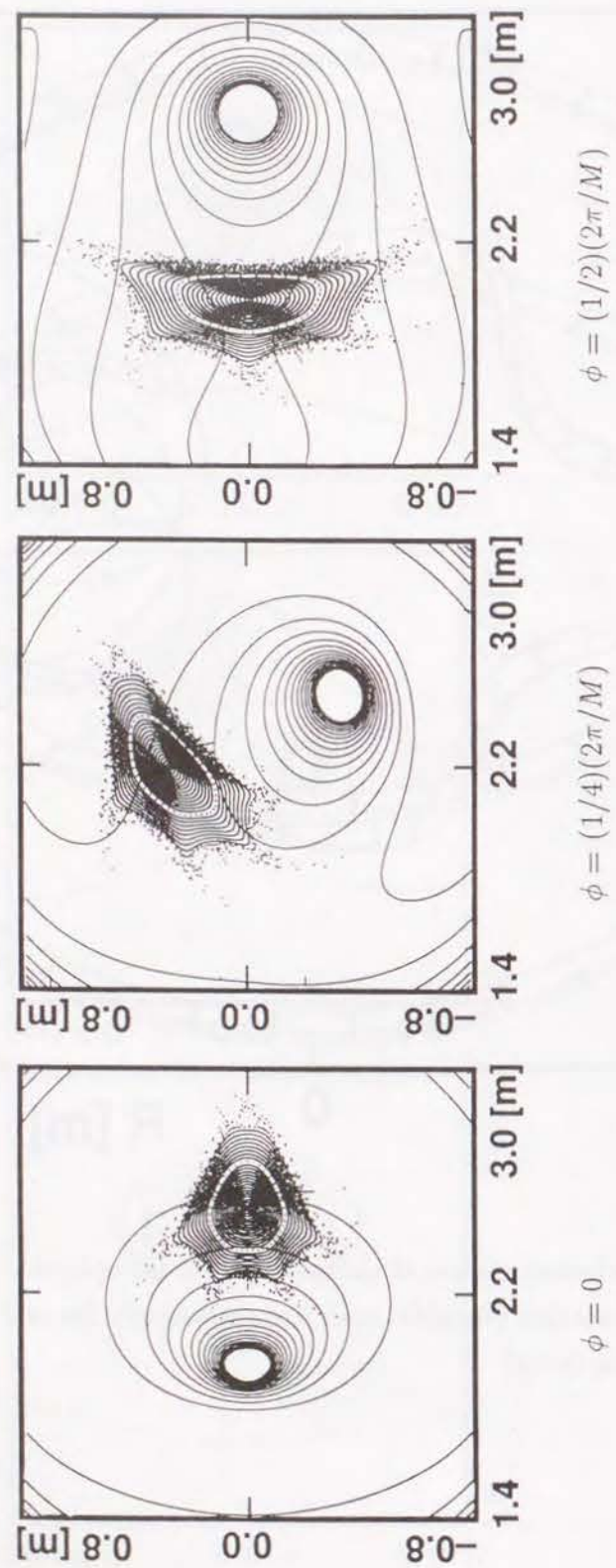
Fig. 3.6: Cross sections of vacuum magnetic surfaces of optimized helical axis configuration.

$\phi = (1/2)(2\pi/M)$

$\phi = (1/4)(2\pi/M)$

$\phi = 0$
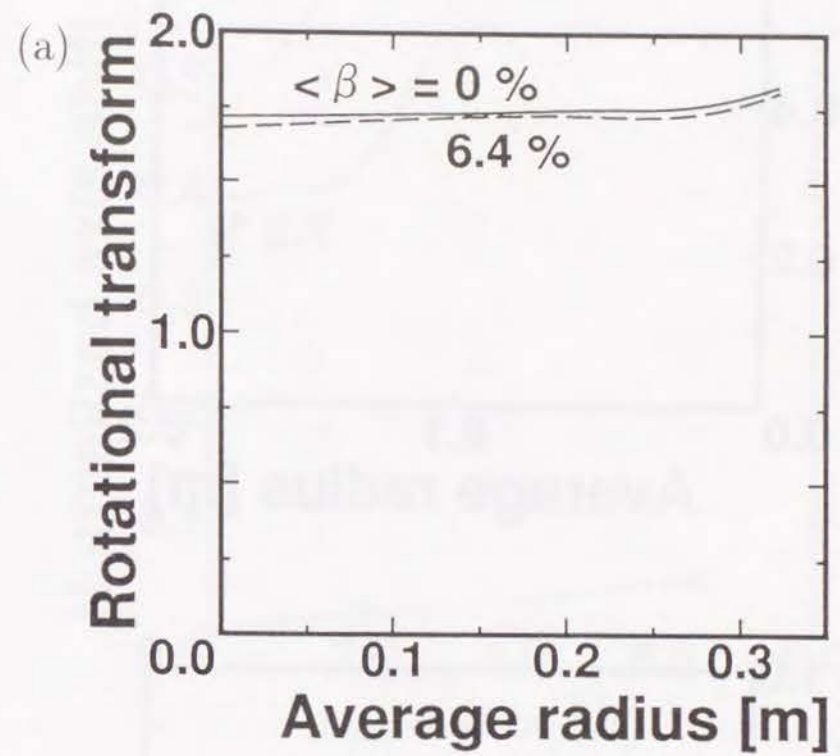
Fig. 3.7: The rotational transform profile for vacuum and finite beta plasmas for (a) Helias-like, (b) Heliac-like and (c) optimized helical axis configurations.

(b)

Rotational transform (y-axis)
Average radius [m] (x-axis)

$\langle \beta \rangle = 0\ \%$

4.1 %

7.3 %

(c)

Rotational transform (y-axis)
Average radius [m] (x-axis)

$\langle \beta \rangle = 0\%$

2.9%

4.5%

(a)

Normalized axis shift (y-axis)
$\langle \beta \rangle (\%)$ (x-axis)
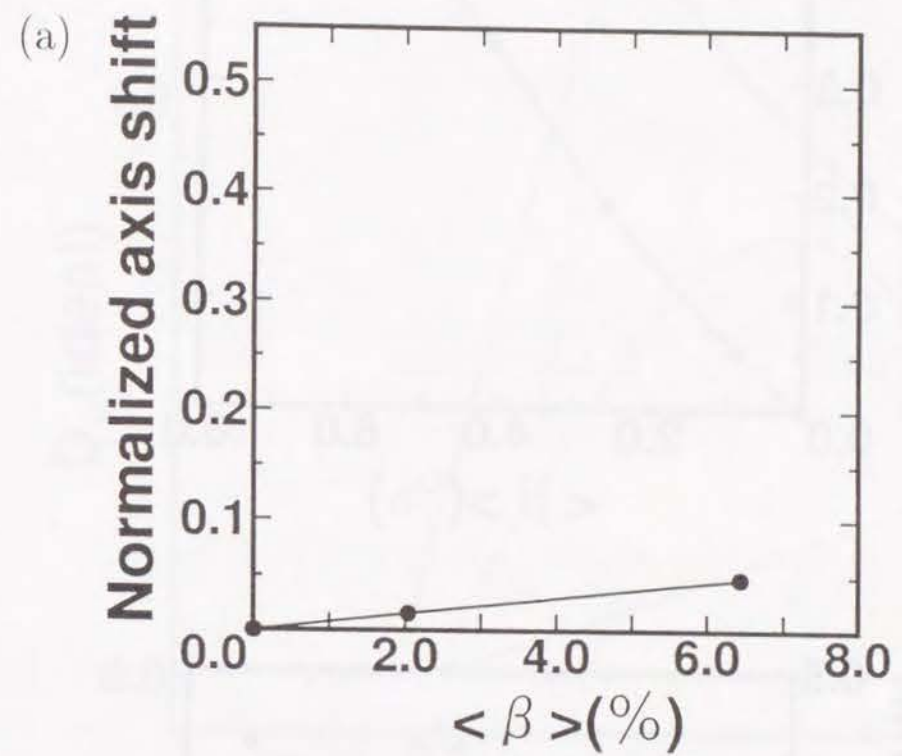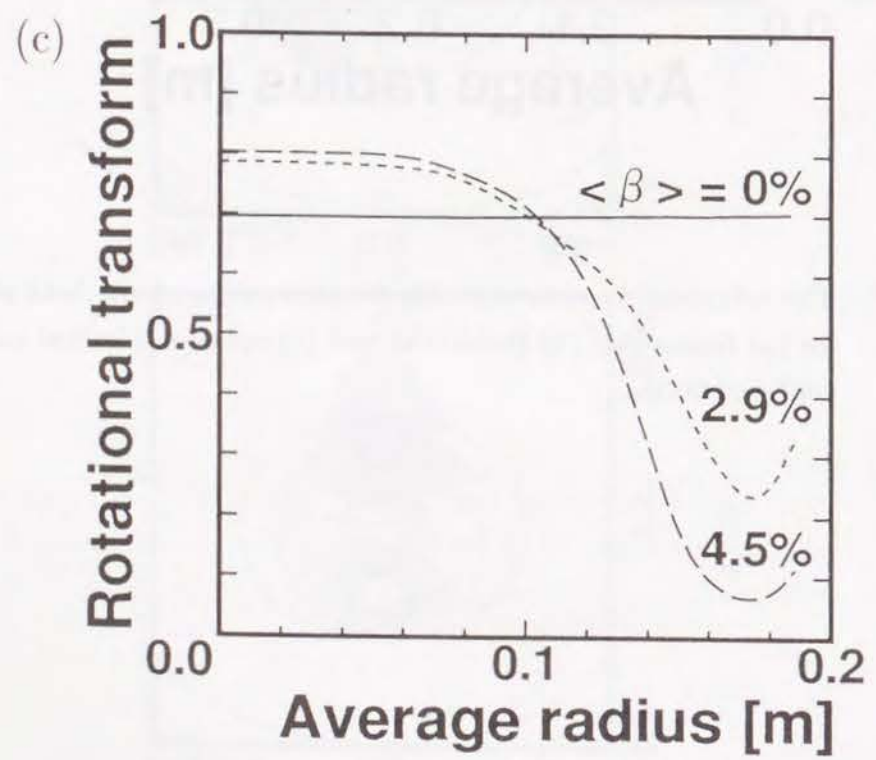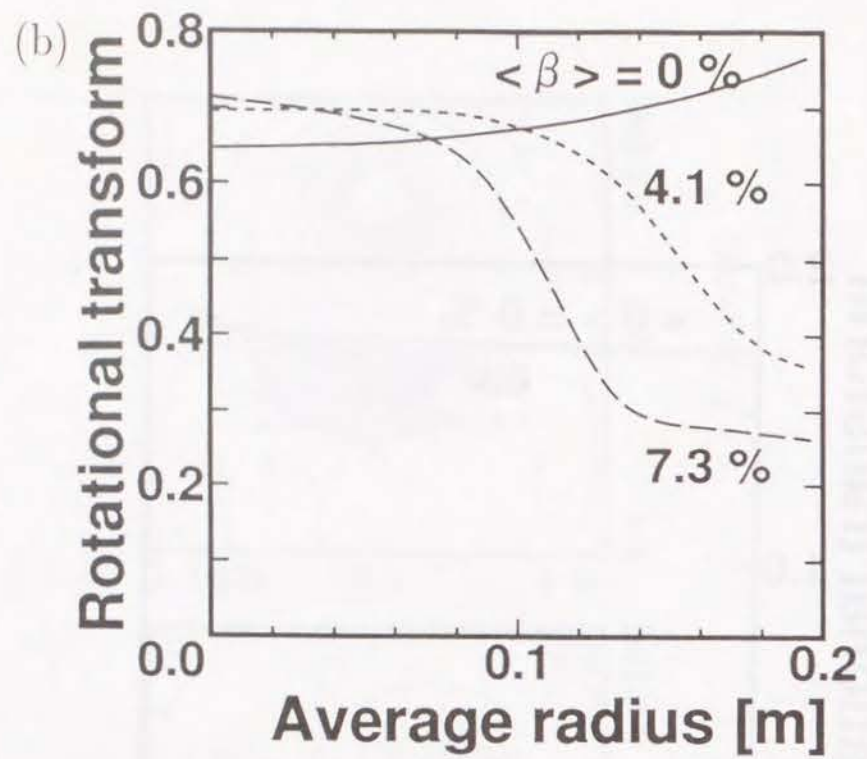
Fig. 3.8: Magnetic axis shift normalized by plasma minor radius versus $\langle \beta \rangle$ for (a) Helias-like, (b) Heliac-like and (c) optimized helical axis configurations.

(b)

(c)
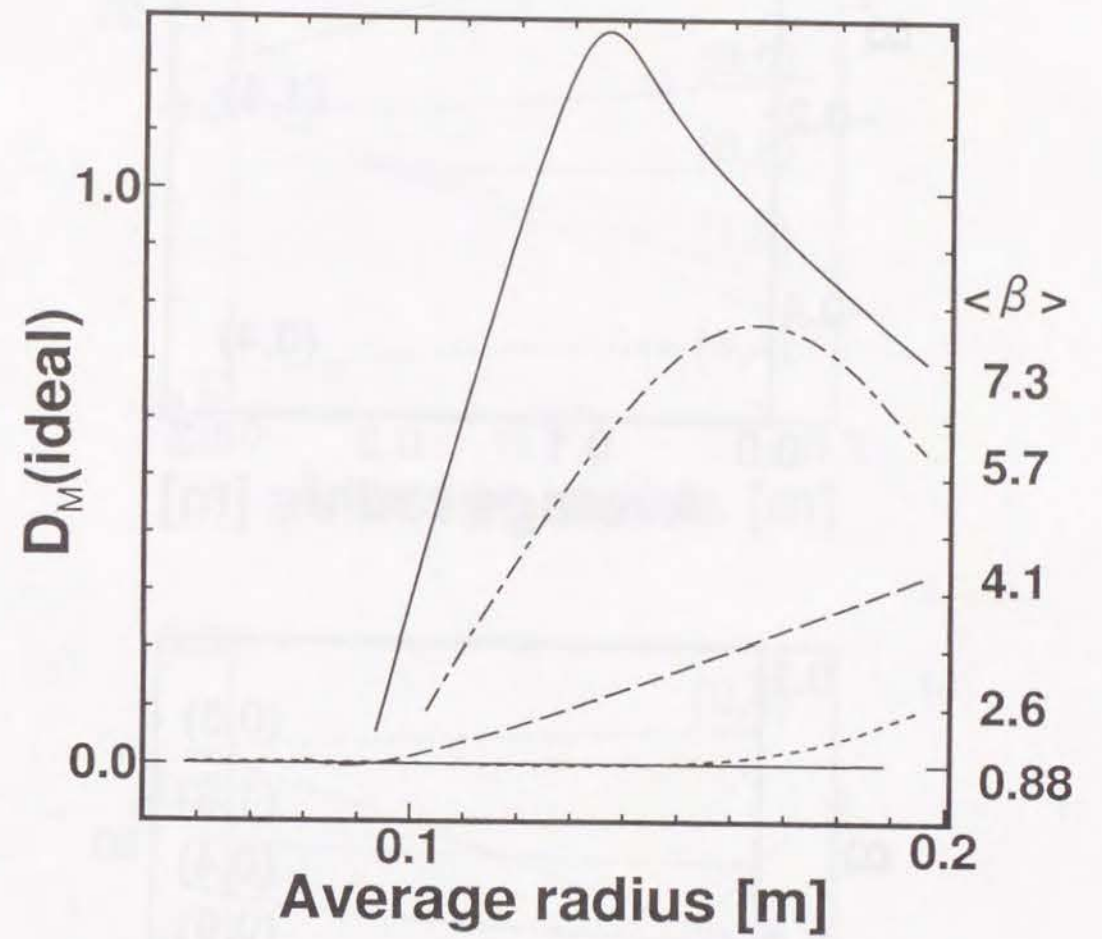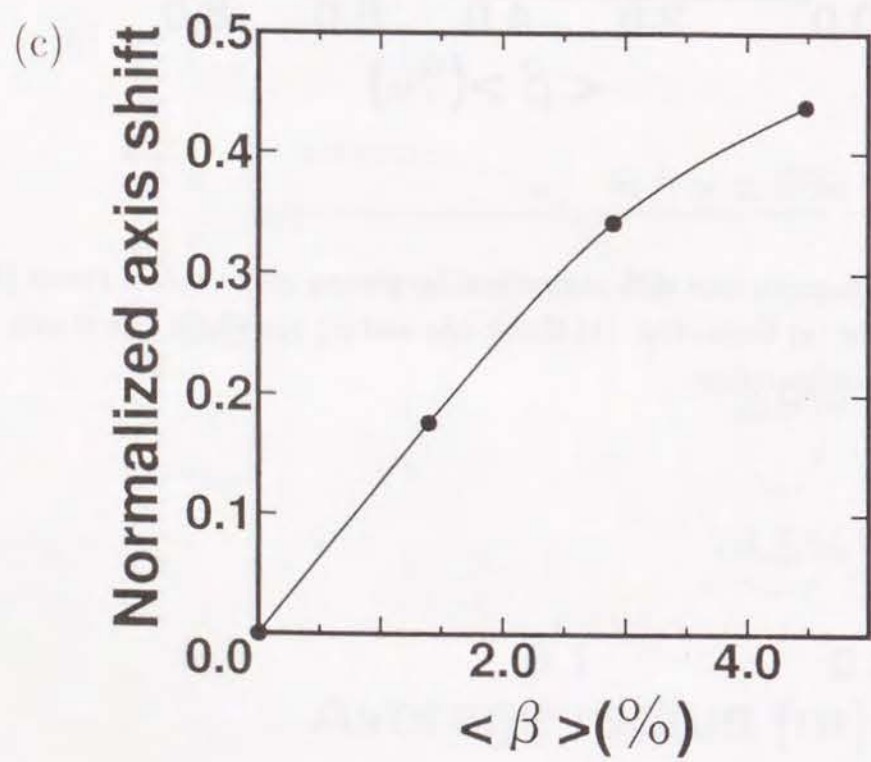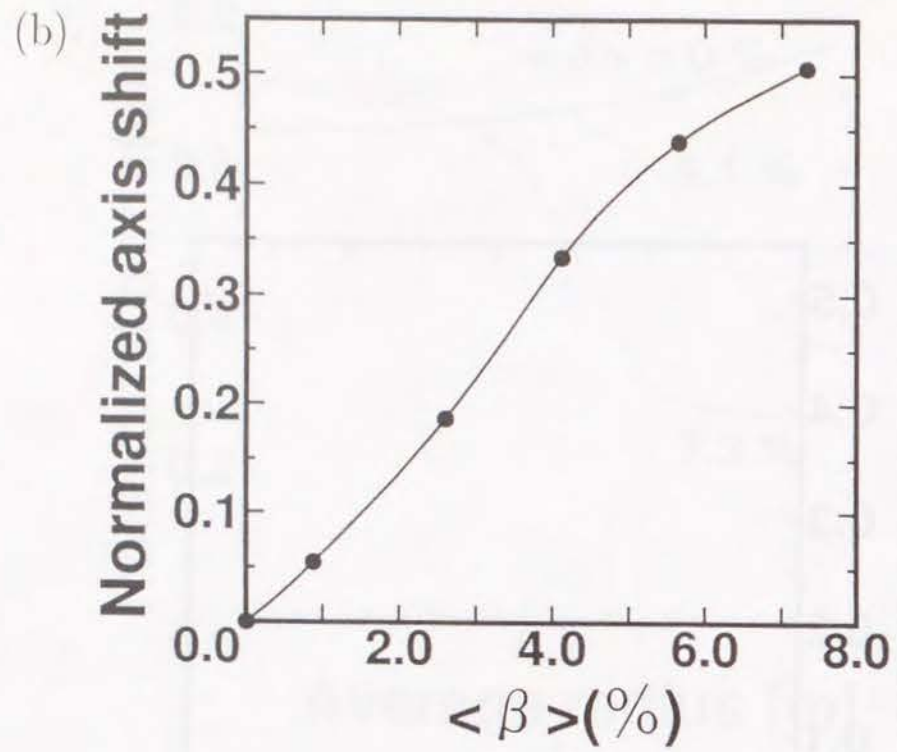
Fig. 3.9: The Mercier stability criterion D_M are shown for several $\langle \beta \rangle$ values for the Heliac-like configuration.
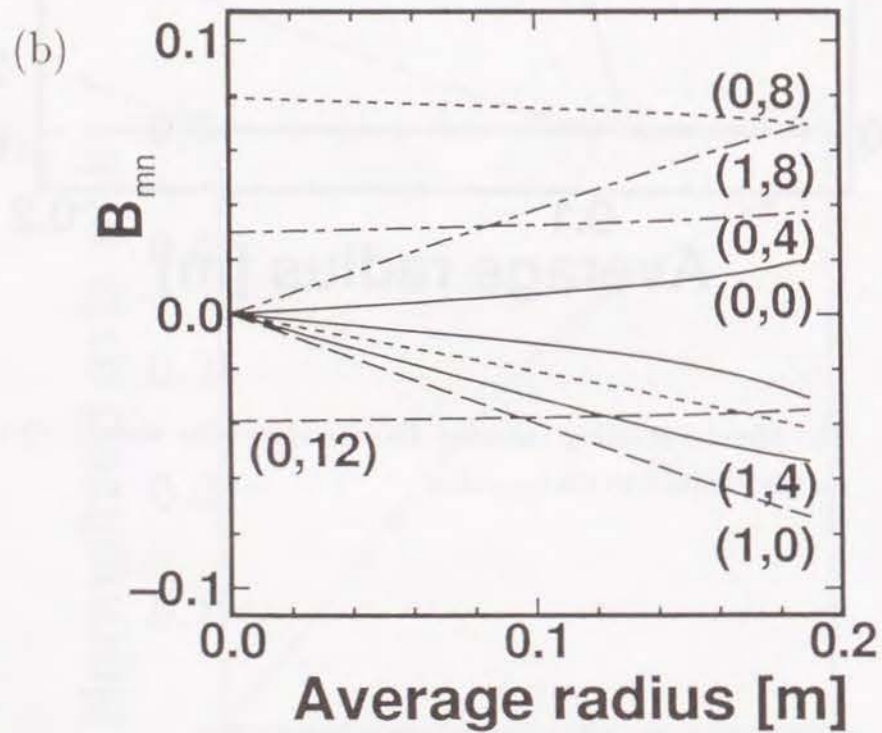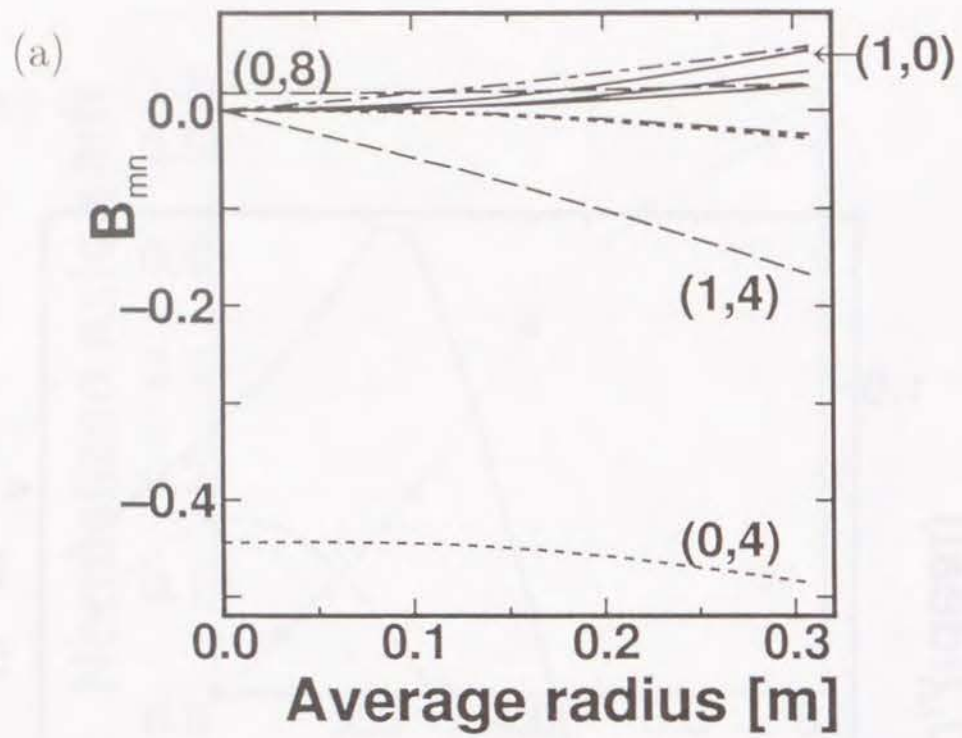
Fig. 3.10: Fourier spectrum of the magnetic field strength in the Boozer coordinates for (a) Helias-like and (b) Heliac-like configurations.
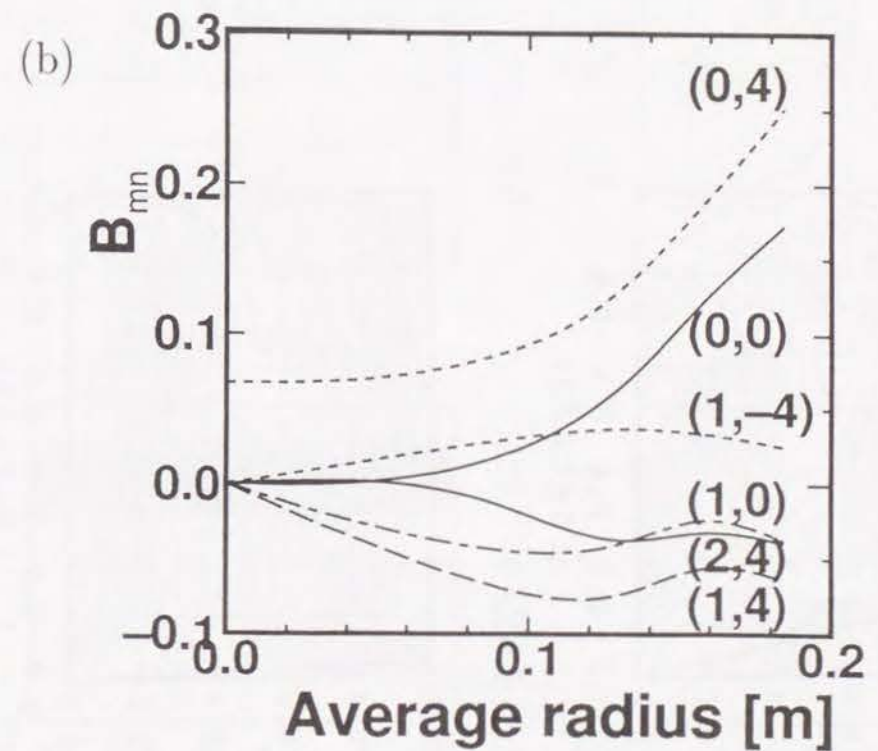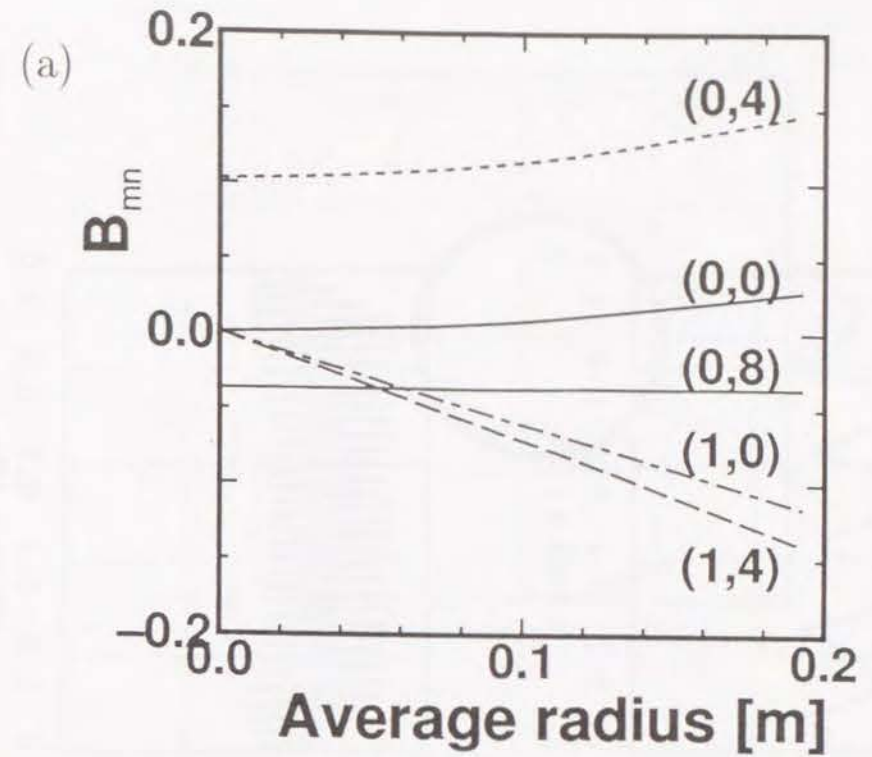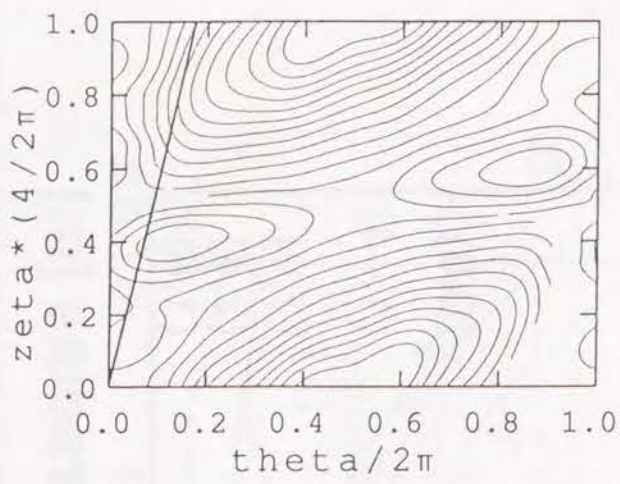

Fig. 3.11: Fourier spectrum of the magnetic field strength in the Boozer coordinates for (a) vacuum and (b) $\langle \beta \rangle = 4.5\%$ for optimized helical axis configuration.

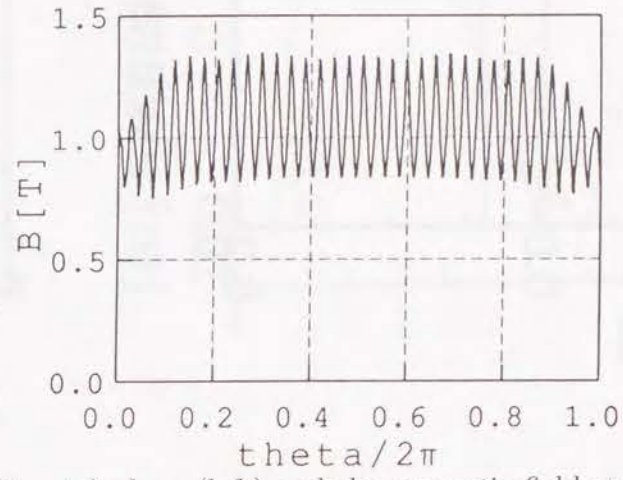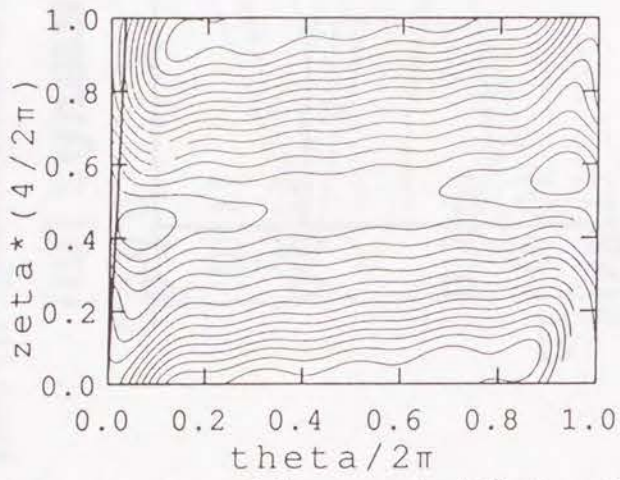(a) $\langle\beta\rangle = 0\%$
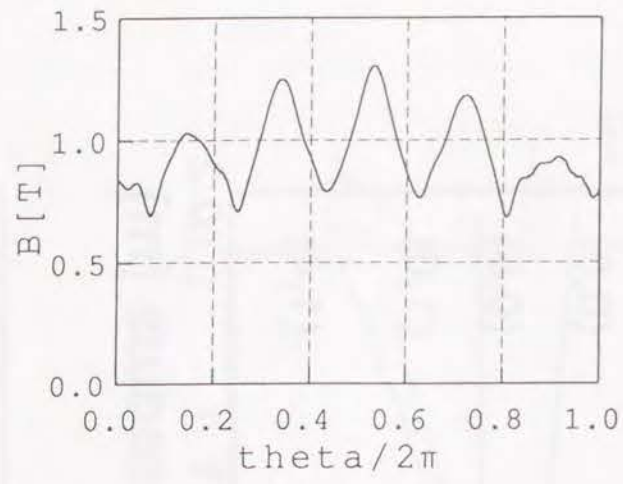
(b) $\langle\beta\rangle = 4.5\%$

Fig. 3.12: Contours of the magnetic field strength on the (θ_B, ϕ_B) plane (left) and the magnetic field strength along the field line (right) both on the outermost magnetic surface for (a) vacuum and (b) $\langle\beta\rangle = 4.5\%$ cases. The solid line in the left figures denotes the magnetic field line for one toroidal period.
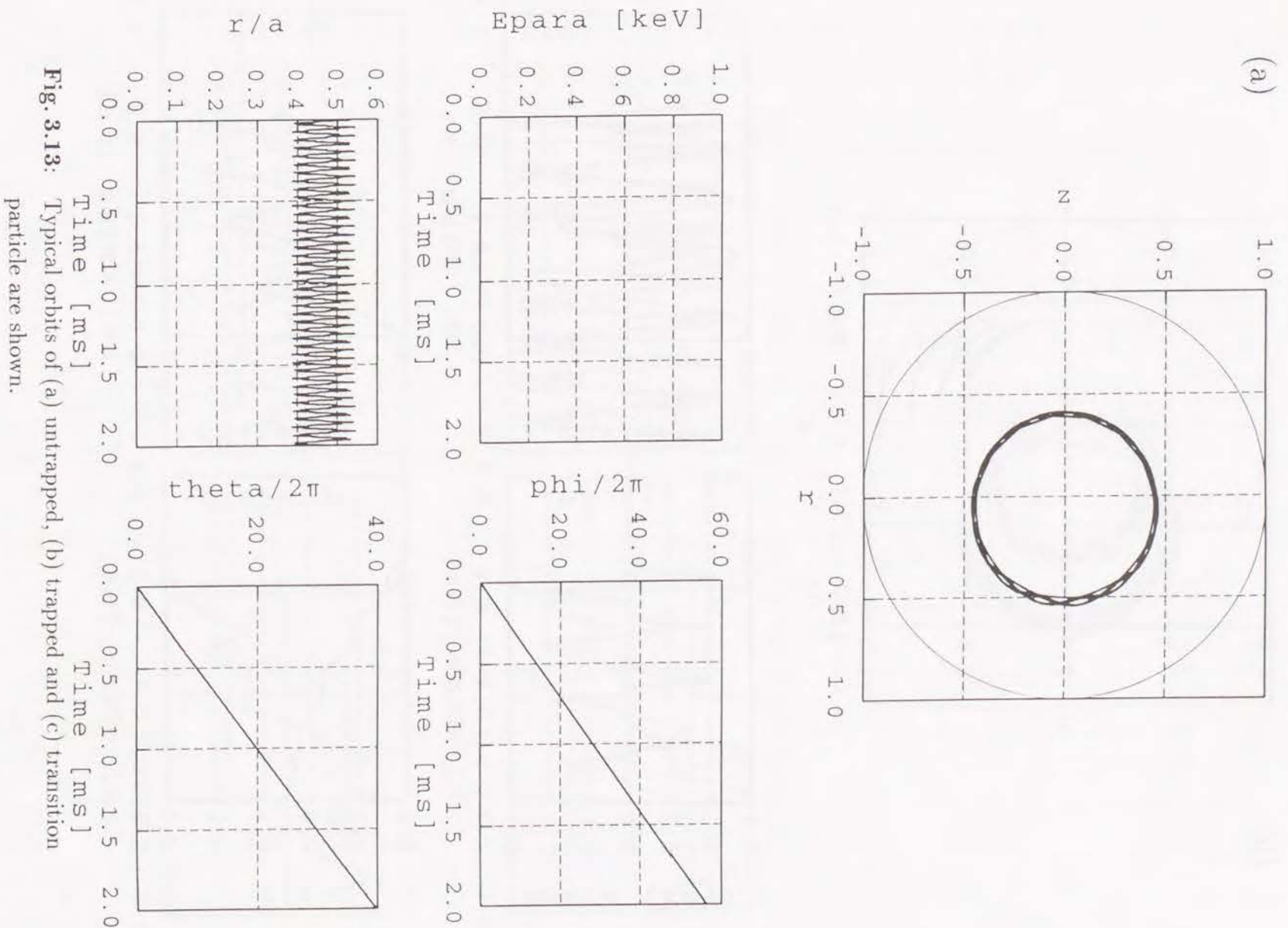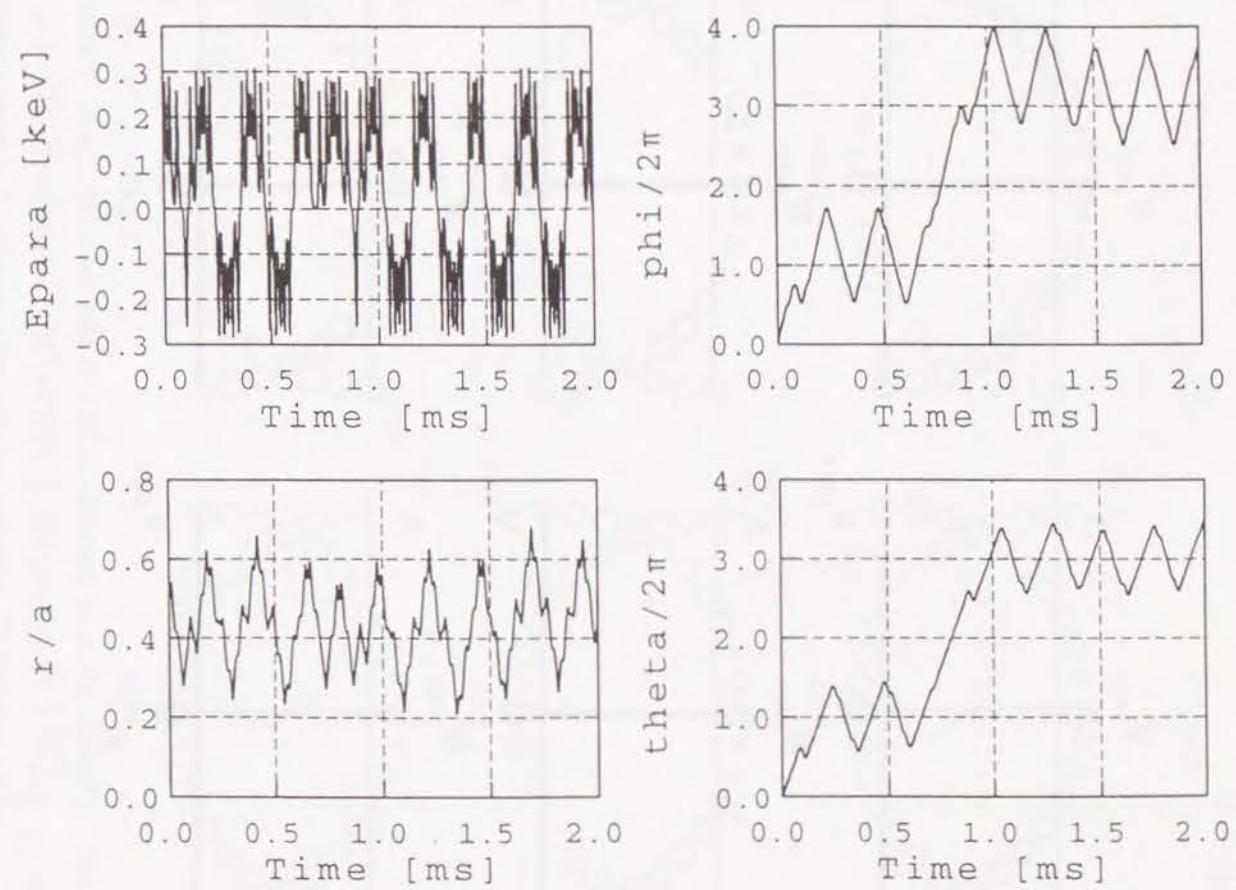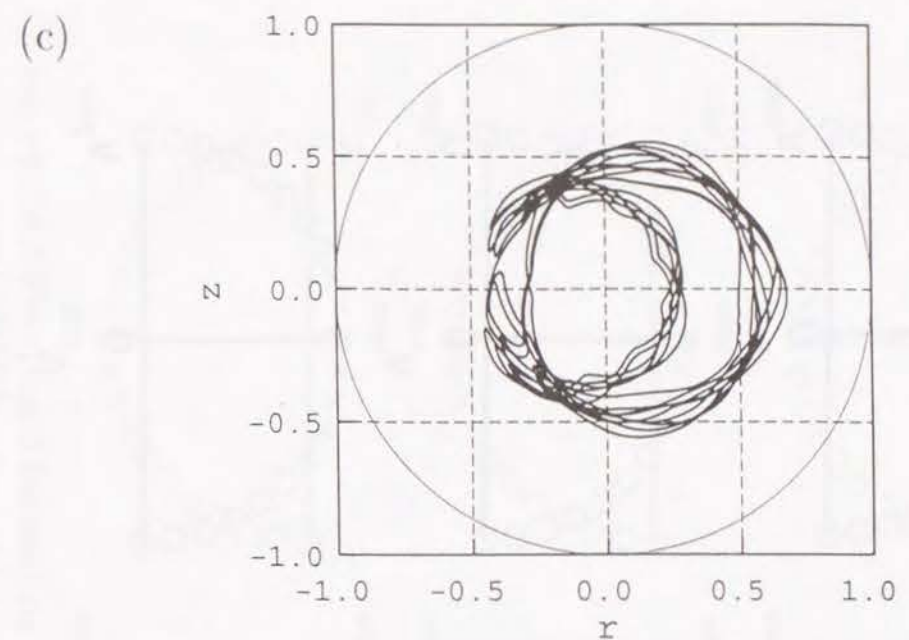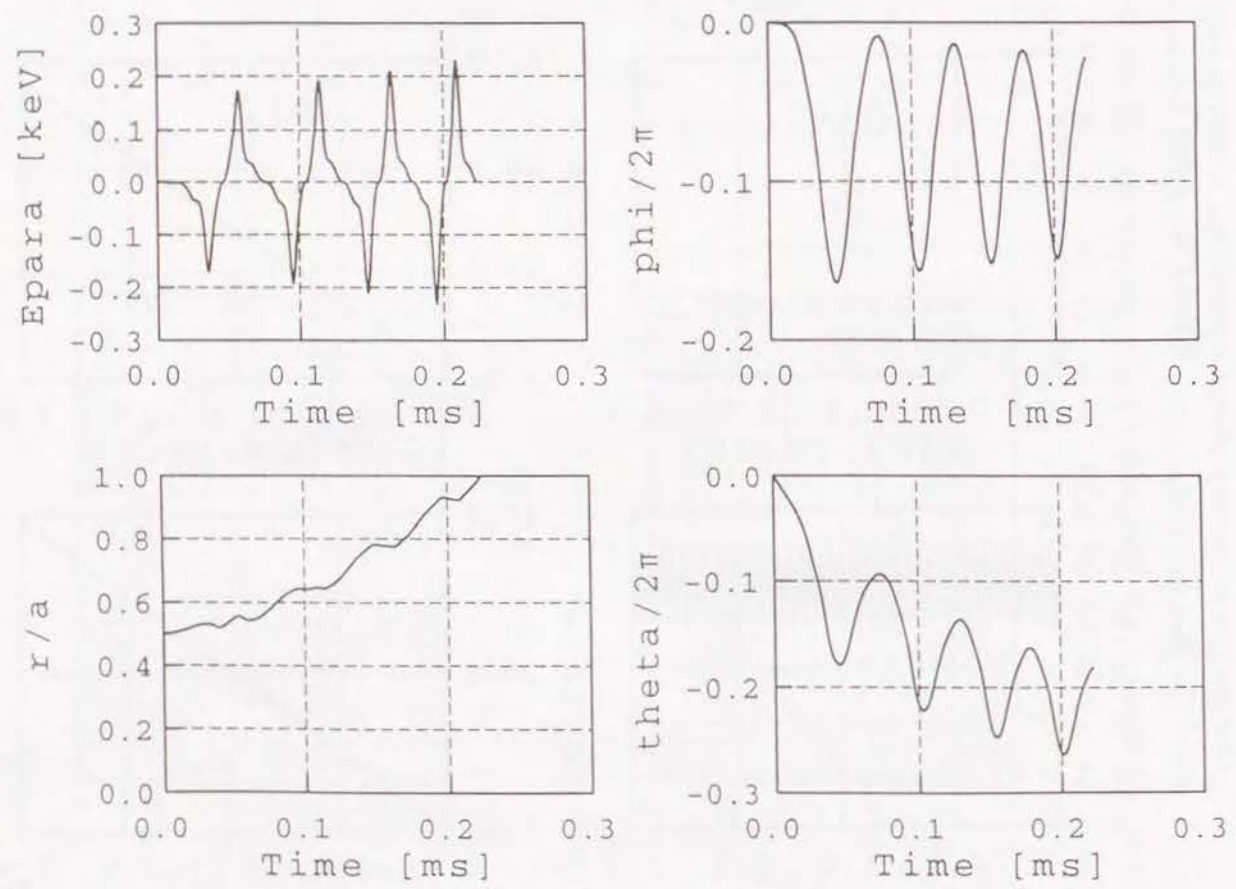

Fig. 3.13: Typical orbits of (a) untrapped, (b) trapped and (c) transition particle are shown.

(b)

(c)

(a) $\theta_{B0} = 0$

$\phi_{B0} = 0$ $(1/4)(2\pi/M)$ $(1/2)(2\pi/M)$

r/a

V_{perp} V_{perp} V_{perp}

0.2

0 V_{para} 0 V_{para} 0 V_{para}

V_{perp} V_{perp} V_{perp}

0.5

0 V_{para} 0 V_{para} 0 V_{para}

V_{perp} V_{perp} V_{perp}

0.8

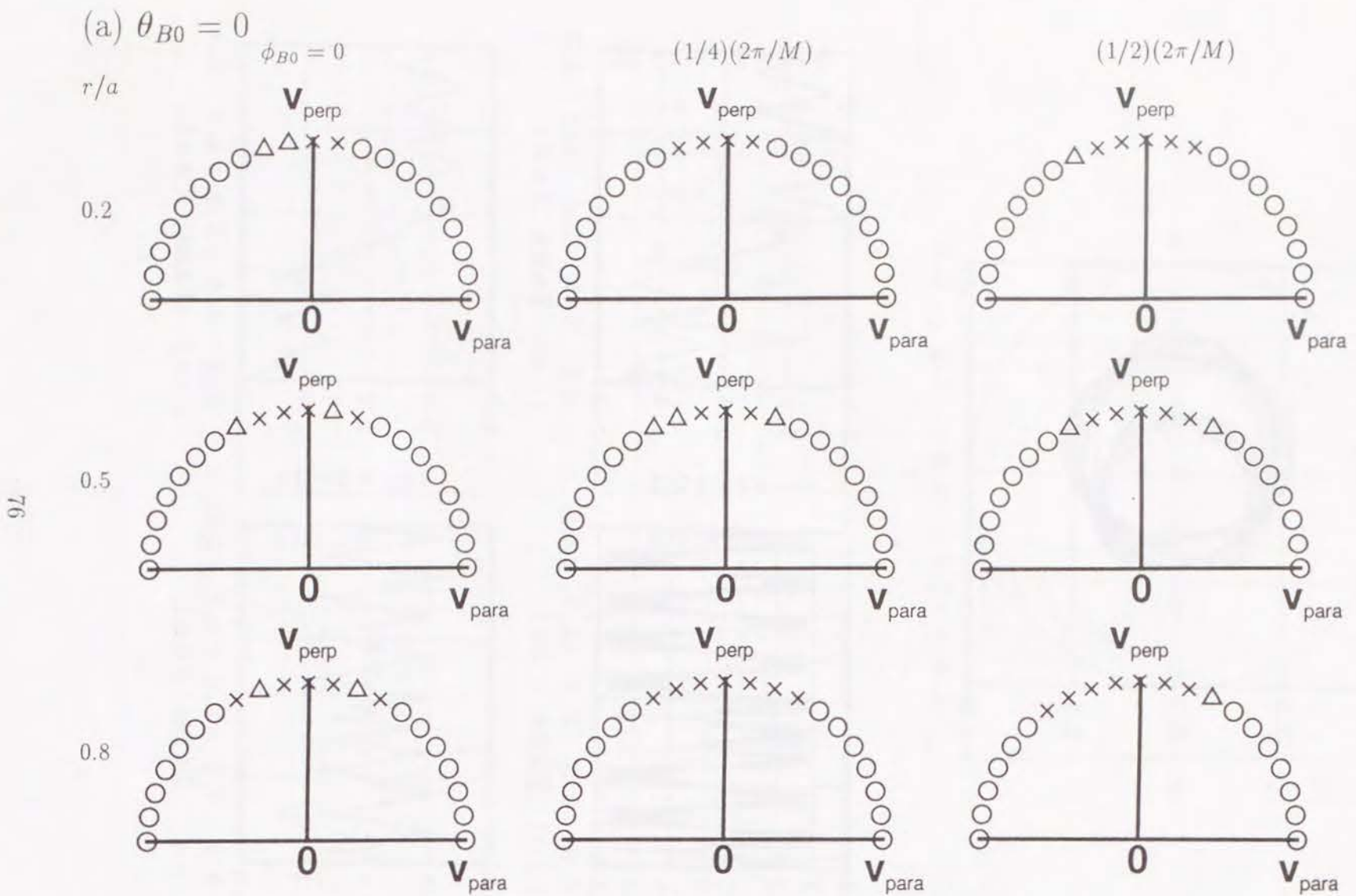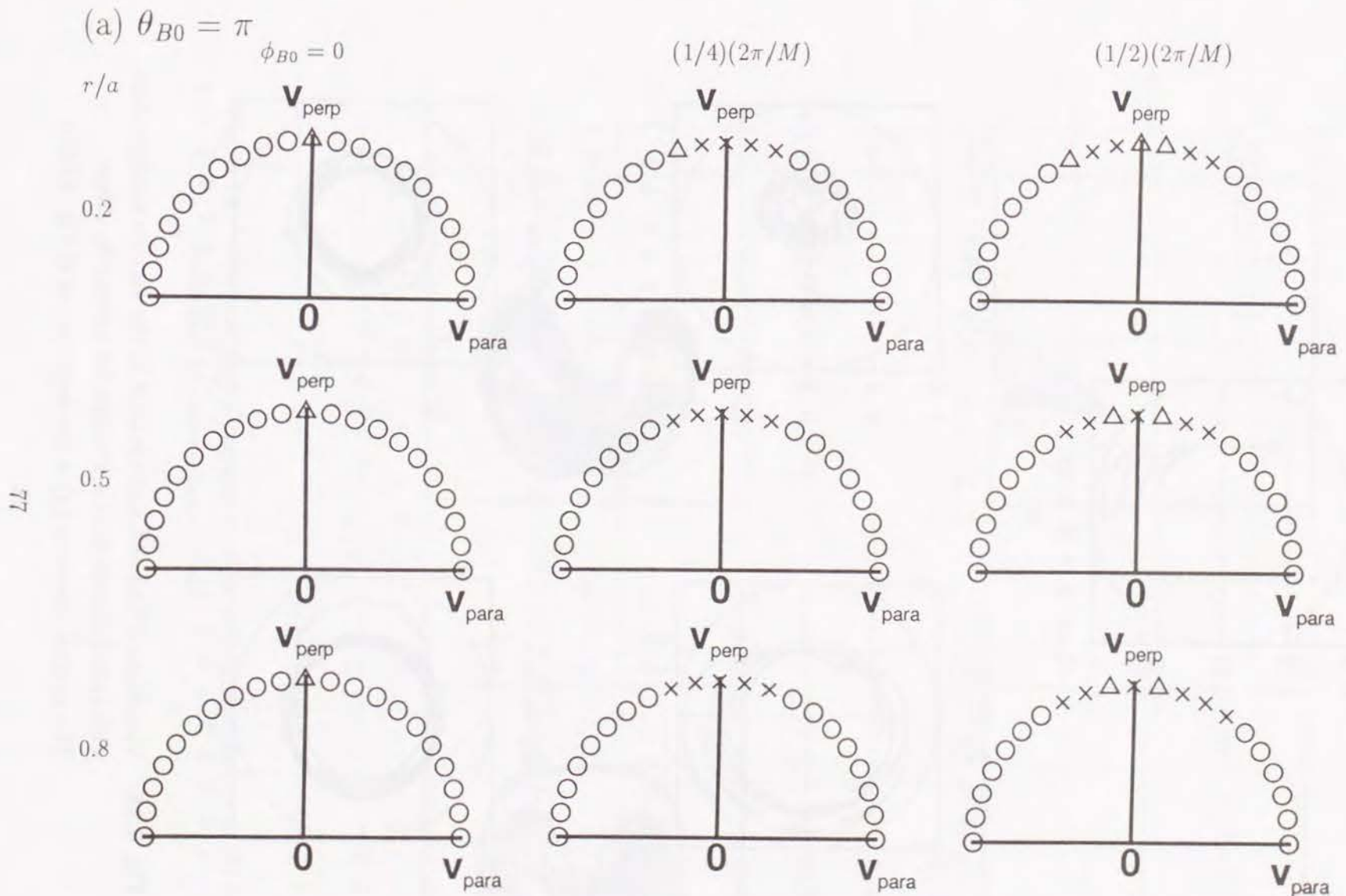0 V_{para} 0 V_{para} 0 V_{para}
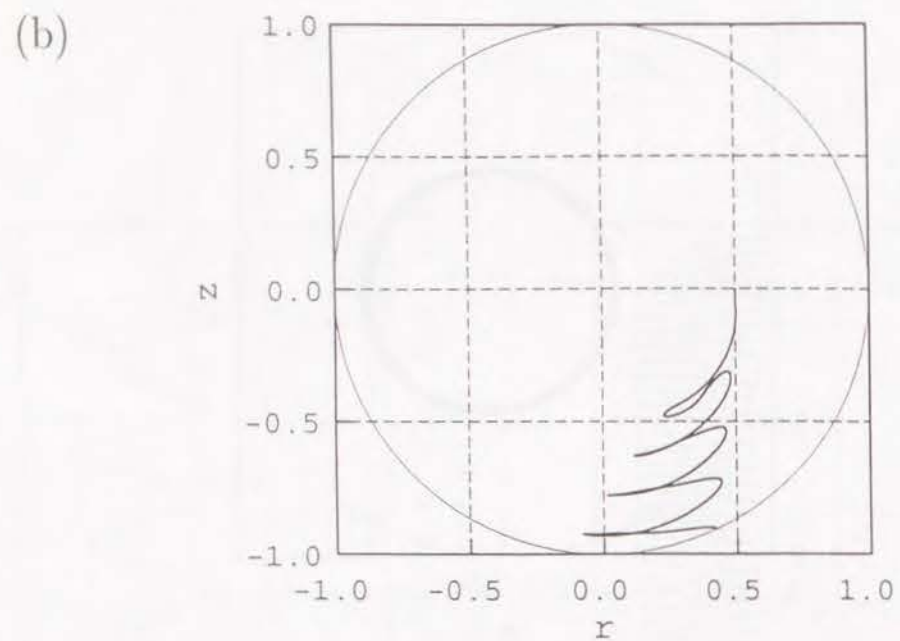
Fig. 3.14: Classification of particle orbits in the velocity space. Particles are launched from $r/a = 0.2$, 0.5, 0.8 and $\phi_{B0} = 0$, $(1/4)(2\pi/M)$, $(1/2)(2\pi/M)$, respectively, starting from (a) $\theta_{B0} = 0$ and (b) $\theta_{B0} = \pi$. The symbol $\bigcirc$ denotes untrapped particle, $\triangle$ denotes trapped particle and $\times$ denotes loss particle.

(a) $\theta_{B0} = \pi$

$\phi_{B0} = 0$ $(1/4)(2\pi/M)$ $(1/2)(2\pi/M)$

r/a

V_{perp} V_{perp} V_{perp}

0.2

0 V_{para} 0 V_{para} 0 V_{para}

V_{perp} V_{perp} V_{perp}

0.5

0 V_{para} 0 V_{para} 0 V_{para}

V_{perp} V_{perp} V_{perp}

0.8

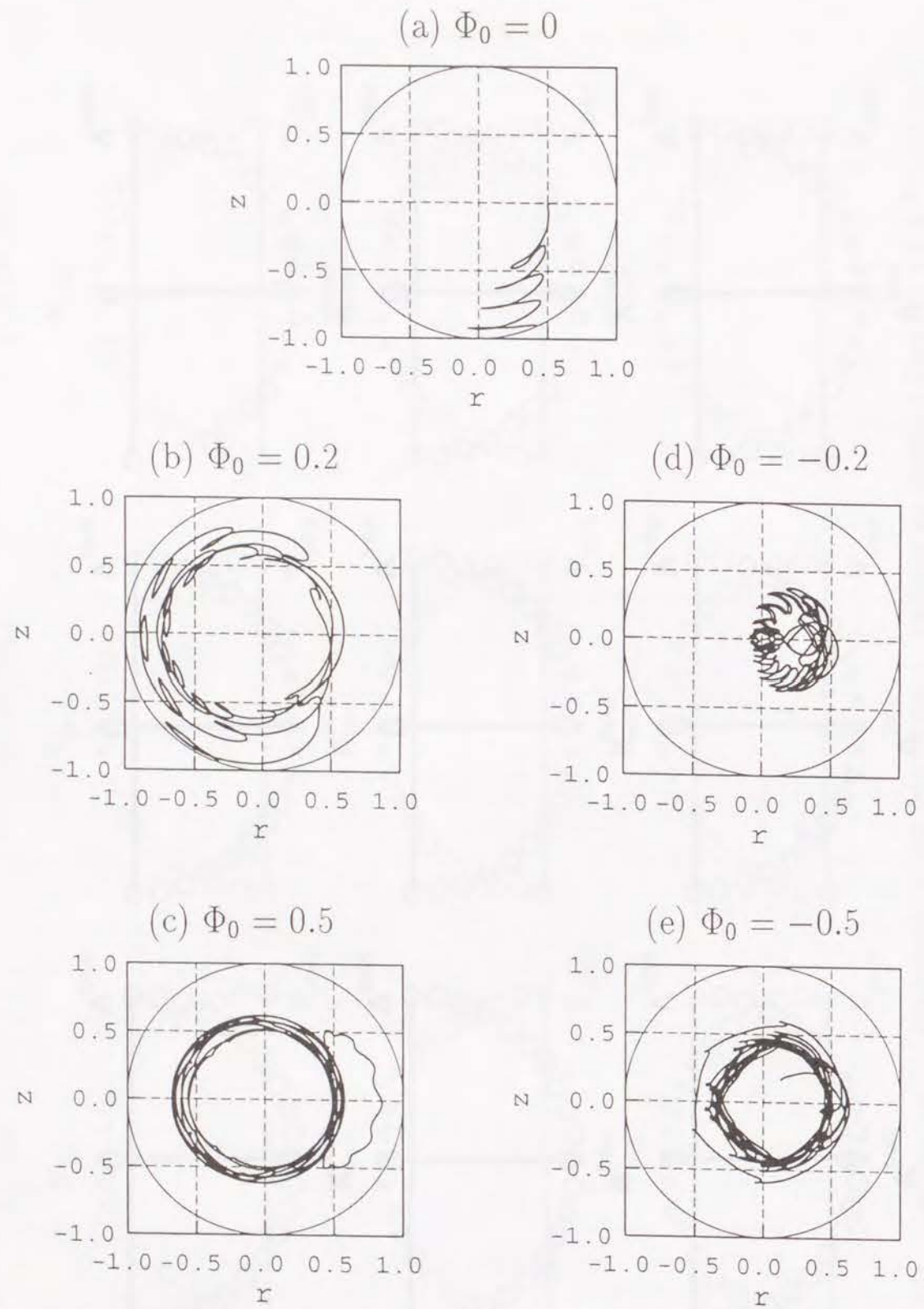0 V_{para} 0 V_{para} 0 V_{para}

Fig. 3.15: Variations of trapped particle orbit in the vacuum configuration with radial electric field are shown for several Φ_0 values. The particle shown in (a) is the same one as in Fig. 3.13(b).
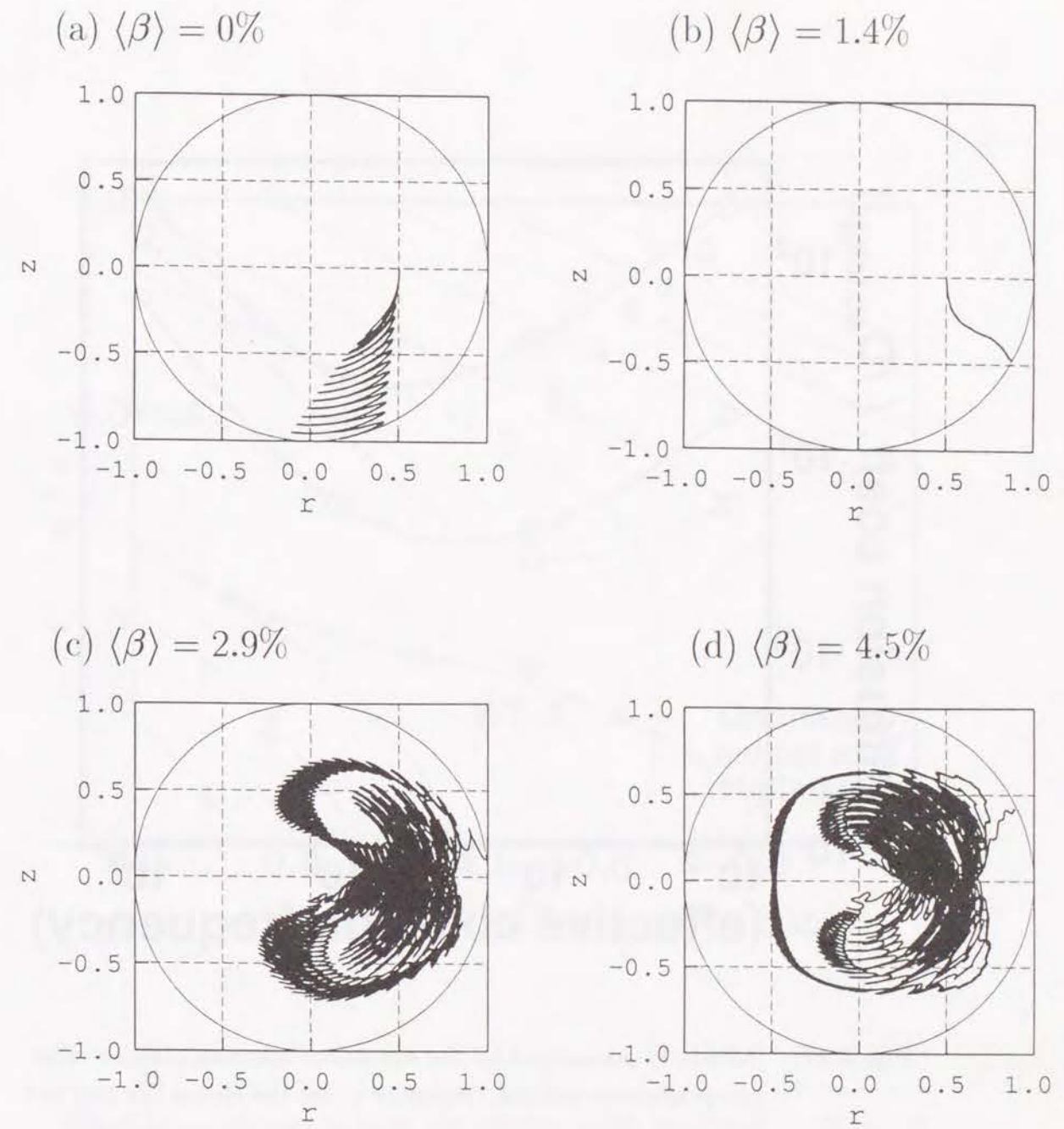

Fig. 3.16: Orbits of deeply trapped particle with kinetic energy of 0.1 keV are shown for several beta values.
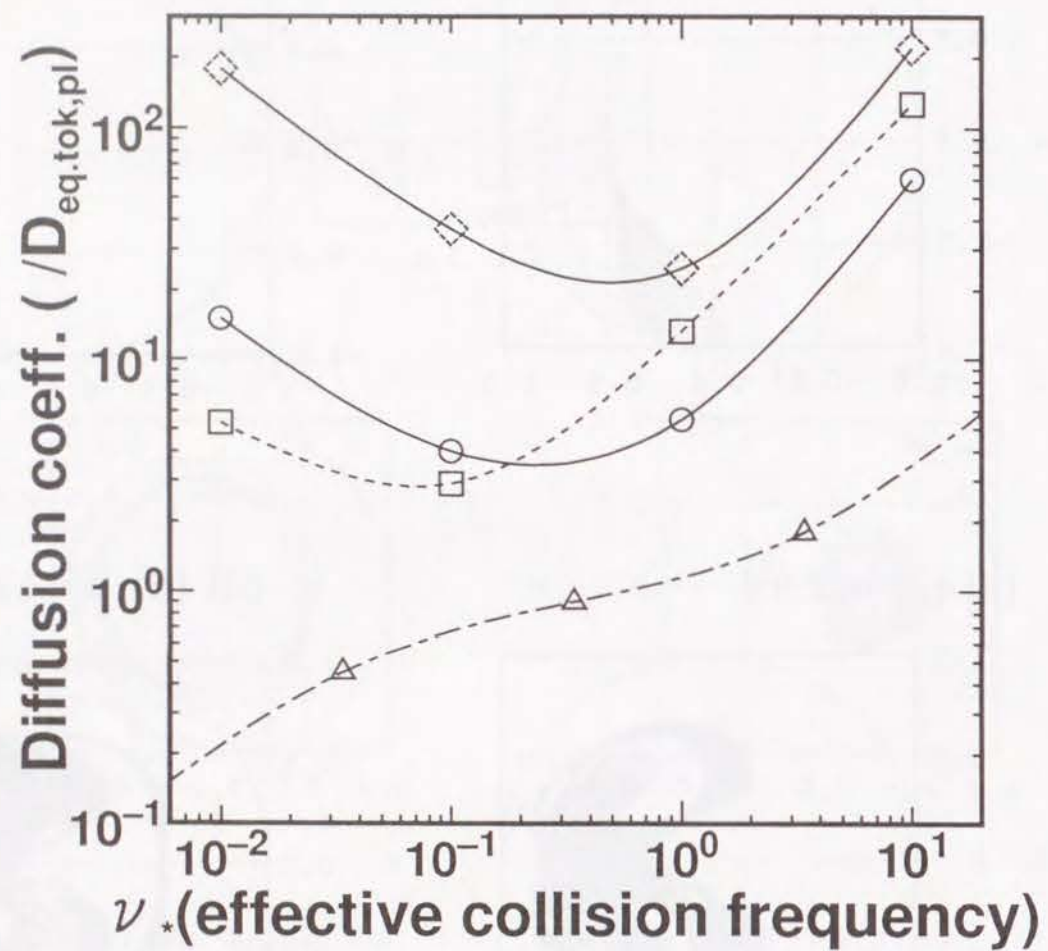
Fig. 3.17: Diffusivity normalized by the equivalent tokamak plateau value versus effective collision frequency ν_* for the Helias-like ($\diamond$) and Heliac-like ($\square$) configurations. For comparison, results for the W7-X ($\triangle$) [14] and the TJ-II ($\bigcirc$) [87] are also shown.
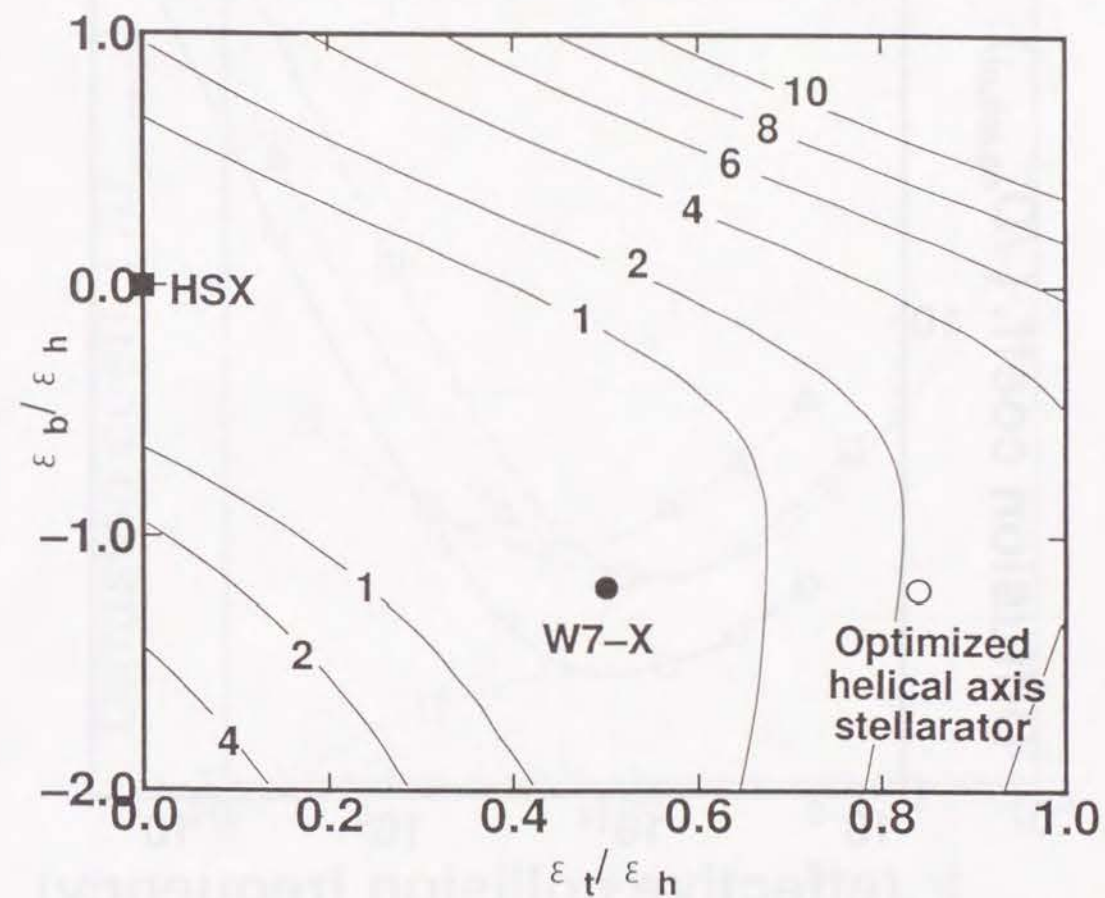

Fig. 3.18: Contours given by the integral in the bracket of Eq. (2.11) are shown on (ϵ_t/ϵ_h, ϵ_b/ϵ_h) plane. The optimized helical axis configuration is plotted ($\bigcirc$). The origin corresponds to the quasi-helically symmetric stellarator such as the HSX. For reference, the case of the W7-X is also plotted ($\bullet$).

Fig. 3.19: Diffusivity normalized by the equivalent tokamak plateau value versus effective collision frequency ν_* for the optimized helical axis configuration (○) with negligibly small radial electric field. For comparison, results for zero B_{04} case (△) and Heliac-like case (□) are also shown.
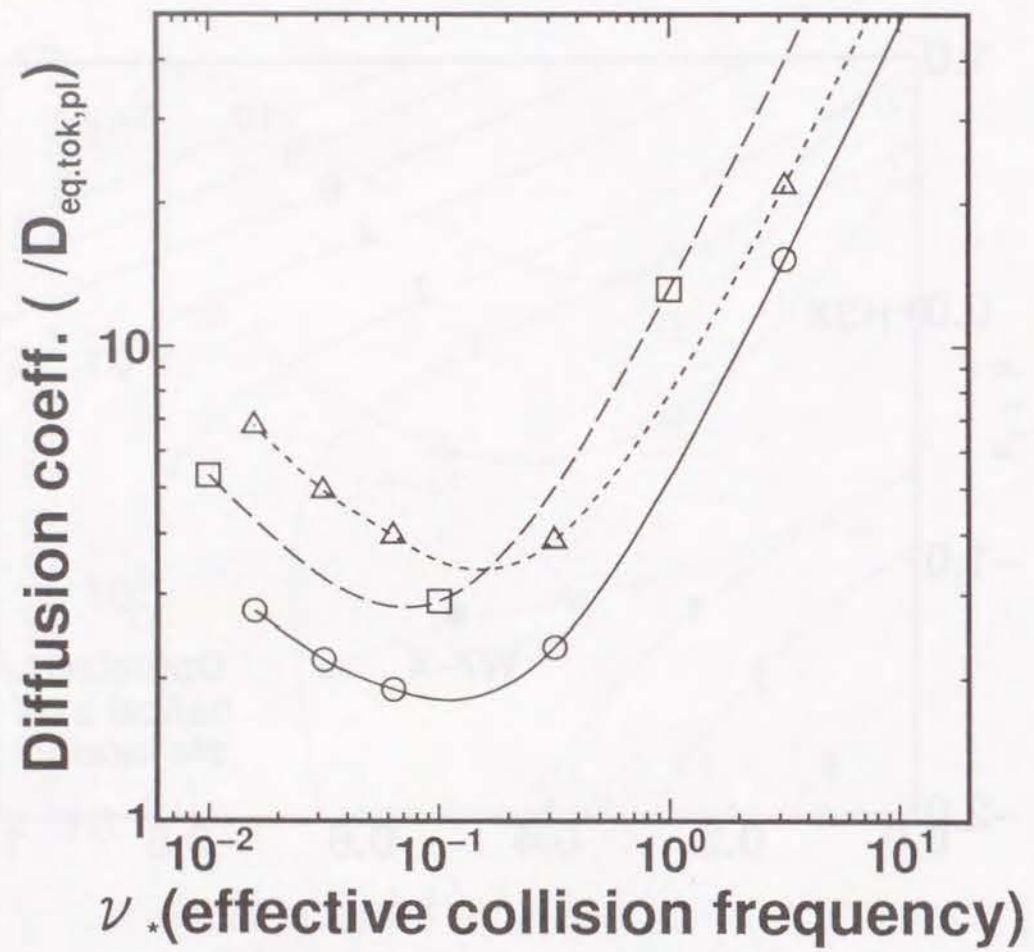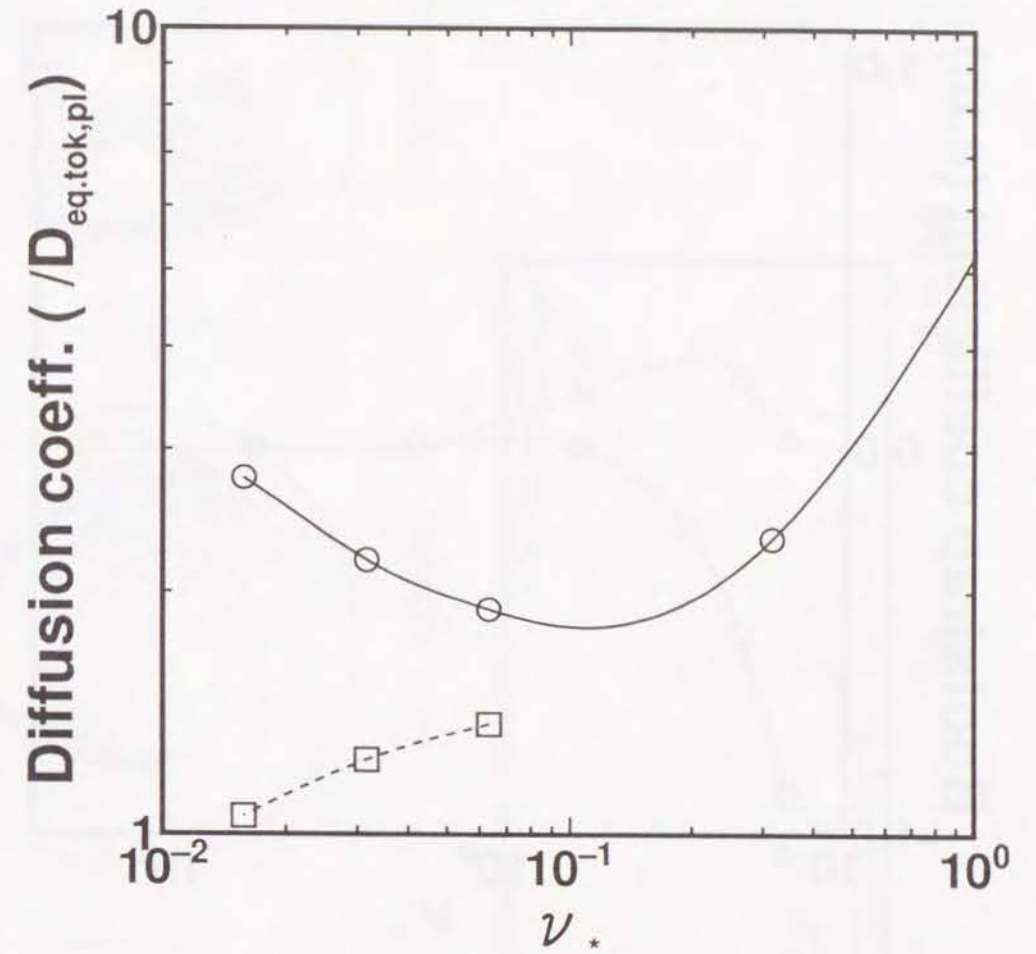

Fig. 3.20: Diffusivity normalized by the equivalent tokamak plateau value versus effective collision frequency ν_* for the optimized helical axis configuration (□) with radial electric field of $E_r/v = 3 \times 10^{-3}$ V·s/m². For comparison, results for negligibly small E_r case (○) are also shown.

Bootstrap coefficient (a.u.)
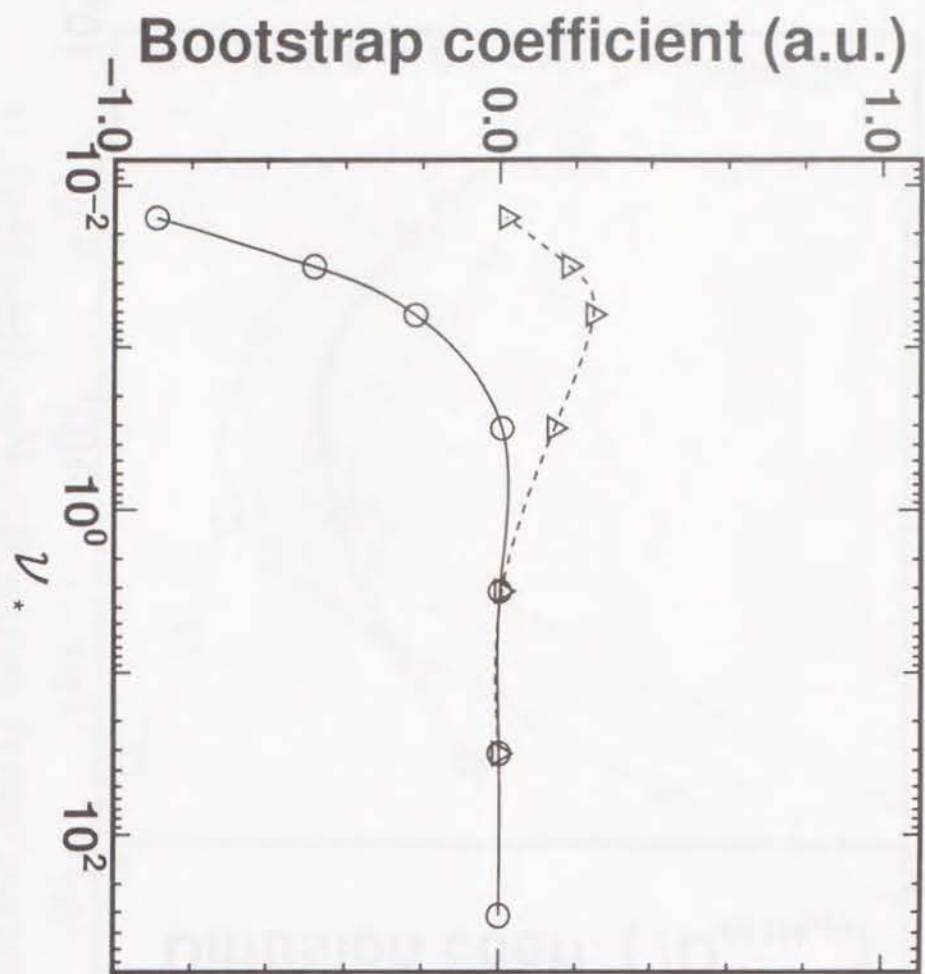
Fig. 3.21: Bootstrap coefficient (a.u.) versus effective collision frequency ν_* for the optimized helical axis configuration ($\bigcirc$). For comparison, results for zero B_{04} case ($\triangle$) is also shown.

(a)

$\phi = 0$ $\phi = (1/4)(2\pi/M)$ $\phi = (1/2)(2\pi/M)$

(b) 2π

θ

0

0 ϕ $2\pi/M$

Fig. 3.22: Poincaré plots of magnetic field lines outside the outermost magnetic surface in Helias-like configuration: (a) traces in $\phi = 0$, $(1/4)(2\pi/M)$ and $(1/2)(2\pi/M)$ and (b) traces on the vacuum chamber.

(a)

$\phi = 0$ $\phi = (1/4)(2\pi/M)$ $\phi = (1/2)(2\pi/M)$

(b) 2π

θ

0

0 ϕ $2\pi/M$

Fig. 3.23: Poincaré plots of magnetic field lines outside the outermost magnetic surface in Heliac-like configuration: (a) traces in $\phi = 0$, $(1/4)(2\pi/M)$ and $(1/2)(2\pi/M)$ and (b) traces on the vacuum chamber.

(a)

$\phi = 0$ $\phi = (1/4)(2\pi/M)$ $\phi = (1/2)(2\pi/M)$

(b) 2π

θ

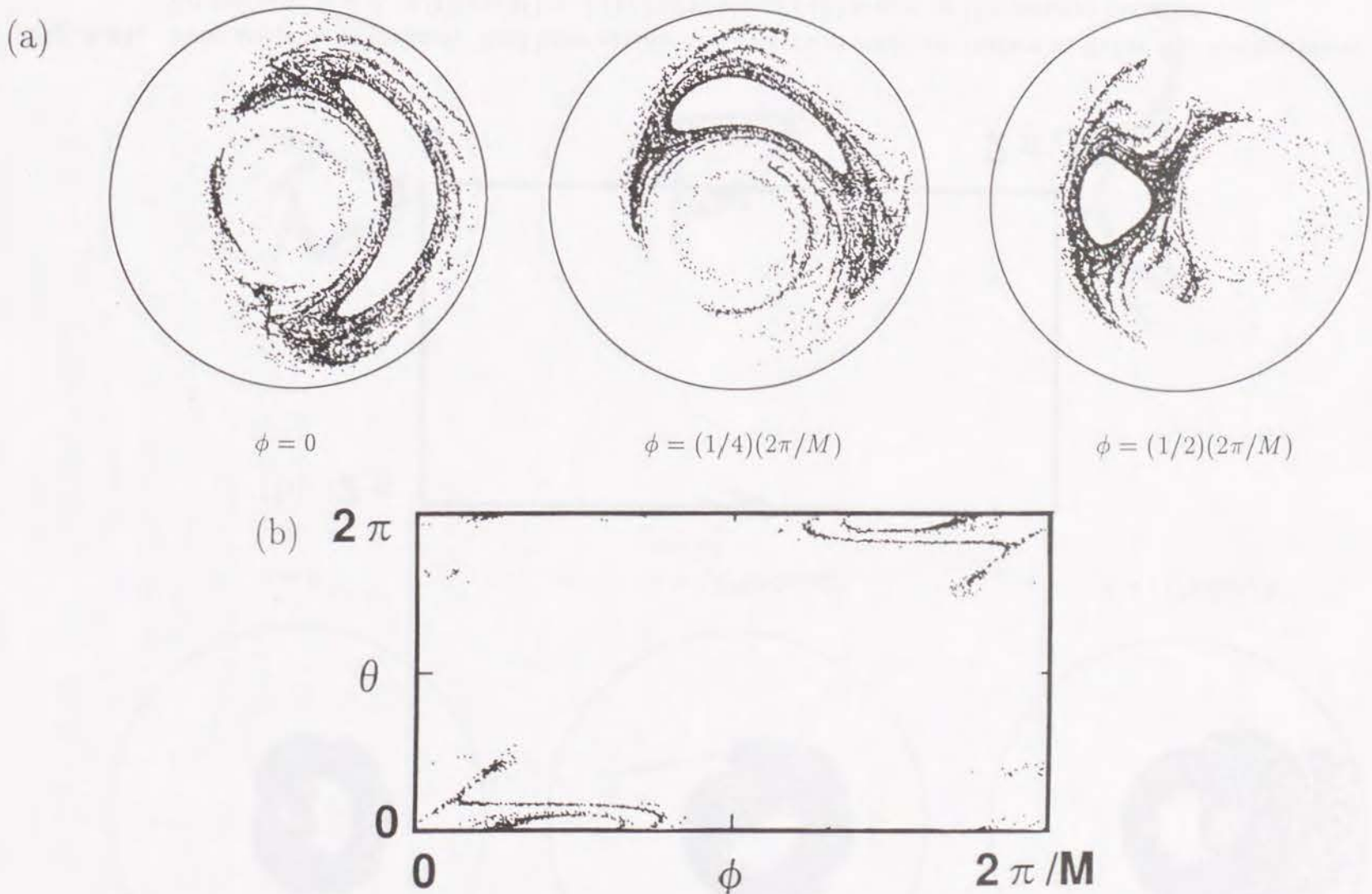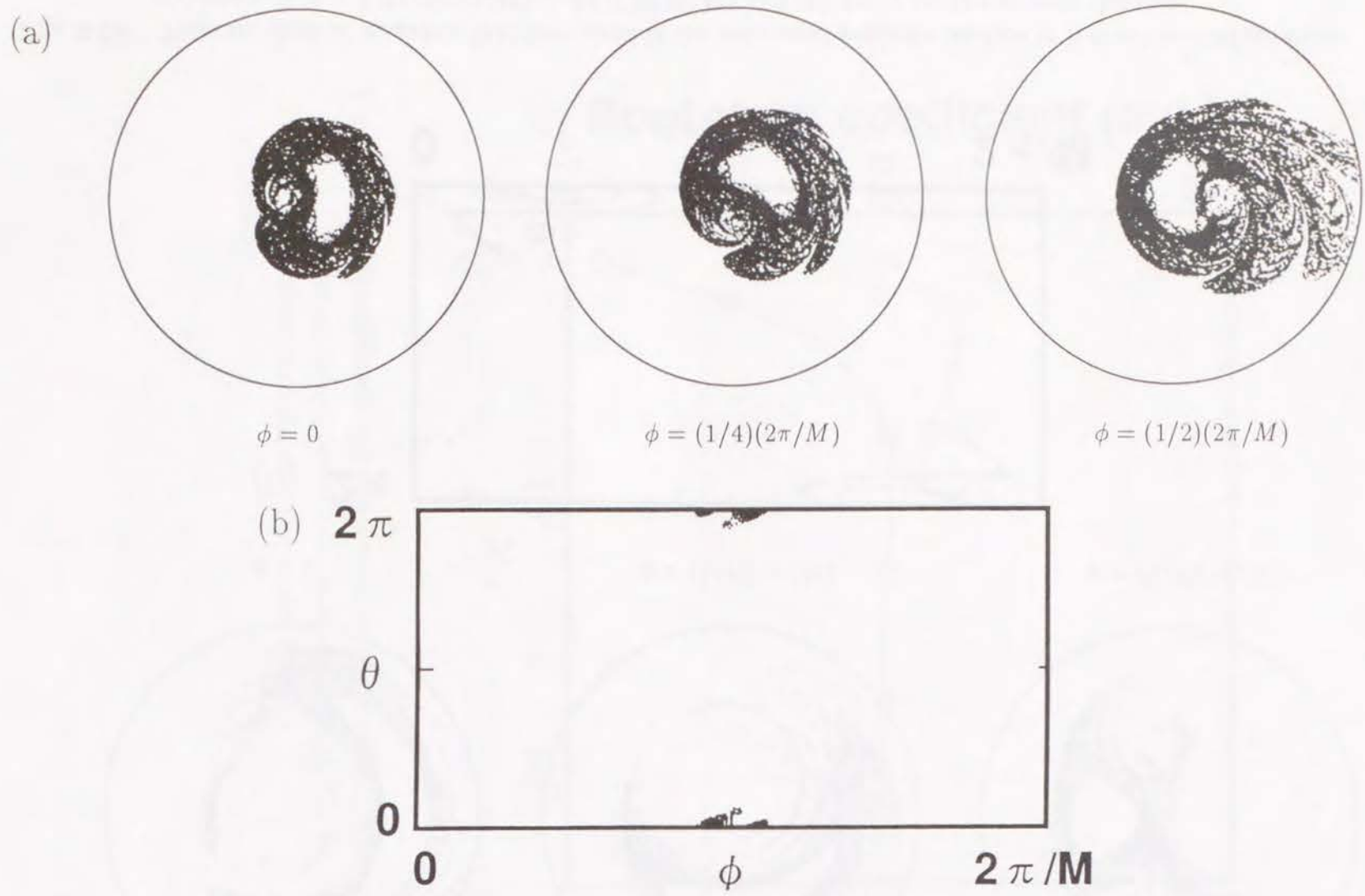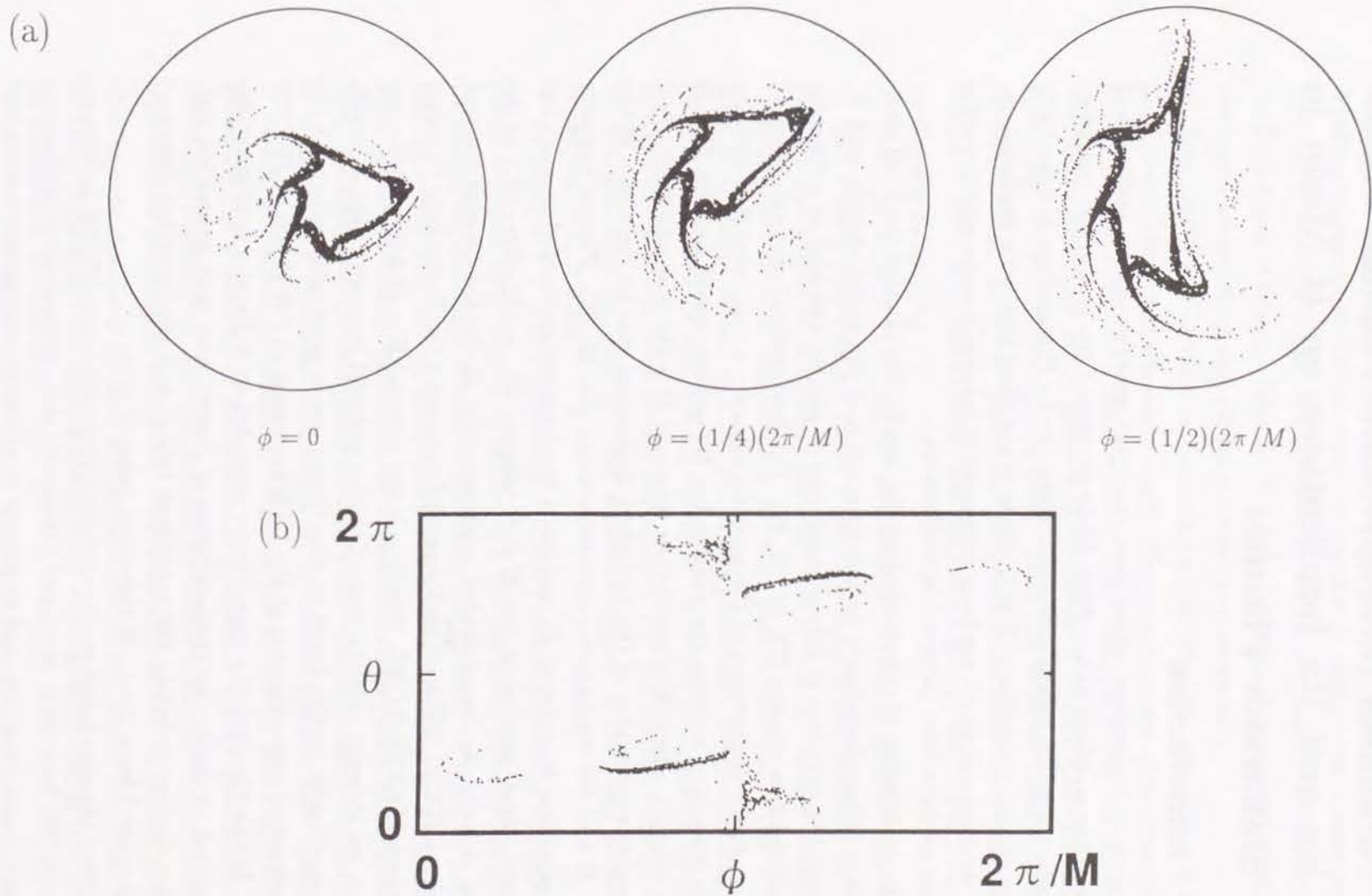0

0 ϕ $2\pi/M$

Fig. 3.24: Poincaré plots of magnetic field lines outside the outermost magnetic surface in optimized helical axis configuration: (a) traces in $\phi = 0$, $(1/4)(2\pi/M)$ and $(1/2)(2\pi/M)$ and (b) traces on the vacuum chamber.

4 Nonlinear Incompressible Poloidal Viscosity and Its Implications on H Mode in Stellarator Plasmas

4.1 Introduction

For present stellarators, anomalous transport governs plasma confinement rather than neoclassical one does. However, even if the anomalous transport is dominant in the helical axis stellarators, the L - H transition is expectable under certain conditions. The H mode is the discharge with improved energy confinement which has been developed in tokamaks and recently similar discharges have been observed in stellarators.

An explanation of the physical mechanism for the cause of the L - H transition in tokamaks is based on the bifurcation of the radial electric field E_r through the existence of a local maximum of plasma viscosity as a function of poloidal flow velocity [23, 24, 25, 26]. The fundamental physical reason of the nonlinear dependence of the poloidal viscosity on poloidal flow velocity is the resonance between the parallel (to B) particle speed and the $E \times B$ drift velocity, where E is the electric field and B is the magnetic field. Subsequently suppression of the turbulent fluctuation due to the shear of the $E \times B$ and the diamagnetic angular velocity [94, 95, 96]. Plasma viscosity is a nonlinear function of E_r and has a local maximum located at a critical poloidal Mach number of the $E \times B$ velocity $M_p = (V_{pE} B / v_{Ti} B_p)$ of the order of unity, as demonstrated experimentally in the Continuous Current Tokamak (CCT) [25] and the Tokamak Experiment for Technology Oriented Research (TEXTOR) [26]. Here V_{pE} is the poloidal $E \times B$ drift velocity, v_{Ti} is the ion thermal velocity, and B_p is the poloidal magnetic field strength. The qualitative results based on this theory are in good agreement with the experimental measurements at the L - H transition in DIII-D [23] or JFT-2M [24]. In this Chapter, the same theory extended to stellarator configurations is applied to clarify the characteristics of present and next generation stellarator devices including the optimized helical axis configuration discussed in Chapter 3 from the L - H transition point of view.

Other theories based on the turbulent Reynolds stress [97, 98] or Stringer spin-up [99] have been developed. However, their extensions to stellarators are not shown explicitly, and at present quantitative comparison among several devices is difficult. Since there are differences in magnetic configuration between tokamaks and stellarators, stellarator H mode experiments are important to develop the L - H transition theory, if the mechanism is the same for both types of device. Thus the present transition theory provides further tests with the existing and future stellarator experiments.

Since stellarator devices can sustain toroidal plasmas continuously without current drive and eliminate major disruptions easily, they have potentiality for the magnetic fusion reactor. The stellarator devices have been studied in Japan for many years, and Heliotron E [7] and CHS [8] are now operating. New next generation device LHD [13] is under construction. It is notable that the L - H transition like phenomena have been observed in the CHS, when the plasma current is induced to change rotational transform profile somewhat [22].

Stellarators with the name of Wendelstein have been studied intensively in Max-Planck Institute for many years. Recently main direction of Wendelstein stellarator is to develop modular coil system to confine currentless toroidal plasmas with significantly reduced parallel current. The W7-AS [100] is a present device and the W7-X [101] has been designed as the next generation device. In the W7-AS the L - H transition phenomena have also been observed in the ECRH plasmas without the net plasma current [102]. At present, it is realized only for a narrow region of the edge rotational transform, $\iota(a) \simeq 0.52$.

In Section 4.2, a brief derivation of the nonlinear poloidal viscosity for stellarator devices is shown. In Section 4.3, the nonlinear poloidal viscosity is calculated for the above devices; CHS, Heliotron E, LHD, W7-AS, W7-X and the optimized helical axis configuration described in Chapter 3. Although each device has many variations for experimental magnetic configurations, only one representative magnetic configuration is chosen except for the CHS. It is also noted that the parameters to describe magnetic field spectrum of each device are approximate to estimate the nonlinear poloidal viscosity. However, the sensitivity of the nonlinear poloidal viscosity was checked on the chosen parameters. Also momentum loss due to charge exchange reaction with neutral particles is evaluated. Characteristics of the nonlinear poloidal viscosity are discussed in these stellarators mentioned above and some comments will be given for results relevant to experiments. Main results are summarized in Section 4.4.

4.2 Nonlinear Incompressible Poloidal Viscosity

The poloidal and toroidal plasma viscosities can be calculated from the linearized drift kinetic equations with plasma flows [103, 104],

$$[(v_\parallel + V_\parallel)\hat{\boldsymbol{n}} + \boldsymbol{v}_E] \cdot \nabla f - C(f) = 2\frac{v^2}{v_T^2}\left(\frac{1}{2} - \frac{3}{2}\frac{v_\parallel^2}{v^2}\right)f_M\left[\boldsymbol{V} \cdot \nabla \ln B - L_1^{(3/2)}\frac{2}{5}\frac{\boldsymbol{q} \cdot \nabla \ln B}{P}\right],$$
(4.1)

where $\boldsymbol{V}$ is the mass flow velocity, $V_\parallel$ is the mass flow velocity parallel to $\boldsymbol{B}$, $\boldsymbol{v}_E$ is the $\boldsymbol{E} \times \boldsymbol{B}$ drift velocity, $v_\parallel$ is the particle speed parallel to $\boldsymbol{B}$, $\boldsymbol{q}$ is the heat flow, $L_1^{(3/2)} = (5/2) - v^2/v_T^2$, P is the plasma pressure, f_M is the Maxwellian distribution function, and $C(f)$ is the Coulomb collision operator. In the plateau-Pfirsch-Schlüter regime, Eq. (4.1) can be solved with a Krook collision term $C(f) = -\nu_k f$ with a proper choice of collision frequency ν_k. For a stellarator configuration, the magnetic field can be expressed in the standard toroidal coordinates (r, θ, ζ) as follows:

$$B = B_0(r)[1 - \sum_{mn}\epsilon_{mn}(r)\cos(m\theta - n\zeta)],$$

where B_0 is the magnetic field strength on the magnetic axis, m (n) is the poloidal (toroidal) mode number, and ϵ_{mn}'s are the amplitudes with the mode numbers (m, n). The resonant part of the solution of Eq. (4.1) in the plateau-Pfirsch-Schlüter regime for a large aspect ratio stellarator configuration is

$$f = 2\frac{v^2}{v_T^2}\left(\frac{1}{2} - \frac{3}{2}\frac{v_\parallel^2}{v^2}\right)f_M\left[-\left(\boldsymbol{V} \cdot \nabla \theta - L_1^{(3/2)}\frac{2}{5P}\boldsymbol{q} \cdot \nabla \theta\right)\sum_{mn}m\epsilon_{mn}R_{mn}\right.$$
$$\left.\sin(m\theta - n\zeta) + \left(\boldsymbol{V} \cdot \nabla \zeta - L_1^{(3/2)}\frac{2}{5P}\boldsymbol{q} \cdot \nabla \zeta\right)\sum_{mn}n\epsilon_{mn}\sin(m\theta - n\zeta)\right],$$
(4.2)

where $R_{mn} = \nu_k/[(m\omega_\theta - n\omega_\zeta)^2 + \nu_k^2]$, $\omega_\theta = (v_\parallel + V_\parallel)\chi'/B + \boldsymbol{v}_E \cdot \nabla \theta$, $\omega_\zeta = (v_\parallel + V_\parallel)\psi'/B + \boldsymbol{v}_E \cdot \nabla \zeta$. Here the Hamada coordinates is employed and $\psi' = \boldsymbol{B} \cdot \nabla \zeta$ and $\chi' = \boldsymbol{B} \cdot \nabla \theta$ for a magnetic field $\boldsymbol{B} = \boldsymbol{B}_p + \boldsymbol{B}_t = \psi'\nabla\hat{V} \times \nabla\theta - \chi'\nabla\hat{V} \times \nabla\zeta$, where $\hat{V}$ is the volume enclosed by the flux surface. The magnetic field has been described in the Hamada coordinates in the large aspect ratio limit which is appropriate for most of stellarators. Real spectrum of stellarator magnetic field has many Fourier components of helical magnetic field; however, dominant or truncated Fourier components are sufficient to calculate the poloidal plasma viscosity with reasonable accuracy. Here it is noted that the perturbed distribution function is linear in the magnetic perturbations and the viscosity is quadratic in them. Since the

helical magnetic components ϵ_{mn} with $m \neq 0$ and $n \neq 0$ are considered as the magnetic perturbations to the dominant axisymmetric field, it is allowed to neglect the higher order terms with respect to ϵ_{mn} in Eq. (4.2).

The poloidal plasma viscosity can be calculated from the definition [105]

$$\langle \boldsymbol{B}_p \cdot \nabla \cdot \boldsymbol{\Pi} \rangle = \langle \int d^3v m_A[(v^2/2) - (3v_\parallel^2/2)]f\boldsymbol{B}_p \cdot \nabla B/B \rangle,$$

which yields

$$\langle \boldsymbol{B}_p \cdot \nabla \cdot \boldsymbol{\Pi} \rangle = \frac{\sqrt{\pi}}{4}Nm_A v_T^2 B\sum_{mn}[I_{mn}\epsilon_{mn}^2 m(m\boldsymbol{V} \cdot \nabla\theta - n\boldsymbol{V} \cdot \nabla\zeta)$$
$$+ L_{mn}\epsilon_{mn}^2 m\frac{2}{5P}(m\boldsymbol{q} \cdot \nabla\theta - n\boldsymbol{q} \cdot \nabla\zeta)],$$
(4.3)

where N and m_A are plasma density and mass, respectively, I_{mn} and L_{mn} in Eq. (4.3) are given by

$$\left\{\begin{array}{c}I_{mn}\\L_{mn}\end{array}\right\} = \frac{1}{\pi}\int_0^\infty dx x^2 e^{-x}\left\{\begin{array}{c}1\\x - 5/2\end{array}\right\} \times \int_{-1}^1 dy(1 - 3y^2)^2\left(\frac{v\chi'}{B}\right)R_{mn},$$
(4.4)

where $x = v^2/v_T^2$, $y = v_\parallel/v$, $\nu_k = 3\nu_D + \nu_E$, and ν_D and ν_E are defined in Ref. [106]. Here the upper limit of the energy integral in Eq. (4.4) is extended to infinity by assuming bi-Maxwellian distribution function. The viscosity given by Eq. (4.3) is for the thermal ion component and the hot ions are assumed to undergo the orbit loss process discussed in Ref. [24]. It can be assumed that ion distribution is a Maxwellian. In this case, the upper limit of the integral in Eq. (4.4) should be $\nu_h^{*1/2} = (\nu_k Rq/v_T m\epsilon_h^{3/2})^{1/2}$, where $\epsilon_h = \epsilon_{lM}$ denotes the dominant helical magnetic component. It is also assumed that the largest value of E_r occurs at a distance about one thermal ion orbit size away from the plasma boundary. In the large aspect ratio toroidal coordinates (r, θ, ζ), the poloidal plasma viscosity in Eq. (4.3) is shown as [107]

$$-\frac{\langle \boldsymbol{B}_p \cdot \nabla \cdot \boldsymbol{\Pi} \rangle}{Nm_A v_T^2\chi'} = \frac{\sqrt{\pi}}{4}\sum_{mn}\epsilon_{mn}^2 m(m - nq)$$
$$\times \left\{I_{mn}\left[\frac{V_\parallel}{v_T} + \frac{m}{m - nq}(M_p - V_{p,P})\right] - L_{mn}\frac{m}{m - nq}V_{p,T}\right\}$$
$$+ \epsilon_i^2\left(\frac{\nu_{eff}}{(v_T/qR)}\right)\left(\frac{V_\parallel}{(v_T q^2)} + 2M_p - 2V_{p,P}\right),$$
(4.5)

where $V_{p,P} = -c(dP/dr)/(Nev_T B_p)$, $V_{p,T} = -c(dT/dr)/(ev_T B_p)$, and $M_p = -cE_r/(B_p v_T)$. In obtaining Eq. (4.5), it is employed a conversion formula to express Hamada coordinates in terms of standard toroidal coordinates for

a tokamak [108]. Thus Eq. (4.5) is approximate. It is also assumed that $V_{\parallel}/v_T \sim 0$ and $1 + 2q^2 \sim 2q^2$ with $q = \epsilon_t(B/B_p)$, where ϵ_t corresponds to $\epsilon_{1,0}$. It is noted that M_p is positive for $E_r < 0$. The second term in Eq. (4.5) is related to the charge exchange momentum loss and $\nu_{eff} = N_n\langle\sigma v\rangle_{cx}$, where N_n is the neutral density and $\langle\sigma v\rangle_{cx}$ is the reaction rate of charge exchange reaction.

The physical model of the L - H transition based on the nonlinear poloidal viscosity is explained briefly in Appendix C.

4.3 Magnetic Spectrum and Poloidal Viscosity of Recent Stellarators

4.3.1 CHS

Recently H mode or H mode like transport barrier has been observed in the CHS [22] and the W7-AS [102]. First, nonlinear poloidal viscosity is calculated for the CHS. In the CHS, H mode like transitions occur in NBI plasmas with the toroidal plasma current. The line averaged electron density rises while the H_α signal drops, and the electron density profile steepens near the plasma edge.

In the case of the CHS I (standard), a model magnetic field is described in the (r, θ, ζ) coordinates as $B/B_0 = 1 - \cos\theta - \epsilon_h\cos(2\theta - 8\zeta)$, where $\epsilon_t = \epsilon_{1,0} = 0.136$ and $\epsilon_h = \epsilon_{2,8} = 0.21$ as listed in Table 4.1 (see CHS I). It is noted that these values reproduce the magnetic structure near the edge region with $q_{edge} = 1.25$ approximately. For a particular magnetic surface in the CHS, ϵ_t and ϵ_h at $q_{edge} = 1.25$ are somewhat different and satellite magnetic components also appear. However, the satellite magnetic components of the CHS affect the nonlinear poloidal viscosity very weakly as will be discussed later.

The damping of the toroidal rotation by the helical magnetic field component $\epsilon_h\cos(m\theta - n\zeta)$ is strong because usually $nq \gg m$ [91]. Thus the toroidal viscosity of stellarator can compete with the charge exchange momentum loss mechanism in damping the toroidal rotation [109]. It is assumed here that the toroidal rotation is damped so that $V_{\parallel}/v_T \sim 0$. It is shown that the damping of the poloidal rotation by the charge exchange momentum loss mechanism is not as large as the damping of the toroidal rotation, where a factor of ϵ_t^2 appears in front of charge exchange poloidal rotation damping term in Eq. (4.5). However, this term affects the poloidal viscosity significantly as will be shown later. With the approximation $V_{\parallel}/v_T \sim 0$, the right hand side of Eq. (4.5) becomes an equation of E_r for a given set of values of $V_{p,P}$ and $V_{p,T}$.

Figure 4.1 shows the normalized poloidal viscosity

$$\Pi_{p,n} = \langle \boldsymbol{B}_p \cdot \nabla \cdot \boldsymbol{\Pi} \rangle / (N m_i v_T^2 \chi' \sqrt{\pi}/4) \tag{4.6}$$

versus poloidal Mach number M_p in the CHS I for $V_{p,P} = 0.2$, $V_{p,T} = 0.1$ and $\nu_{*i} = \nu_k^i Rq/(v_T\epsilon_t^{3/2}) = 12$, where ν_k^i is $\nu_k = 3\nu_D + \nu_E$ for ions [106]. In

Ref. [107], $V_{p,P} = 0.1$ and $V_{p,T} = 0.2$ are assumed; however, effects of these choices on $\Pi_{p,n}$ is fairly weak. When $\nu_{eff}/(v_T/Rq)$ is decreased from 1.0 to 0.1, local maximum of $\Pi_{p,n}$ appears at $M_p \sim 7.0$ which is somewhat larger than $M_p \sim |m - nq|/m$ for $m = 2$, $n = 8$ and $q_{edge} = 1.25$. Figure 4.2 shows $\Pi_{p,n}$ versus M_p for the less collisional plasma with $\nu_{*i} = 1$ in the CHS I. Here $\Pi_{p,n}$ has two clear local maxima for $\nu_{eff}/(v_T/Rq) = 0.1$; $M_p \sim 1.8$ and $M_p \sim 6.8$.

It is shown that the Mach number corresponding to the local maximum of $\Pi_{p,n}$ decreases, when the upper limit of the integral $\nu_h^{*1/2}$ in I_{mn} and L_{mn} is decreased from the infinity. In Fig. 4.3(a), the second local maximum of $\Pi_{p,n}$ moves from $M_p \sim 6.8$ in Fig. 4.2 to $M_p \sim 3.6$ for $\nu_{*i} = 1.0$, $\nu_h^{*1/2} = 1.0$ and $\nu_{eff}/(v_T/Rq) = 0.1$, although the first local maximum of $\Pi_{p,n}$ almost disappears. For $\nu_{*i} = 1.0$, $\nu_h^{*1/2} = 1.0$ and $\nu_{eff}/(v_T/Rq) = 0$ or no charge exchange momentum loss in Fig. 4.3(b), the first local maximum appears clearly at $M_p \sim 0.8$. From Fig. 4.1 and Fig. 4.3, the decrease of $\nu_{eff}/(v_T/Rq)$ is not effective to obtain the local maximum of $\Pi_{p,n}$ at $M_p \sim 1.5 - 2$, in the collisional plasma with $\nu_{*i} \sim 10 - 12$.

Here the effect of aspect ratio on $\Pi_{p,n}$ in the CHS is examined by increasing ϵ_t artificially (see CHS II in Table 4.1) but there is no significant change of $\Pi_{p,n}$ between Fig. 4.2(b) and Fig. 4.4. Next, satellite magnetic components of $\epsilon_{1,8} = -0.05$ and $\epsilon_{3,8} = 0.05$ (see CHS III in Table 4.1) are included in the calculation of $\Pi_{p,n}$ but again there is no significant change of $\Pi_{p,n}$ between Fig. 4.2(b) and Fig. 4.5. It is noted that these values of $\epsilon_{1,8}$ and $\epsilon_{3,8}$ are chosen just for evaluation and do not correspond to a particular configuration.

According to the L - H transition theory the local maxima of $\Pi_{p,n}$ have a possibility to realize the H mode. From this point of view the first local maximum with lowest Mach number M_p is most important. In the CHS, when both ν_{*i} and $\nu_{eff}/(v_T/Rq)$ become small, $\nu_{*i} \lesssim 1$ and $\nu_{eff}/(v_T/Rq) \lesssim 0.1$, the first local maximum exists at $M_p \sim 1.8$. However, since the second local maximum exists at $M_p \sim 7$, $\Pi_{p,n}$ in the region of $M_p \sim 2.5$ does not decrease significantly. This result may suggest that the improvement of energy confinement of the H mode like discharges in the CHS is not large, which seems consistent with the experiment [22]. One question related to the experiment is that the H mode like transition occurs only for current carrying plasmas on the order of $(10 - 20)$ kA and it does not occur for currentless plasmas. It is speculated that MHD fluctuations observed in the current carrying CHS

plasmas produce a heat pulse propagating from the core to the edge region. Ions in the edge region are heated by this heat flow and ν_{*i} is decreased from $\nu_{*i} \gtrsim 5$ to $\nu_{*i} \sim 1$, which makes it possible to have the local maximum of $\Pi_{p,n}$. Since MHD fluctuation levels are usually lower in currentless plasmas, the above scenario is not expected for the currentless operation.

4.3.2 Heliotron E

The Heliotron E (H-E) has a large aspect ratio, $\epsilon_t = 0.1$ and a large helical magnetic component with $m = 2$ and $n = 19$, $\epsilon_h = \epsilon_{2,19} = 0.25$ (see H-E in Table 4.1). Also the edge rotational transform is large, $q_{edge} = 0.5$.

Figure 4.6 shows $\Pi_{p,n}$ versus M_p in the H-E for a collisional plasma with $\nu_{*i} = 12$. For collisional plasmas the first local maximum at $M_p \sim 1.5 - 2$ is obtained when the charge exchange momentum loss is extremely small, $\nu_{eff}/(v_T/Rq) = 0.01$. Figure 4.7 shows $\Pi_{p,n}$ versus M_p for a weakly collisional plasma with $\nu_{*i} = 1.0$. In this case the first local maximum of $\Pi_{p,n}$ appears at $M_p \sim 1.8$ for $\nu_{eff}/(v_T/Rq) = 0.1$. Thus the decrease of ν_{*i} is the key problem in order to obtain the L - H transition in the H-E. It is noted that $\Pi_{p,n}$ shown in Fig. 4.7(b) resembles to that in Fig. 4.2(b) for the CHS. This suggests that the L - H transition will be possible also in the H-E, if it is realized in a currentless CHS plasma.

4.3.3 LHD

The LHD is the next generation device under construction. The inverse aspect ratio, $\epsilon_t = 0.14$, is larger than that of H-E. It is expected that higher temperature plasmas with temperatures of 1-5 keV will be confined stably [13]. Figure 4.8 shows $\Pi_{p,n}$ versus M_p for a collisional plasma with $\nu_{*i} = 12$. When $\nu_{eff}/(v_T/Rq) < 0.1$, the first local maximum of $\Pi_{p,n}$ appears marginally. Figure 4.9 shows $\Pi_{p,n}$ versus M_p for a weakly collisional plasma with $\nu_{*i} = 1.0$. In this case the first local maximum of $\Pi_{p,n}$ appears for $\nu_{eff}/(v_T/Rq) \sim 0.1$. It seems that the L - H transition is realized in the LHD as in the CHS by comparing Figs. 4.8 and 4.9 with Figs. 4.1 and 4.2.

4.3.4 W7-AS

The W7-AS was designed to reduce PSC with modular coil system, which is related to reduction of the neoclassical transport and improvement of equi-

librium beta limit [100]. However, the W7-AS has many magnetic field components such as $(m,n) = (0,-5),(1,5),(2,-5),(1,-10)$. It is noted that the $(m,n) = (0,-5)$ component does not contribute to the nonlinear poloidal viscosity in Eq. (4.5). The W7-AS device has five field period ($M = 5$) and Fourier components of the magnetic field spectrum are shown in Table 4.1, which are estimated from Ref. [14]. Here $\epsilon_{0,-5}, \epsilon_{2,-5}, \epsilon_{1,-10}$ are taken into account instead of $\epsilon_{0,5}, \epsilon_{2,5}, \epsilon_{3,5}$.

In the W7-AS, H mode phases can last up to 0.2 s and show almost all the characteristics known from tokamaks, such as the drop in the H_α signal associated with edge localized modes (ELMs), as well as the development of an edge transport barrier, an increase of the poloidal impurity flow velocity and a reduction of the fluctuations in this region.

Figure 4.10 shows $\Pi_{p,n}$ versus M_p for a collisional plasma with $\nu_{*i} = 12$. Even when the charge exchange momentum loss is not so large, $\nu_{eff}/(v_T/Rq) = 0.5$, there is no local maximum of $\Pi_{p,n}$. For $\nu_{eff}/(v_T/Rq) = 0.01$, the local maximum of $\Pi_{p,n}$ appears at $M_p \sim 2.0$. In the W7-AS case, only the first local maximum of $\Pi_{p,n}$ is clearly seen for $\nu_{eff}/(v_T/Rq) \sim 0.01$ (see Fig. 4.10 and Fig. 4.11). Here it is noted that the local maximum value of $\Pi_{p,n}$ appeared for $\nu_{eff}/(v_T/Rq) \sim 0.01$ is not large.

From results shown in Figs. 4.10 and 4.11, it is suggested that the decrease of ν_{*i} is as important as the decrease of neutral density, since the local maximum of $\Pi_{p,n}$ appears for $\nu_{*i} = 1$ and $\nu_{eff}/(v_T/Rq) \sim 0.5$. In order to obtain the L - H transition in the W7-AS ECRH plasma, a high density plasma with $n \gtrsim n_{cr}$ is required, where $n_{cr} \sim (4-5) \times 10^{13}$ cm^{-3} at $B = 2.5$ T. When the density becomes high in the ECRH plasma, the ion temperature increases due to Coulomb energy transfer from electrons to ions. This tendency seems consistent with the above suggestions. Also the rotational transform to obtain the L - H transition is limited to $\iota(a) \sim 0.52$ in the W7-AS. This may not be related to the nonlinear poloidal viscosity. Usually separatrix configuration is favorable to realize the clear H mode from tokamak experiments. By considering that the separatrix appears at $\iota(a) \sim 0.5$ and $\iota(a)$ increases due to the finite beta effect, the above value of $\iota(a) \sim 0.52$ may belong to a possible range to obtain the L - H transition.

It is noted that the above values of $\Pi_{p,n}$ for the W7-AS are smaller than those for the CHS and the LHD, which makes it easier to generate the poloidal flow with a fairly small ion orbit loss flux (see Eq. (C.2) in Appendix C). This

may be a reason that the L - H transition phenomena have been observed in the currentless plasma of the W7-AS.

4.3.5 W7-X

The magnetic configuration for the W7-X device [101] is designed to realize the quasi-helically symmetric stellarator [15]. It has five field period ($M = 5$) and the Fourier component of $(m,n) = (1,5)$ is dominant. Significant feature of the Fourier spectrum is the bumpy component, $(m,n) = (0,5)$, with the opposite sign to the main helical component is realized to reduce the bootstrap current which changes the magnetic configuration substantially in finite beta plasmas. Therefore the Fourier component of $(m,n) = (0,5)$ is included as shown in Table 4.1, although it does not affect the nonlinear poloidal viscosity. The toroidicity corresponding to $\epsilon_{1,0}$ is decreased significantly compared to the geometrical inverse aspect ratio with the careful design of the modular coil system.

Figure 4.12 shows $\Pi_{p,n}$ versus M_p for a collisional plasma with $\nu_{*i} = 12$. Even for $\nu_{eff}/(v_T/Rq) < 1$, the first local maximum of $\Pi_{p,n}$ appears marginally at $M_p \sim 1.8$. The decrease of $\Pi_{p,n}$ in the region of $M_p \sim 2.5$ is not large even for $\nu_{eff}/(v_T/Rq) = 0.01$. In the case of $\nu_{*i} = 1.0$ shown in Fig. 4.13, the behavior of $\Pi_{p,n}$ is not so different from Fig. 4.12. Thus the L - H transition will be expected in the W7-X if the nonlinear poloidal viscosity plays an important role and the neutral density at the plasma edge region is decreased substantially.

4.3.6 Optimized Helical Axis Configuration

Finally, nonlinear poloidal viscosity is evaluated for the optimized helical axis configuration described in Chapter 3. It has four field period ($M = 4$) and $\epsilon_h = \epsilon_{1,4}$, $\epsilon_t = \epsilon_{1,0}$ and $\epsilon_b = \epsilon_{0,4}$ are dominant Fourier components of the magnetic field. This structure is similar to that of the W7-X, although $\epsilon_{1,0}$ is not reduced from the geometrical inverse aspect ratio. Figure 4.14 shows $\Pi_{p,n}$ versus M_p for a collisional plasma with $\nu_{*i} = 12$. Even for $\nu_{eff}/(v_T/Rq) < 1$, the first local maximum of $\Pi_{p,n}$ appears very weakly at $M_p \sim 2.0$. In the less collisional case, $\nu_{*i} = 1.0$, as shown in Fig. 4.15, the behavior of $\Pi_{p,n}$ is similar to that of the W7-AS case, although the value of $\Pi_{p,n}$ is about one order of magnitude larger. It is noted that the clear first local maximum is not seen in the W7-X case (Fig. 4.13) for the same values of $(\nu_{*i}, \nu_{eff}/(v_T/Rq))$. Thus

it is considered that the unreduced $\epsilon_{1,0}$ or relatively large fraction of $\epsilon_{1,0}/\epsilon_{1,4}$ contributes to make a clear "tokamak like" local maximum at $M_p \sim 1$.

It is expected from above results that the L‑H transition is possible in the optimized helical axis configuration with the similar nonlinear poloidal viscosity to that in the W7-AS.

4.4   Summary

The tokamak L‑H transition theory has been applied to present and next generation stellarator devices (CHS, Heliotron E, LHD, W7-AS, W7-X and the optimized helical axis configuration described in Chapter 3) in a controlled manner by making use of the two or more local maxima in poloidal viscosity as a function of the poloidal Mach number. Depending on the relative magnitudes of the magnetic field spectrum, the local maxima in poloidal viscosity, and thus, the transition can occur either at a critical poloidal Mach number M_p on the order of unity, similar to that of a tokamak, or at M_p on the order of $|m-nq|/m$, similar to that of a helically symmetric torus. Therefore, the underlying L‑H transition dynamics in stellarators can be investigated by performing the L‑H transition experiments on either a stellarator with an adjustable magnetic field spectrum such as HHHS or on several stellarators with different magnetic field spectrum.

In order to observe the clear local maximum of the poloidal viscosity, it is effective not only to reduce the ion-ion collision frequency but also to reduce the effect of the charge exchange momentum loss by controlling the edge neutral density. Therefore, it is considered that the good divertor function is necessary to realize L‑H transition from the latter point.

Some results in this chapter seem consistent with the experimental observations in stellarator H mode experiments. The possibilities of the L‑H transition in the major next generation stellarator devices, the LHD and the W7-X, are also shown. It is also expected that the L‑H transition is possible in the optimized helical axis configuration, in which the behavior of nonlinear poloidal viscosity is similar to that of the W7-AS.

Finally, it should be noted that it is necessary to exceed dominant local maxima to have a stellarator H mode as good as that of tokamaks [110]. This can be made easier if $|m - nq|/m$ is close to unity, i.e., similar to that of tokamaks, for example, by decreasing n of the main helical field.

	$\epsilon_{1,0}$	$\epsilon_{0,M}$	$\epsilon_{1,M}$	$\epsilon_{2,M}$	$\epsilon_{3,M}$	q_{edge}
CHS ($M=8$)						
I	0.136	0.0	0.0	0.21	0.0	1.25
II	0.17	0.0	0.0	0.21	0.0	1.25
III	0.136	0.0	-0.05	0.21	0.05	1.25
Heliotron E ($M=19$)	0.1	0.0	0.0	0.25	0.0	0.5
LHD ($M=10$)	0.14	0.0	0.0	0.24	0.0	1.0
		$(\epsilon_{0,-5})$		$(\epsilon_{1,-10})$	$(\epsilon_{2,-5})$	
W7-AS ($M=5$)	0.053	0.029	0.036	0.024	0.025	1.92
W7-X ($M=5$)	0.03	0.125	0.08	0.0	0.0	1.15
Optimized helical axis configuration ($M=4$)	0.12	0.15	0.14	0.0	0.0	1.4

Table.4.1 Model magnetic field spectrum for calculation of the nonlinear incompressible poloidal viscosity.
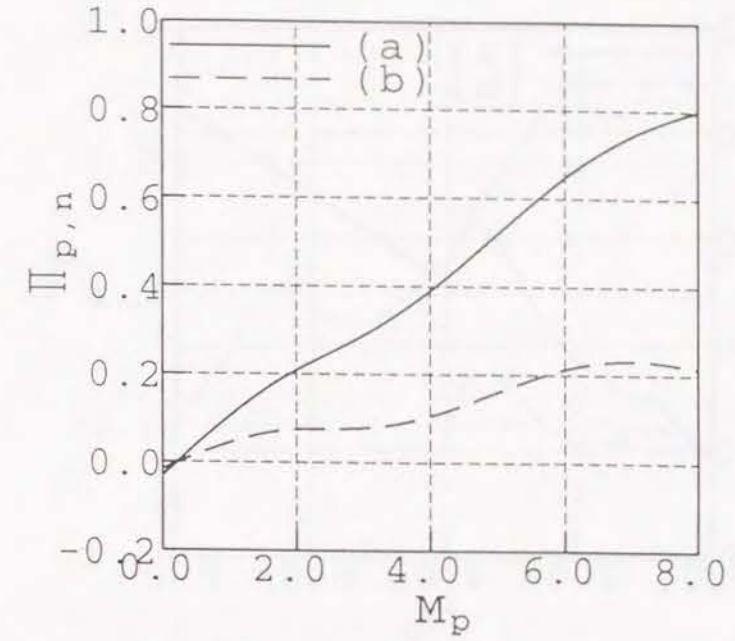

Fig. 4.1: Normalized poloidal viscosity $\Pi_{p,n}$ versus poloidal Mach number M_p in CHS (standard) for (a) $(\nu_{*i}, \nu_{eff}/(v_T/Rq)) = (12, 1.0)$ and (b) $(12, 0.1)$.
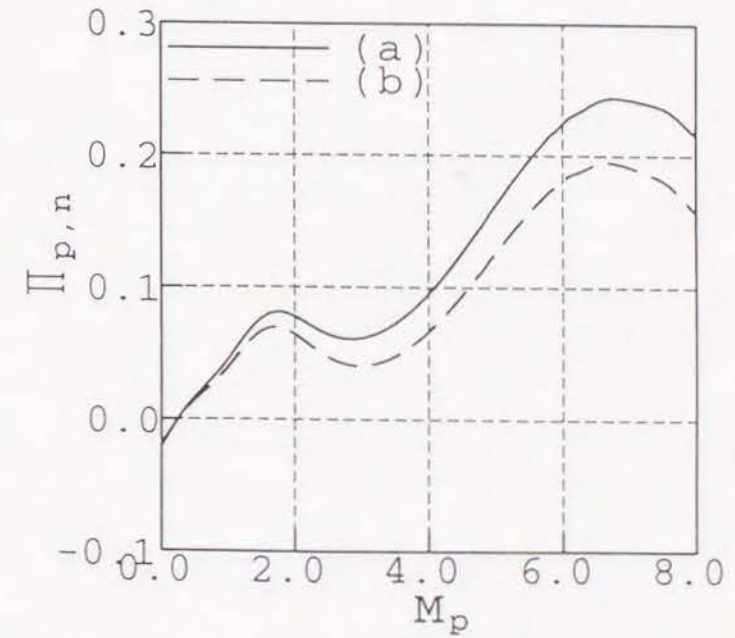

Fig. 4.2: $\Pi_{p,n}$ versus M_p in CHS (standard) for (a) $(\nu_{*i}, \nu_{eff}/(v_T/Rq)) = (1.0, 0.1)$ and (b) $(1.0, 0.01)$.
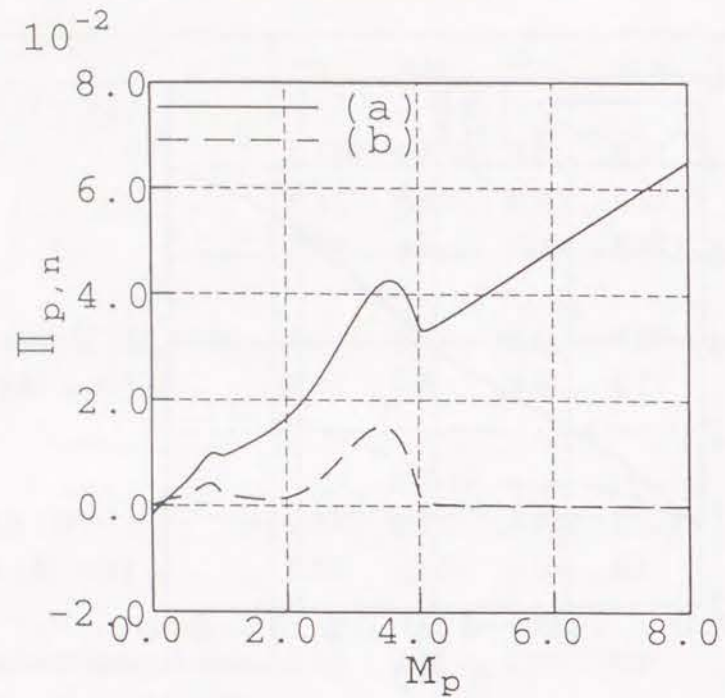
Fig. 4.3: $\Pi_{p,n}$ versus M_p in CHS (standard) for
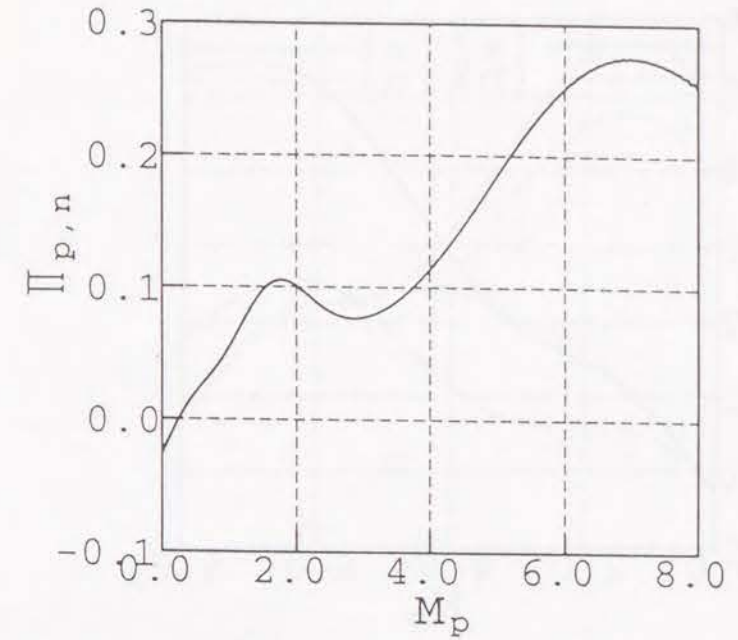(a) $(\nu_{*i}, \nu_h^{*1/2}, \nu_{eff}/(v_T/Rq)) = (1.0, 1.0, 0.1)$ and (b) $(1.0, 1.0, 0.0)$.

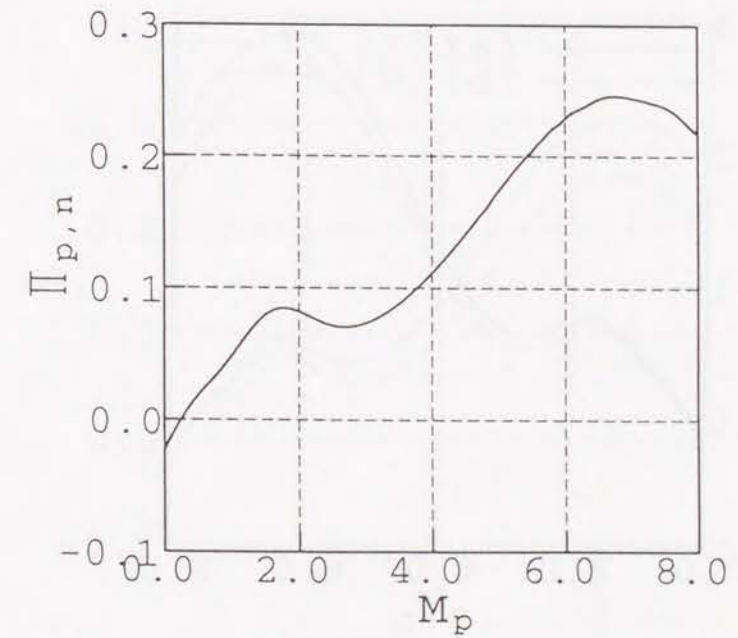**Fig. 4.4**: $\Pi_{p,n}$ versus M_p in CHS II for $(\nu_{*i}, \nu_{eff}/(v_T/Rq)) = (1.0, 0.1)$.

Fig. 4.5: $\Pi_{p,n}$ versus M_p in CHS III for $(\nu_{*i}, \nu_{eff}/(v_T/Rq)) = (1.0, 0.1)$.
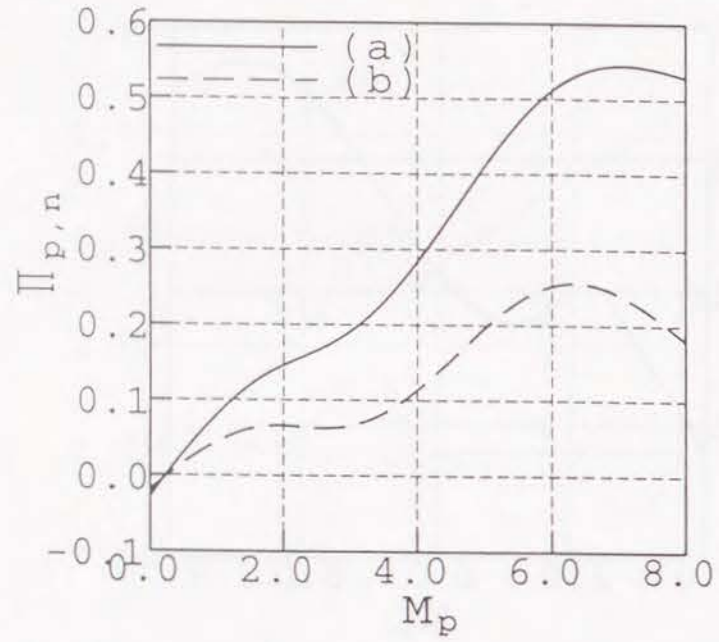
Fig. 4.6: $\Pi_{p,n}$ versus M_p in Heliotron E for (a) $(\nu_{*i}, \nu_{eff}/(v_T/Rq)) = (12, 1.0)$ and (b) $(12, 0.01)$.
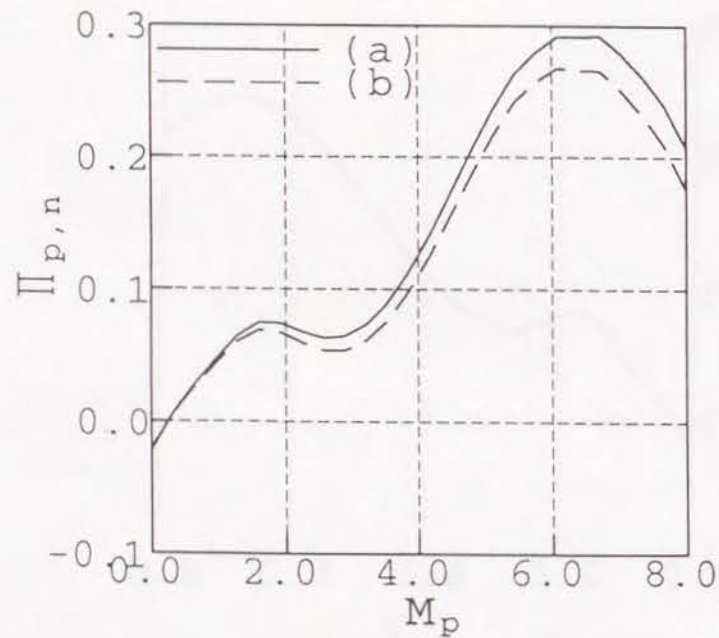

Fig. 4.7: $\Pi_{p,n}$ versus M_p in Heliotron E for (a) $(\nu_{*i}, \nu_{eff}/(v_T/Rq)) = (1.0, 0.1)$ and (b) $(1.0, 0.01)$.
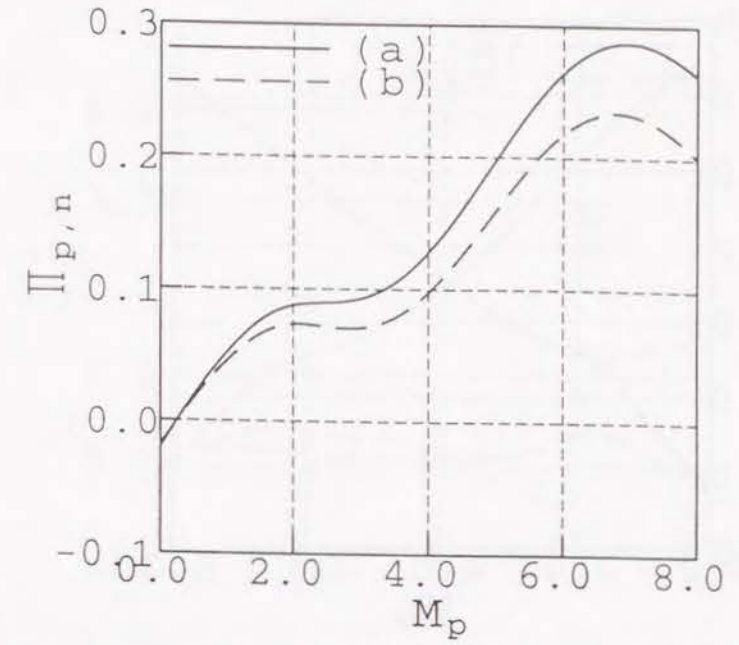

Fig. 4.8: $\Pi_{p,n}$ versus M_p in LHD for (a) $(\nu_{*i}, \nu_{eff}/(v_T/Rq)) = (12, 0.1)$ and (b) $(12, 0.01)$.
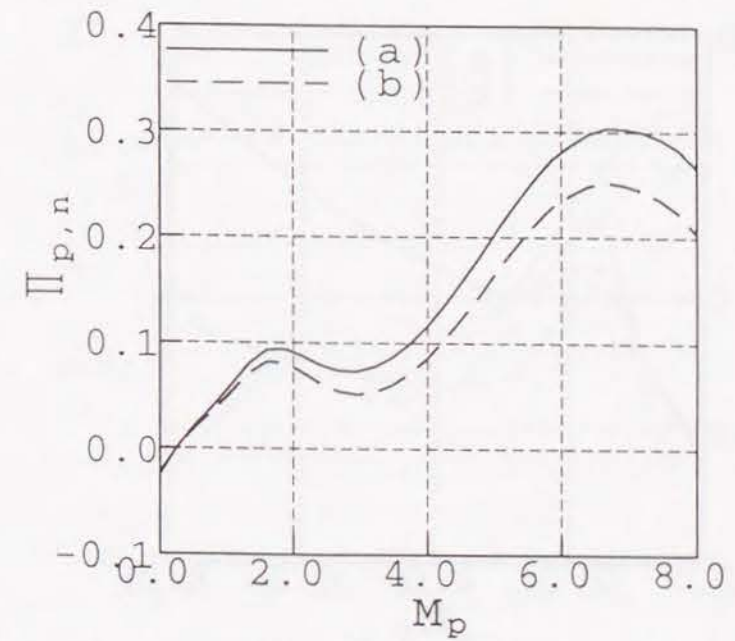

Fig. 4.9: $\Pi_{p,n}$ versus M_p in LHD for (a) $(\nu_{*i}, \nu_{eff}/(v_T/Rq)) = (1.0, 0.1)$ and (b) $(1.0, 0.01)$.

104

105

Fig. 4.10: $\Pi_{p,n}$ versus M_p in W7-AS for (a) $(\nu_{*i}, \nu_{eff}/(v_T/Rq)) = (12, 0.5)$ and (b) $(12, 0.01)$.

Fig. 4.11: $\Pi_{p,n}$ versus M_p in W7-AS for (a) $(\nu_{*i}, \nu_{eff}/(v_T/Rq)) = (1.0, 0.1)$ and (b) $(1.0, 0.01)$.

Fig. 4.12: $\Pi_{p,n}$ versus M_p in W7-X for (a) $(\nu_{*i}, \nu_{eff}/(v_T/Rq)) = (12, 1.0)$ and (b) $(12, 0.01)$.

Fig. 4.13: $\Pi_{p,n}$ versus M_p in W7-X for (a) $(\nu_{*i}, \nu_{eff}/(v_T/Rq)) = (1.0, 0.1)$ and (b) $(1.0, 0.01)$.
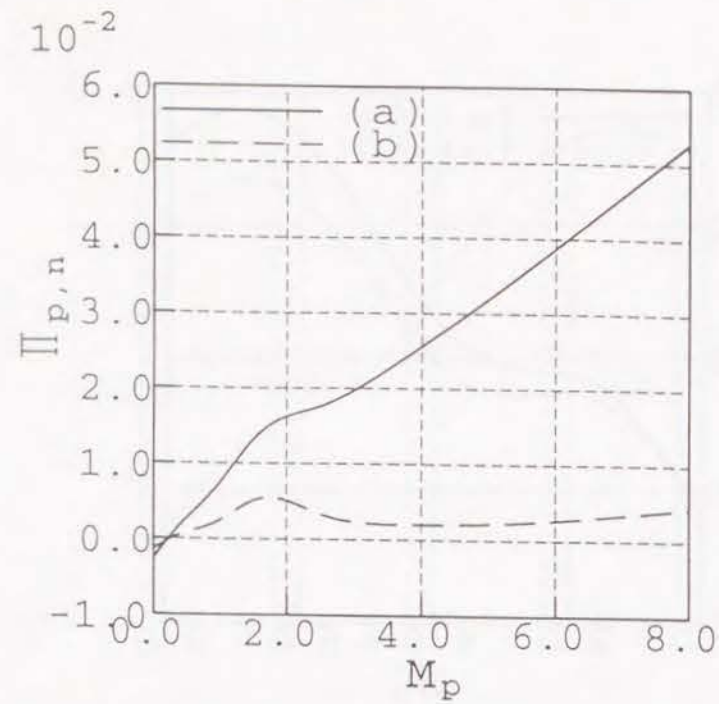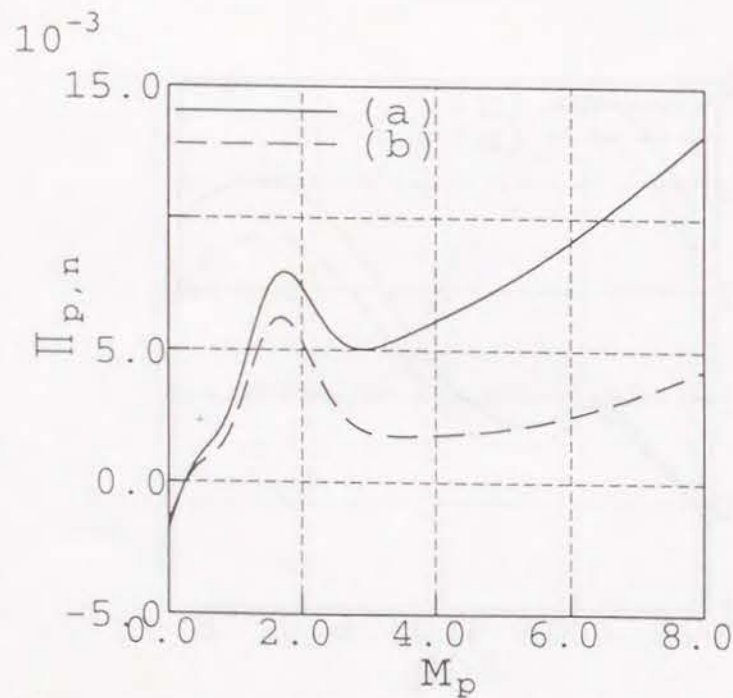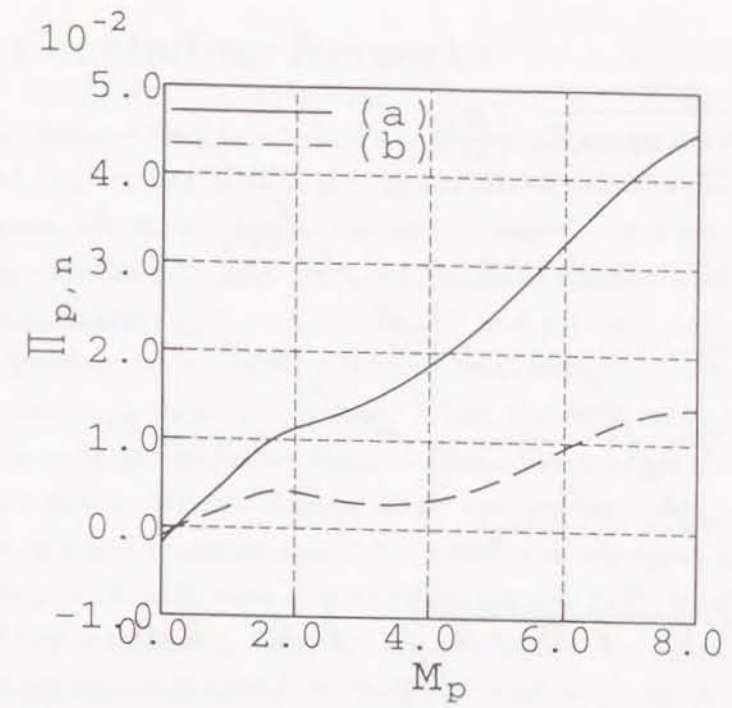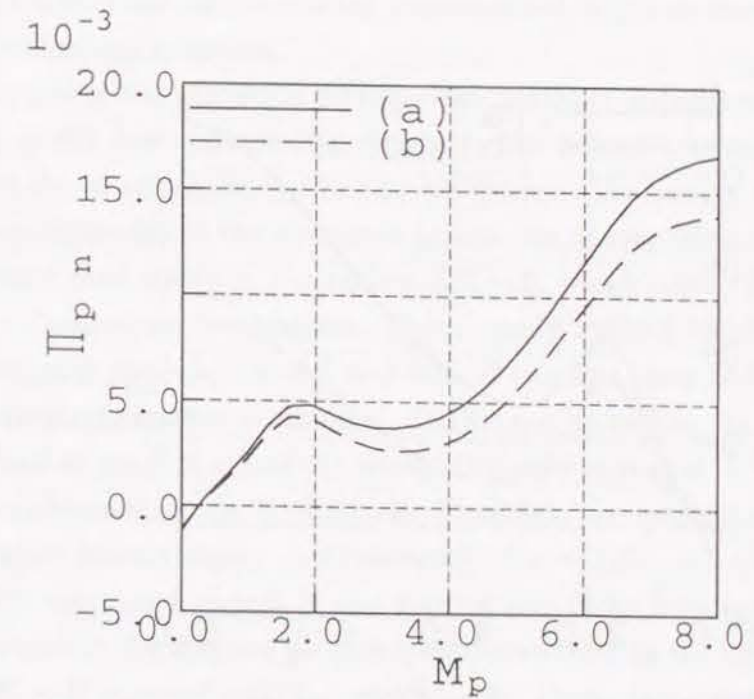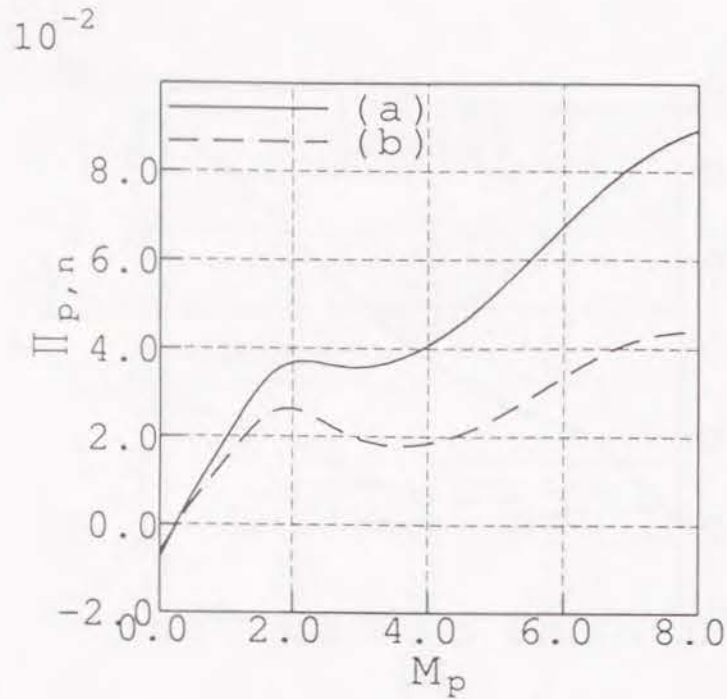
10^{-2}

Fig. 4.14: $\Pi_{p,n}$ versus M_p in the optimized helical axis configuration for (a) $(\nu_{*i}, \nu_{eff}/(v_T/Rq)) = (12, 0.1)$ and (b) $(12, 0.01)$.
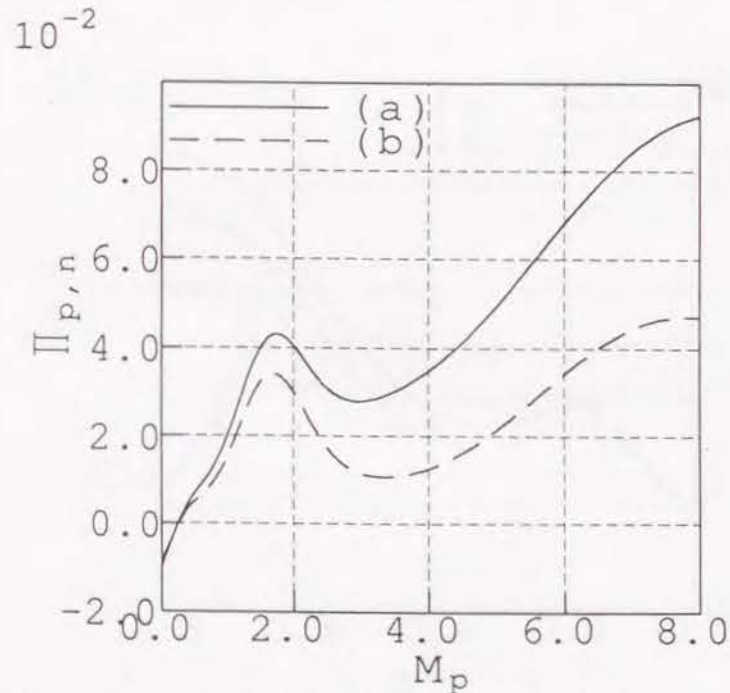
10^{-2}

Fig. 4.15: $\Pi_{p,n}$ versus M_p in the optimized helical axis configuration for (a) $(\nu_{*i}, \nu_{eff}/(v_T/Rq)) = (1.0, 0.1)$ and (b) $(1.0, 0.01)$.

5 Concluding Remarks

In this thesis, several new helical axis stellarator configurations, Helias-Heliac Hybrid Stellarator (HHHS) and the optimized helical axis configuration, are presented, which have been obtained by theoretical guidances for compatibility between the high beta limit and the good trapped particle confinement.

Combinations of $l = 1$ helical coil and poloidal and toroidal coils allow a freedom for controlling the magnetic field spectrum by adjusting the coil currents in these coil system. Thus the wide range of magnetic configurations including Helias-like and Heliac-like configuration are possible in a single device, HHHS. Among these two representative configurations in HHHS, Heliac-like configuration has a sufficient vacuum magnetic well, contributing to the high limit of beta value, $\langle \beta \rangle_{st} \sim 7.3\%$, which is evaluated by ideal Mercier criterion. However, the neoclassical transport is not optimized due to the enhancement of the magnetic field ripple by the broad spectrum of the magnetic field, although the particle diffusivity is about one order of magnitude smaller than that of Helias-like configuration by controlling the bumpy component. The bumpy component is large and has the same sign as the helical one and causes the enhancement of the magnetic field ripple in Helias-like configuration.

Applying the analytical neoclassical transport analysis with multiple helicity in the low collisionality regime to the helical axis configurations has led to the attention on the bumpy component; the bumpy component with the opposite sign to the dominant helical one is very effective to reduce the magnetic field ripple in the region of $\theta \sim 0$, which results in the reduction of neoclassical ripple transport. This is easily realized by changing the sign of the pitch modulation of $l = 1$ helical coil and then the optimized helical axis configuration is obtained. In this configuration, the plateau level of neoclassical particle diffusivity almost the same as that of its equivalent tokamak is obtained by the DKES code. Moreover, the vacuum magnetic well in the entire plasma region contributes to $\langle \beta \rangle_{st} \sim \langle \beta \rangle_{eq} \sim 4.5\%$. Collisionless particle orbit confinement is also studied and finite beta and radial electric field improve the trapped particle confinement due to the diamagnetic effect and $\boldsymbol{E} \times \boldsymbol{B}$ poloidal rotation, respectively. Bootstrap current, which has a possibility to cause the extensive low order rational surfaces in low shear stellarators, is controllable by the bumpy field component and this is desirable

to investigate the effects of bootstrap current in finite beta plasmas. Above mentioned capability of this magnetic configuration is similar to the W7-X from the point of views of beta limit, neoclassical transport and high energy particle confinement; however, this helical axis stellarator does not use modular coils as in the W7-X. It should be noted that the ϵ_t component in the magnetic field spectrum is not reduced from the geometrical inverse aspect ratio, which causes the substantial change of rotational transform for finite beta plasmas.

In addition to the above favorable properties for high temperature plasma confinement, the large clearance between the helical coil and the outermost magnetic surface, and the one between the chamber surface and the outermost magnetic surface are advantageous for plasma heating and diagnostics in designing a new experimental device.

One weak point of the above mentioned optimization is that the understanding of the anomalous transport governing the plasma confinement in the realistic situations is not mature. In this case, it is important to develop ways to suppress the anomalous transport. From the tokamak experiments, the L - H transition is reliable to improve confinement time with about a factor of two. Since there is a significant difference in the magnetic configuration between stellarators and tokamaks, H mode experiments in stellarators are important in clarifying the L - H transition physics. One of the explanations of the physical mechanisms for the L - H transition in tokamaks is extended and applied to stellarator configurations to clarify the characteristics of present and next generation stellarator devices (CHS, Heliotron E, LHD, W7-AS, W7-X and the optimized helical axis configuration considered in this thesis) from the L - H transition point of view. This theory is based on the bifurcation of the radial electric field E_r through the existence of a local maximum in the plasma poloidal viscosity as a function of poloidal flow velocity.

In order to obtain the clear local maximum of the poloidal viscosity, reduction of the charge exchange momentum loss by suppressing the edge neutral density is very effective in addition to the reduction of ion-ion collision frequency.

The local maxima in poloidal viscosity depends on the relative magnitudes of the magnetic field spectrum, and thus, the transition may occur either at a critical poloidal Mach number M_p on the order of unity corresponding to

that of a tokamak, or at M_p on the order of $|m - nq|/m$ corresponding to that of a helically symmetric torus. Here, m (n) is the poloidal (toroidal) mode number of the main helical field. Therefore, the underlying L - H transition dynamics in stellarators may be clarified by performing L - H transition experiments on either a stellarator with an adjustable magnetic field spectrum such as HHHS or on several stellarators with different magnetic field spectrum, which will give the further tests of this theory. From the theoretical results in Chapter 4, the L - H transition is also expectable in the optimized helical axis configuration discussed in Chapter 3.

The future studies concerning the subjects in this thesis are described briefly.

In the optimized helical axis configuration described in Chapter 3, the toroidal component ϵ_t in the magnetic spectrum is not reduced from the geometrical inverse aspect ratio. The toroidal effect is the origin of the Pfirsch-Schlüter current which changes the rotational transform profile substantially. If this change degrades confinement property due to magnetic island generation, an effort will be necessary to decrease the ϵ_t component. It is noted that this ϵ_t component also causes the $1/\nu$ ripple diffusivity a little larger than that of the W7-X, although it can be reduced to the level of the W7-X by controlling the bumpy field component. As for the MHD equilibrium, a free boundary equilibrium calculation is also required to study the effect of the vertical field control for finite beta plasmas. In this thesis, the structure of magnetic field lines is studied only for the vacuum configurations. The free boundary MHD equilibrium will clarify the magnetic structure in the region outside the outermost magnetic surface also for finite beta plasmas. It is also necessary to follow particle orbits of higher energy particles to clarify α particle confinement definitively.

As for the L - H transition theory described in Chapter 4, $V_\parallel/v_T \sim 0$ is assumed due to the damping of the toroidal rotation is stellarators. However, this assumption is not necessary. It is possible to obtain the parallel flow speed $V_\parallel$ in the steady state solution satisfying the poloidal and toroidal momentum equations simultaneously [111]. Further comparisons with experimental results are necessary to clarify the role of the plasma flow on L - H transition physics.

If this type of device based on the modulated $l = 1$ helical coil system is built, it will contribute to investigate physics of helical axis stellarators in

addition to W7-X, TJ-II and HSX etc. and also to the stellarator physics. Considerable subjects expected to become clear are as follows;

- anomalous transport caused by the egde turbulence and its relation to the magnetic well or hill configuration,
- inter-relation between trapped particle orbit loss and generation of radial electric field,
- magnetic field line structure outside the outermost magnetic surface (wide stochastic layer, clear divertor structure) and its influence on the bulk plasma confinement,
- relation between anomalous transport and the magnetic field spectrum.

Finally, it is added that the above described concept of the optimized helical axis configuration is one of the candidates for the next experimental device at the Institute of Advanced Energy (IAE), Kyoto University.

A DKES code
— Code for Neoclassical Transport Coefficients —

The neoclassical transport coefficients for particle diffusion, energy diffusion, bootstrap current and Ware pinch can be computed by the DKES code [47]. In this Appendix, some remarks on the numerical schemes used in the DKES code and its applications are explained briefly.

A.1 Basic Equations

For a quasistatic magnetic configuration of interest in transport applications ($\partial B / \partial t \sim 0$ on the collision time scale), the evolution of the gyrophase angle ϕ independent part of the distribution function $f(\boldsymbol{x}, \boldsymbol{v}, t)$ is governed by the following conservative drift kinetic equation

$$\frac{\partial f}{\partial t} + \nabla \cdot (\boldsymbol{v}_g f) + \frac{1}{\sin \alpha} \frac{\partial}{\partial \alpha} (\sin \alpha \dot{\alpha} f) + \frac{1}{v^2} \frac{\partial}{\partial v} (v^2 \dot{v} f) = C(f, f). \qquad (A.1)$$

Here the notations are the same as those in Ref. [47] and (v, α, ϕ) are the spherical velocity space coordinates, where $v_{\parallel} = v \cos \alpha$ and α is the pitch angle, and are convenient for numerical computations.

For transport computations, expanding Eq. (A.1) about a local Maxwellian f_M and using the expansion of $\boldsymbol{B}$ on the magnetic coordinates yield the following steady state linear equation for f_1 (the perturbed distribution that results from small local departures from thermodynamic equilibrium)

$$\boldsymbol{v}_L \cdot \nabla f_1 + \dot{\alpha}_L \frac{\partial f_1}{\partial \alpha} + \dot{v}_L \frac{\partial f_1}{\partial v} - C(f_1) = D, \qquad (A.2)$$

with the same notations as in Ref. [47]. This conservative form is useful in establishing variational properties of the drift kinetic equation as described in the following.

A.2 Variational Principle

A variational principle for the thermodynamic fluxes is derived from the linearized equation (A.2), with $\dot{v}_L = 0$ which corresponds to the neglect of radial electric field. Since the DKES can treat the transition particle dynamics, a variational principle is required that is valid for all collisionalities.

It is convenient to recast Eq. (A.2) as follows

$$\hat{V}(g_1) - \hat{C}(g_1) = D, \qquad (A.3)$$

where $g_1 = f_1/f_M$, $\hat{V}(g_1) \equiv f_M V(g_1)$ and $\hat{C}(g_1) \equiv C(f_M g_1)$. The inner product is defined as

$$\{f, h\} \equiv 2\pi \int d(\cos\alpha) \int \langle fh \rangle v^2 dv, \qquad (A.4)$$

where the angle brackets indicate the surface-average. Noting the conservative nature of Eq. (A.2), it follows from integration by parts that

$$\hat{V} : \underline{\text{antisymmetric}} \text{ operator} \quad (\{f, \hat{V}(h)\} = -\{h, \hat{V}(f)\}),$$
$$\hat{C} : \underline{\text{symmetric}} \text{ operator} \quad (\{f, \hat{C}(h)\} = \{h, \hat{C}(f)\}).$$

Thus the total operator in Eq. (A.2) has no symmetry structure with respect to the inner product. To obtain a variational principle for such an equation, it is necessary to introduce the adjoint equation

$$-\hat{V}(h_1) - \hat{C}(h_1) = D^*. \qquad (A.5)$$

When D^* is chosen to satisfy $D^*(E_\parallel, \alpha) \equiv D(-E_\parallel, \pi - \alpha) = D(E_\parallel, \alpha)$, the adjoint equation has reversed orbits, where $E_\parallel$ is the surface-averaged electric field strength in the $\boldsymbol{B}$ direction.

To obtain equations with definite symmetry properties, the sum and difference distributions, $F^\pm$, are introduced

$$F^\pm \equiv (g_1 \pm h_1)/2. \qquad (A.6)$$

Adding and subtracting Eqs. (A.3) and (A.5) with $D^* = D$ yield

$$\begin{aligned}\hat{V}(F^-) - \hat{C}(F^+) &= D, \\ \hat{V}(F^+) - \hat{C}(F^-) &= 0.\end{aligned} \qquad (A.7)$$

After some calculations with these equations, the entropy production rate $\hat{S}$ is obtained as follows:

$$\hat{S} = 2\{F^+, \hat{V}(F^-)\} - \{F^+, \hat{C}(F^+)\} + \{F^-, \hat{C}(F^-)\} - 2\{F^+, D\}. \qquad (A.8)$$

Using the symmetry properties of $\hat{V}$ and $\hat{C}$, it follows that $\hat{S}$ is a variational quantity with respect to $F^\pm$ and attains its stationary value, $\hat{S}_* = -\{g_1, D\}$, when $F^\pm$ satisfy Eq. (A.7). This $\hat{S}_*$ can also be represented as

$$\hat{S}_* = \sum_{j=1}^{3} I_j A_j, \qquad (A.9)$$

where I_j are the thermodynamic fluxes conjugate to the forces A_j,

$$\begin{aligned}I_1 &\equiv \langle \boldsymbol{\Gamma} \cdot \nabla\rho \rangle &= -\sum_{n=1}^{3} L_{1n}A_n, \\ I_2 &\equiv \langle \boldsymbol{Q} \cdot \nabla\rho/T \rangle &= -\sum_{n=1}^{3} L_{2n}A_n, \\ I_3 &\equiv n\langle \boldsymbol{u} \cdot \boldsymbol{B} \rangle &= -\sum_{n=1}^{3} L_{3n}A_n.\end{aligned} \qquad (A.10)$$

Here, ρ is the label of the magnetic surface, $\boldsymbol{\Gamma} = \int \boldsymbol{v}_D f_1 d^3\boldsymbol{v}$ is the particle flux, $\boldsymbol{Q} = T \int \boldsymbol{v}_D K f_1 d^3\boldsymbol{v}$ is the heat flux and $n\boldsymbol{u} \cdot \boldsymbol{B} = B \int v_\parallel f_1 d^3\boldsymbol{v}$. The coefficient L_{ij} defined in Eq. (A.10) are elements of the Onsager transport matrix.

The relations $\frac{\delta\hat{S}}{\delta F^\pm} = 0$ together with Eq. (A.9) make up a variational principle for computing values of the transport matrix elements for all collision frequency regimes.

Since $\hat{C}$ is a negative operator, its inverse is well defined except for functions comprising the collisional invariants which are in the null space of $\hat{C}$. It is computationary efficient to consider the augmented negative definite operator, $\hat{C}_\epsilon = \hat{C} + \epsilon$, where $\epsilon \to 0^-$ has negative eigenvalues in the null space of $\hat{C}$. The operator $\hat{C}_\epsilon$ is rigorously invertible and the transport coefficients can be computed as the limit of a sequence corresponding to decreasing values of ϵ. Thus,

$$F^- = \hat{C}_\epsilon^{-1}\hat{V}(F^+) \qquad (A.11)$$

from the second equation of (A.7) and substituting this into the expansion for $\hat{S}$ yields the following quadratic form for F^+:

$$\hat{S}(F^+) = \lim_{\epsilon \to 0^-} [\{F^+, \hat{V}\hat{C}_\epsilon^{-1}\hat{V}(F^+)\} - \{F^+, \hat{C}(F^+)\} - 2\{F^+, D\}]. \qquad (A.12)$$

Since the operator $\boldsymbol{M} \equiv \hat{V}\hat{C}_\epsilon^{-1}\hat{V} - \hat{C}$ is positive definite, the extremal value of $\hat{S}$ obtained by varying F^+ corresponds to a minimum. Equation (A.12) is therefore an energy principle for determining the thermodynamic fluxes.

A.3 Fourier-Legendre Expansion of the Distribution Function

The variational distribution $F^\pm$ defined in Eq. (A.6) can be expanded in a Fourier-Legendre series as follows [47]

$$F^\pm = \sum_{i=1}^{3} A_i\{\sum_l p_l(\cos\alpha) \sum_{m,n} \sum_{\gamma=c,s} F_{imnl}^{\pm\gamma}(v)e_{mn}^\gamma(\theta, \zeta)\}. \qquad (A.13)$$

Here $0 \leq l \leq L$ (L is the maximum order in a truncated Legendre series approximation for $F^\pm$) and $\{p_l(x)\}$ are the orthonomalized Legendre polynomials. The $e^\gamma_{mn}(\theta, \zeta)$ are orthonomalized trigonometric functions ($\gamma = c : \cos$, $\gamma = s : \sin$). The resulting variational equations for the expansion coefficients in Eq. (A.13) are listed in Eqs. (26), (27) of Ref. [47]. In practice, they are solved for several different values of the radial electric field strength and of the collisionality to obtain F^γ_{imnl}. Then the transport coefficient L_{ij} can be expressed as

$$L_{ij} = \frac{2}{\sqrt{\pi}} \int_0^\infty K^{\frac{1}{2}} e^{-K} g_i g_j D_{ij}(K) dK , \qquad (A.14)$$

where $g_1 = g_3 = 1$, $g_2 = K$ ($K = \dfrac{mv^2}{2T}$: normalized kinetic energy) and $D_{ij}(K)$ is the velocity dependent diffusion coefficient (cf., Eq. (30b) of Ref. [47]).

A.4 Numerical Scheme

An appropriate analysis of the eigenvalue structure of Eq. (A.7) can be made by considering scalar models for the operators $\hat{V}(F^\pm) \sim \pm\omega_b F^\pm$ and $\hat{C}(F^\pm) \sim -\nu_{eff} F^\pm$. If $dF^\pm/dt$ is retained in Eq. (A.7), the resulting temporal eigenvalues are $-\nu_{eff} \pm i\omega_b = -\nu_{eff}(1 \pm i/\nu_*)$. Thus in the low collision frequency regimes of interest ($\nu_* \ll 1$), the explicit numerical integration of the underdamped system in Eq. (A.7) converges only very slowly toward a steady state solution.

The convergence rate of the explicit temporal integration scheme can be substantially improved by using the energy principle for $F^\pm$, Eq. (A.12), as the basis for a conjugate minimization method. This method, which generalizes the steepest descent technique, finds the quadratic minimum of $\hat{S}$ along search directions which are given as appropriate combinations of the local gradients $g(F^+) \equiv MF^+ - D$.

The conjugate gradient scheme is much more efficient at all collision frequencies than explicit temporal integration. One reason for this improved efficiency is that the eigenvalue spectrum exist in the complex plane.

The main attribute of the conjugate gradient method is the relatively small storage requirement compared with the direct matrix inversion techniques. However, the tridiagonal structure of the variational equations ($A^\gamma_{imnl} = 0$, cf., Eq. (26) of Ref. [47]) with respect to the Legendre index l may be exploited to efficiently invert these equations with minimal storage. A block-

tridiagonal solver seems to be considerably faster in the low collision frequency regimes than the unpreconditioned conjugate gradient method with a computation time that is nearly independent of ν_{eff}/ω_b.

A.5 Application of the DKES code

The DKES code has been applied to study neoclassical transport properties, particle diffusion and bootstrap coefficients, of helical axis configurations in this thesis. Since the DKES code is based on the Boozer coordinates, it is necessary to have the magnetic field quantities such as the poloidal and toroidal flux profiles and the Fourier spectrum of the field strength in the Boozer coordinates for the input data. These quantities can be obtained by transforming the MHD equilibrium calculated in the VMEC coordinates to the Boozer coordinates.

Figures A.1 show the results of the convergence study of diffusion coefficient with respect to (a) Fourier mode number with 100 Legendre polynomials and (b) Legendre polynomials with 465 Fourier modes for the case of $\nu_* \sim 1.5 \times 10^{-2}$ without radial electric field. It is clearly seen from Fig. A.1(a) that more than 300 Fourier modes are necessary to obtain sufficient convergence and from Fig. A.1(b) that the number of Legendre polynomials has little effect on the convergence if the sufficient number of Fourier modes are used. Therefore, 100 Legendre polynomials and 465 Fourier modes for distribution functions have been used to study neoclassical transport properties of helical axis configurations in this thesis. The transport coefficients are obtained with sufficient accuracy for the parameter regime of $\nu_* > 10^{-2}$; however, it has been difficult to obtain good convergence in the regime of $\nu_* < 10^{-2}$. In those cases, the upper and lower values from variational principles are averaged to have the approximate transport coefficients. In Ref. [112], the same behavior has appeared and the diffusion coefficients are extrapolated by assuming a $1/\nu$ or ν variation expected by the neoclassical transport theory.

When an equivalent tokamak is considered, Fourier components of the magnetic field strength for a helical axis stellarator is manipulated in the code so that the toroidal component in the magnetic spectrum becomes the same as the geometrical inverse aspect ratio of the specified magnetic surface with keeping the rotational transform and field strength averaged along the magnetic axis. As for the "$B_{04} = 0$" case in Figs. 3.19 and 3.21, only B_{04}

component is set to zero in the code with keeping all other input data. It is noted that this elimination of the bumpy field component does not change the average magnetic field strength on the magnetic axis. Thus, the DKES code is useful to study the effect of each component of the magnetic field spectrum on the neoclassical transport separately.

Recently, the DKES code has been applied to study the neoclassical transport in the low aspect ratio tokamak [113] in which the magnetic field strength can not be represented simply by $B = B_0(1 - \epsilon_t \cos\theta)$ since $\epsilon_t \sim 1$. Therefore, Fourier components corresponding to higher poloidal mode numbers are included. It is noted that effects of the magnetic field ripple due to the finite number of toroidal coils on the neoclassical transport properties in conventional tokamaks can also be investigated by the DKES code.
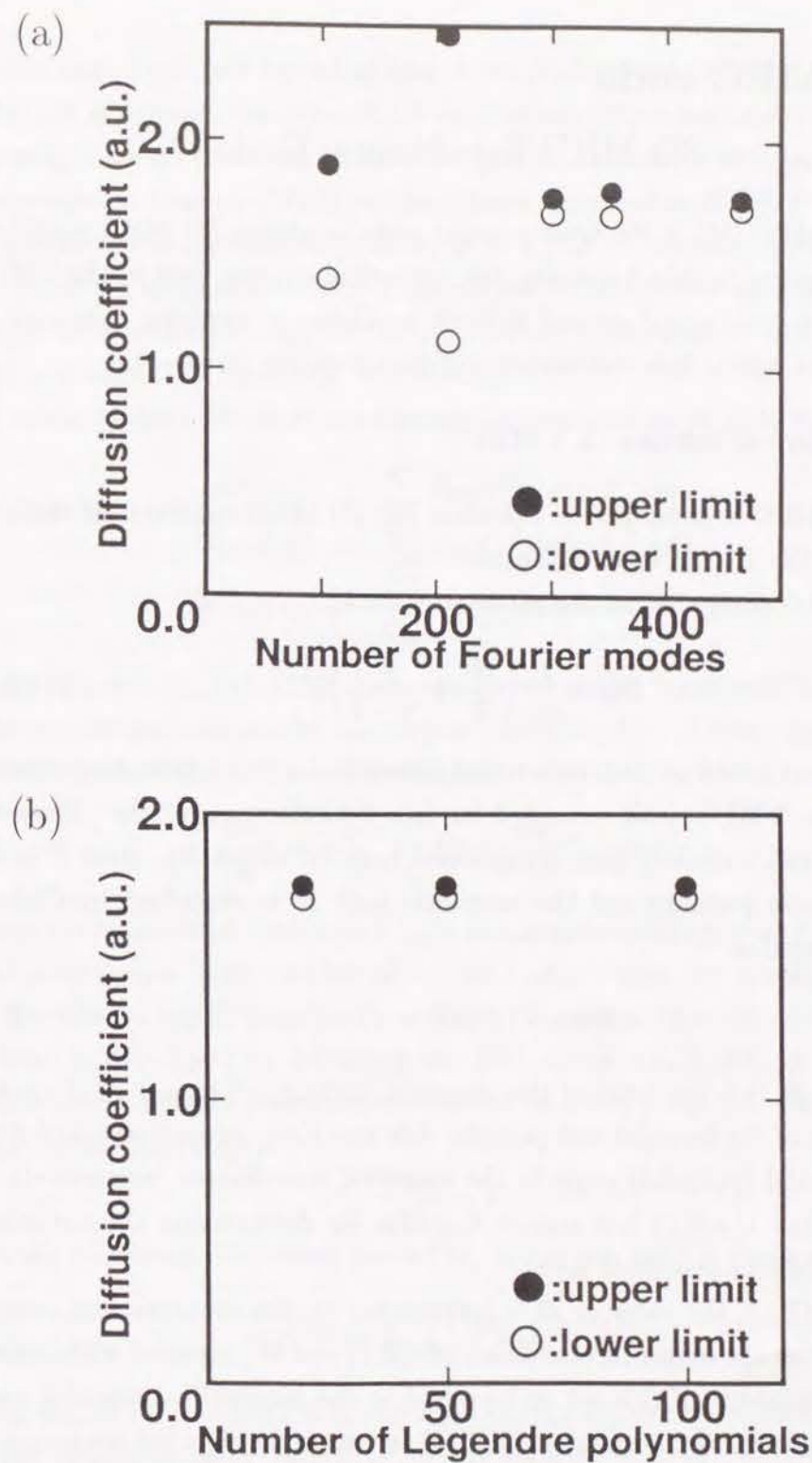

Fig. A.1: Convergence study of diffusion coefficient for optimized helical axis configuration with respect to (a) Fourier modes and (b) Legendre polynomials in the DKES code.

B VMEC code

— 3D MHD Equilibrium Code —

The VMEC [59] is the most popular code to obtain 3D MHD equilibria for stellarators. In this Appendix, the numerical scheme used in the VMEC is explained briefly and several difficult problems in applying this code to equilibria of helical axis stellarator configurations are discussed.

B.1 Numerical scheme in VMEC

The VMEC is developed to calculate the 3D MHD equilibria of stellarators using the inverse spectral method.

The total energy W_p in the plasma region V_p,

$$W_p = \int_{V_p} \left(\frac{B^2}{2} + \frac{P}{\gamma - 1} \right) dV , \qquad (B.1)$$

is minimized based on the variational principle for fixed boundary equilibria. In the VMEC, it is extended for free boundary equilibria. However, only the fixed boundary case is explained here for simplicity. Here P is the scalar plasma pressure and the magnetic field B is described by Clebsch representation as

$$B = \nabla s \times \nabla(\psi'(s)\theta - \chi'(s)\zeta + \lambda) , \qquad (B.2)$$

where $s \in [0, 1]$ is the label of the magnetic surface, $\psi'(s)$ and $\chi'(s)$ are the derivatives of the toroidal and poloidal flux function, respectively, and θ (ζ) is the toroidal (poloidal) angle in the magnetic coordinates, respectively. It is noted that $\lambda(s, \theta, \zeta)$ is a stream function for determining the optimized poloidal angle as described later.

In Eq. (B.1), the value of B is represented by the contravariant components of B on the magnetic coordinates (s, θ, ζ) and W_p is varied with respect to these variables. If ζ is set to be equal to the geometrical toroidal angle ϕ in the cylindrical coordinates (R, Z, ϕ) for example, it is not necessary to vary W_p with respect to ϕ. Here R (Z) is the radial (vertical) variable. Then, from Eq. (B.1), the first variational form of W_p,

$$\delta W_p = -\int_{V_p} F \cdot \delta x \, ds d\theta d\zeta \qquad (B.3)$$

is obtained. It should be noted that $x = (R, Z, \lambda)$ not (R, Z, ϕ). From Eq. (B.3), it is obvious that the MHD equilibrium which satisfies $\delta W_p = 0$ is given by $F = \mathbf{o}$. It can be shown that the condition $F = \mathbf{o}$ is equivalent to the condition that the MHD residual force $\hat{F} = -J \times B + \nabla P$ is exactly zero, where J is the current given by $J = \nabla \times B$. Therefore, in the VMEC, the following numerical scheme is developed to obtain the solution x in the region of V_p corresponding to the equilibrium configuration which satisfies $\delta W_p = 0$ instead of solving $\hat{F} = \mathbf{o}$ directly.

In the VMEC, (R, Z, λ) are Fourier decomposed on (θ, ζ) as follows:

$$
\begin{aligned}
R(s, \theta, \zeta) &= \sum_{mn} R_{mn}(s) \cos(m\theta - n\zeta) , \\
Z(s, \theta, \zeta) &= \sum_{mn} Z_{mn}(s) \sin(m\theta - n\zeta) , \\
\lambda(s, \theta, \zeta) &= \sum_{mn} \lambda_{mn}(s) \cos(m\theta - n\zeta) ,
\end{aligned}
\qquad (B.4)
$$

where $[R_{mn}(s), Z_{mn}(s), \lambda_{mn}(s)]$ are considered as the "moments" of (R, Z, λ) that are determined on the discretized radial meshes. Using these Fourier representations, Eq. (B.3) can be written as

$$\frac{dW_p}{dt} = -\sum_{mn} \int_{V_p} F_{mn}^* \cdot \frac{\partial x_{mn}}{\partial t} ds d\theta d\zeta , \qquad (B.5)$$

where t is an artificial time and F_{mn}^* is the complex conjugate of F_{mn}. In 3D configurations, a large number of moment amplitudes are usually required to describe an equilibrium with sufficient accuracy. An efficient iteration method is developed by following the path along which dW_p/dt decreases with a maximum rate (the steepest descent method) [114]. The descent path equation for Eq. (B.5) is

$$\frac{\partial x_{mn}}{\partial t} = F_{mn} \qquad (B.6)$$

and the maximum decreasing rate of W_p along this path is given by

$$\frac{dW_p}{dt} = -\sum_{mn} \int_{V_p} |F_{mn}|^2 ds d\theta d\zeta . \qquad (B.7)$$

From Eq. (B.7), it is clear that the total energy W_p decreases monotonously to the minimum value according to the solution x_{mn} of Eq. (B.6). Since the first order differential equation (B.6) is not easy to solve with sufficient numerical stability, the second order equation

$$\frac{\partial^2 x_{mn}}{\partial t^2} + \frac{1}{\tau} \frac{\partial x_{mn}}{\partial t} = F_{mn} \qquad (B.8)$$

is solved in the code, which is called the second order Richardson scheme. The parameter $\tau > 0$ has little effect on the stability of the numerical scheme and can therefore be chosen to maximize the decay rate of the least-damped mode of Eq. (B.8), thereby minimizing the number of iterations required to reach the steady state. The optimum value for τ, leading to the critical damping in Eq. (B.8), is [115]

$$\frac{1}{\tau_{op}} = -\frac{d}{dt}\left(\ln\sum_{mn}\int_{V_p}|\boldsymbol{F}_{mn}|^2 dsd\theta d\zeta\right). \tag{B.9}$$

The distinguished feature of the VMEC among several 3D MHD equilibrium codes is the optimization of the poloidal angle representation. In general, the spectral width with respect to the poloidal angle becomes wide when the beta value is increased, which may degrade the numerical accuracy and convergence. To resolve this problem, an optimization procedure is developed for accelerating the convergence of the Fourier series for R and Z in Eq. (B.4) [114]. Let $S_p(m) \equiv m^p \sum_n (R_{mn}^2 + Z_{mn}^2)$ be the power spectrum of the magnetic surface, where $p \geq 0$. Then define a q moment of $S_p(m)$ as follows:

$$\langle M(p,q)\rangle = \frac{\displaystyle\sum_{m\geq 1} m^q S_p(m)}{\displaystyle\sum_{m\geq 1} S_p(m)}. \tag{B.10}$$

For $q > 0$, $\langle M \rangle$ is a qualitative measurement of the spectral width with a smaller $\langle M \rangle$ corresponding, in general, to a more condensed power spectrum.

The minimization of $\langle M \rangle$ will determine a family of constraints between R_{mn} and Z_{mn} (depending on p and q) leading to the condensed Fourier spectrum for R and Z.

In MHD equilibrium theory, the closed contours $H(R, Z, \phi) = H_0$ represent the level surfaces of the magnetic flux function or the magnetic surfaces. Therefore, the variations of R_{mn} and Z_{mn} in Eq. (B.10) are coupled so that $\delta H = H_R \delta R + H_Z \delta Z = 0$. Since $dH/d\theta = H_R R_\theta + H_Z Z_\theta = 0$ on the magnetic surface, these relations imply $\delta R = R_\theta \delta u$ and $\delta Z = Z_\theta \delta u$, where u is an unconstrained variation. Thus from Eq. (B.4),

$$\begin{aligned}\delta R_{mn} &= \oint \cos(m\theta - n\zeta)R_\theta \delta u d\theta d\phi\,,\\ \delta Z_{mn} &= \oint \sin(m\theta - n\zeta)Z_\theta \delta u d\theta d\phi\,.\end{aligned} \tag{B.11}$$

Then, the constrained variation of $\langle M \rangle$ in Eq. (B.10) satisfies

$$\delta\langle M\rangle \cdot \sum_{m\geq 1} S_p(m) = 2\int I(\theta,\phi)\delta u d\theta d\zeta\,, \tag{B.12}$$

where

$$\begin{aligned}I(\theta,\phi) &= X(\theta,\phi)R_\theta + Y(\theta,\phi)Z_\theta\,,\\ X(\theta,\phi) &= \sum_{m\geq 1,n} f(m)R_{mn}\cos(m\theta - n\zeta)\,,\\ Y(\theta,\phi) &= \sum_{m\geq 1,n} f(m)Z_{mn}\sin(m\theta - n\zeta)\,,\end{aligned} \tag{B.13}$$

and $f(m) = m^p(m^q - M)$. The minimum value of $\langle M \rangle$ consistent with a fixed curve geometry is therefore determined by the constraint $I(\theta,\phi) = 0$.

Since $\langle M \rangle \geq 1$ is positive definite and Eq. (B.12) results from the variation of $\langle M \rangle$, it is possible to use a descent path algorithm to solve the equation $I = 0$. Indeed, if $\delta u \sim -I$ is used to iterate R_{mn} and Z_{mn} according to Eq. (B.11), then $\delta\langle M\rangle \sim -\int I^2 d\theta d\zeta$ will decrease monotonously toward the desired solution $I = 0$. Let the descent path equations can be written as

$$\frac{\partial x_{imn}}{\partial t} = (F_i^{con})_{mn} \quad (i = R, Z)\,, \tag{B.14}$$

where $\{(F_i^{con})_{mn}\}$ denote Fourier components of the artificial force to minimize poloidal Fourier modes.

The exponents p and q appearing in Eq. (B.10) should be as large as possible to suppress any spurious high-m spectral components of R and Z. If, however, p and q are too large, the computational effort becomes overwhelming. Since the eigenvalues introduced into the force equations by I scale approximately as M^{p+q}, it is advisable to fix $p + q \equiv Q$ at some reasonable value. It has been found that the choice $q = 1$ and $p = Q - 1$ always leads to the most rapid decay of the power spectrum with respect to the poloidal mode number.

The VMEC finally gives the equilibrium Fourier moments $\boldsymbol{x}_{mn} = (R_{mn}, Z_{mn}, \lambda_{mn})$ corresponding to

$$\begin{aligned}\hat{F}_{imn} &= (F_i + F_i^{con})_{mn} = 0 \quad (i = R, Z)\,,\\ \hat{F}_{\lambda mn} &= 0\,,\end{aligned} \tag{B.15}$$

with the optimized poloidal angle.

B.2 Application of the VMEC to Helical Axis Configurations

The fixed boundary version of the VMEC is employed to study finite beta currentless equilibria of helical axis stellarator configurations in this thesis. But there are some problems in connection with the complicated geometry of these configurations.

The first problem is a time consuming computation. For magnetic surfaces of conventional stellarator about 50 Fourier modes are sufficient to describe their shapes precisely. However, in the helical axis configurations, shapes of the magnetic surfaces changes significantly in both the poloidal and toroidal directions. Therefore, much larger number of Fourier modes, for example, about 300 modes are necessary, which means a time consuming computation.

The second is related to the input data. It is standard to input only the set of Fourier modes of the outermost magnetic surface to the VMEC to construct the initial guess configuration, from which the iteration is started. However, in applying the VMEC to helical axis configurations, sometimes there appear the negative sign of the Jacobian. This is probably due to the intersection or overlapping of the magnetic surfaces obtained by the interpolation based on neighboring radial grids. In order to avoid this difficulty, a better initial guess is needed. Therefore, sets of Fourier modes describing the several vacuum magnetic surfaces are also prepared to improve the interpolation. It is noted that these magnetic surfaces do not intersect each other.

At first, these data are interpolated to obtain the Fourier data of the surfaces corresponding to the VMEC radial grids with the constant interval of the toroidal flux function. But sometimes there still appears intersection of magnetic surfaces especially for the bean shaped surfaces. In this case, the other method is applied. By interpolating the toroidal flux function obtained from the line tracing code first, the magnetic surfaces corresponding to the VMEC radial grids are selected. It is noted again that these magnetic surfaces do not intersect each other. Then they are Fourier decomposed and the initial data of Fourier modes is obtained. The first calculation is done with a coarse grid points (for example, grid number $NS = 7$) to obtain more accurate initial data set. Finally, with this initial configuration, the calculation is started again with a finer radial grid points such as $NS = 41$.

The third is about the numerical convergence. As explained in the previous section, the equilibrium solution is obtained at $\int_{V_p} |F_{mn}|^2 dV = 0$ or $dW_p/dt = 0$ by solving the descent path equation in the VMEC. For planar axis stellarator configurations, it has been possible to reach $\int_{V_p} |F_{mn}|^2 dV \sim 10^{-12}$ easily as the equilibrium state. However, in the case of helical axis

configurations such as discussed in this thesis, $\int_{V_p} |F_{mn}|^2 dV$ typically behaves as shown in Fig. B.1. But before the onset of oscillatory behavior, W_p decreases monotonously along the descent path equations (B.8). The monotonous fall off of W_p may be considered as the approach to the equilibrium state and the end point of this fall off ($\times$ point in Fig. B.1) may correspond to the equilibrium state. The above mentioned problems have also occured in the application of the VMEC to the H-1 Heliac in Australian National University [116].
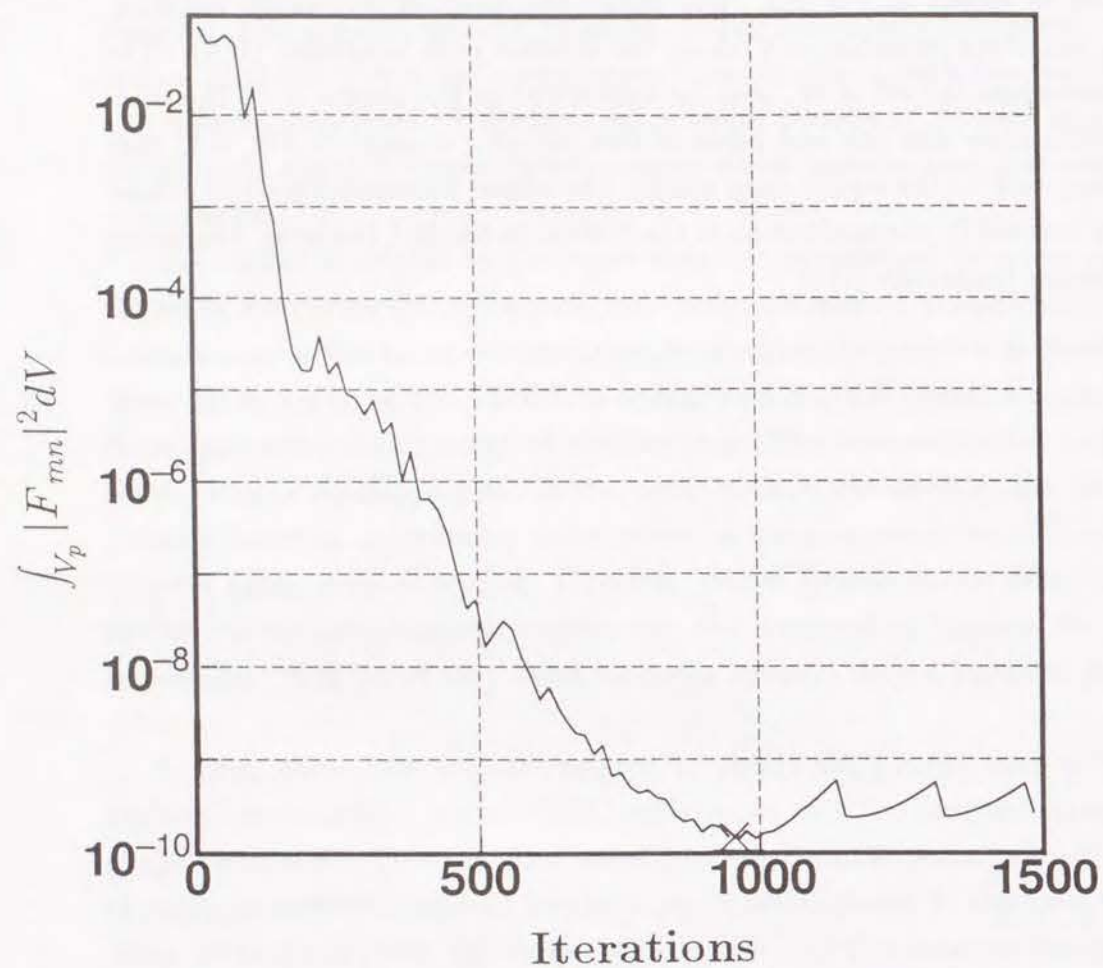
Fig. B.1: Typical behavior of $\int_{V_p} |\boldsymbol{F}_{mn}|^2 dV$ in the application of the VMEC to helical axis configurations.

C A Model of the L-H Transition

The poloidal momentum balance equation is

$$\frac{d}{dt}(NM_i\langle \boldsymbol{B}_p \cdot \boldsymbol{u}\rangle) = \frac{1}{c}(\boldsymbol{J} \times \boldsymbol{B} \cdot \boldsymbol{B}_p) - \langle \boldsymbol{B}_p \cdot \nabla \cdot \boldsymbol{\Pi}\rangle - \frac{e}{c}\boldsymbol{\Gamma}_{orbit} \times \boldsymbol{B} \cdot \boldsymbol{B}_p, \quad \text{(C.1)}$$

where $\boldsymbol{u}$ is the flow velocity, $\boldsymbol{\Gamma}_{orbit}$ is the viscosity driven particle flux associated with the ion orbit loss and $\boldsymbol{J}$ is the plasma current which depends on $\partial E_r/\partial t$. Here E_r is the radial electric field. It is noted that the electron contribution to poloidal momentum, poloidal viscosity and orbit loss are neglected in Eq. (C.1). At steady state,

$$-\frac{e}{c}\boldsymbol{\Gamma}_{orbit} \times \boldsymbol{B} \cdot \boldsymbol{B}_p = \langle \boldsymbol{B}_p \cdot \nabla \cdot \boldsymbol{\Pi}\rangle. \quad \text{(C.2)}$$

A physical interpretation of Eq. (C.2) is that the ion orbit loss of high energy particles drives a poloidal torque; however, low energy particles contribute to the poloidal viscosity and resist poloidal rotation. The solution of Eq. (C.2) describing the equilibrium poloidal flow velocity depends sensitively on poloidal viscosity. When the poloidal viscosity as a function of poloidal flow velocity has a local maximum, there are two possible solutions, as shown in Ref. [94]. One is the lower flow velocity solution and the other has a higher flow velocity than that corresponding to the local maximum of the poloidal viscosity. It is considered that the former with $M_p \lesssim 1$ is the L mode and the latter with $M_p \gtrsim 1$ is the H mode. An equivalent argument based on a different interpretation is also derived in Ref. [117].

References

[1] OKAMURA, S., et al., Nucl. Fusion 35(1995)283.

[2] STRAIT, E. J., Phys. Rev. Lett. 74(1995)2483.

[3] SUDO, S.,et al., Nucl. Fusion 30(1990)11.

[4] LACKNER, K., GOTTARDI, N. A. O., Nucl. Fusion 30(1990)767.

[5] PERKINS, F. W., et al., Phys. Fluids B5(1993)477.

[6] STROTH, U., et al., NIFS Report 375, National Institute for Fusion Science, Japan (1995).

[7] UO. K., et al., in Plasma Physics and Controlled Nuclear Fusion Research 1980 (Proc. 8th Int. Conf. Brussels, 1980), Vol.1, IAEA, Vienna (1981)217.

[8] NISHIMURA, K., et al., Fusion Technol. 17(1990)86.

[9] LYON, J. F., et al., Fusion Technol. 10(1986)179.

[10] W7-A Team, in Plasma Physics and Controlled Nuclear Fusion Research 1976 (Proc. 6th Int. Conf. Berchtesgaden, 1976), Vol.2, IAEA, Vienna (1977)81.

[11] RENNER, H., et al., Plasma Phys. Control. Fusion 31(1989)1579.

[12] TREFFERT, J. D., et al., Phys. Rev. Lett. 53(1984)2409.

[13] IIYOSHI, A., et al., Fusion Technol. 17(1990)169.

[14] GRIEGER, G., et al., Phys. Fluids B4(1992)2081.

[15] NÜHRENBERG, J., ZILLE, R., Phys. Lett. A129(1988)113.

[16] ANDERSON, D. T., GARABEDIAN, P. R., Nucl. Fusion 34(1994)881.

[17] YOKOYAMA, M., NAKAMURA. Y., WAKATANI. M., in Plasma Physics and Controlled Nuclear Fusion Research 1994 (Proc. 15th Int. Conf. Seville, 1994), Vol.2, IAEA, Vienna (1995)345.

[18] YOKOYAMA, M., NAKAMURA. Y., WAKATANI. M., submitted to Nucl. Fusion.

[19] ASDEX Team, Nucl. Fusion 29(1989)1959.

[20] GROEBNER, R. J., Phys. Fluids B5(1993)2343.

[21] WAGNER, F., et al., Plasma Phys. Control. Fusion 36(1994)A61.

[22] TOI, K., et al., in Plasma Physics and Controlled Nuclear Fusion Research 1992 (Proc. 14th Int. Conf. Würzburg, 1992), Vol.2, IAEA, Vienna (1993)461.

[23] GROEBNER, R. J., et al., Phys. Rev. Lett. 64(1990)3015.

[24] IDA, K., et al., Phys. Rev. Lett. 65(1990)1364.

[25] TAYLOR, R. J., Phys. Rev. Lett. 63(1989)2365.

[26] WEYNANTS, R. R., TAYLOR, R. J., Nucl. Fusion 30(1990)945.

[27] YOKOYAMA. M., WAKATANI. M., SHAING, K. C., Nucl. Fusion 35(1995)153.

[28] LOTZ, W., NÜHRENBERG, J., Phys. Fluids 31(1988)2984.

[29] MAASSBERG, H., et al., Phys. Fluids B5(1993)3728.

[30] GARABEDIAN, P. R., GARDNER, H. J., Phys. Plasmas 2(1995)2020.

[31] LOTZ, W., et al., Plasma Phys. Control. Fusion 34(1992)1037.

[32] ANDERSON, D. T., et al., HSX — A Helically Symmetric Toroidal Experiment — (edited by Torsatron/Stellarator Laboratory, Univ. of Wisconsin-Madison) (1993).

[33] CALLEN, J. D., private communication (1993).

[34] SHAING, K. C., et al., Phys. Fluids 29(1986)521.

[35] MERKEL, P., Nucl. Fusion 27(1987)867.

[36] DOMMASCHK, W., Comput. Phys. Commun. 40(1986)203.

[37] TALMADGE, J. N., private communication (1995).

[38] CATTO, P. J., HAZELTINE, R. D., Phys. Fluids **24**(1981)1663.

[39] BERNARDIN, M. P., et al., Phys. Fluids **29**(1986)2605.

[40] GALEEV, A. A., SAGDEEV, R. Z., Reviews of Plasma Physics, Vol.7, Consultants Bureau, New York (1975)p.257.

[41] WAKATANI, M., et al., Nucl. Fusion **21**(1981)175.

[42] MYNICK, H. E., Phys. Fluids **26**(1983)2609.

[43] BOOZER, A. H., Phys. Fluids **23**(1980)904.

[44] FOWLER, R. H., et al., Phys. Fluids **28**(1985)338.

[45] SHAING, K. C., HOKIN, S. A., Phys. Fluids **26**(1983)2136.

[46] MYNICK, H. E., et al., Phys. Rev. Lett. **48**(1982)322.

[47] HIRSHMAN, S. P., et al., Phys. Fluids **29**(1986)2951.

[48] SHAING, K. C., et al., Phys. Fluids **B1**(1989)148.

[49] RENNER, H., et al., in Plasma Physics and Controlled Nuclear Fusion Research 1990 (Proc. 13th Int. Conf. Washington, DC, 1990), Vol.2, IAEA, Vienna (1991)439.

[50] MURAKAMI, M., et al., in Plasma Physics and Controlled Nuclear Fusion Research 1990 (Proc. 13th Int. Conf. Washington, DC, 1990), Vol.2, IAEA, Vienna (1991)455.

[51] BEIDLER, C. D., et al., Nucl. Fusion **30**(1990)405.

[52] BOOZER, A. H., et al., Phys. Fluids **24**(1981)851.

[53] WAKATANI, M., NAKAMURA, Y., ICHIGUCHI, K., Nucl. Eng. and Design **15**(1992)395.

[54] JOHNSON, J. L., et al., Phys. Fluids **1**(1958)281.

[55] ANANIA, G., et al., Phys. Fluids **26**(1983)2210.

[56] SHAFRANOV, V. D., Sov. Phys. JETP **6**(1957)545.

[57] JOHNSON, J. L., et al., J. Comput. Phys. **32**(1979)212.

[58] BAUER, F., BETANCOURT, O., GARABEDIAN, P. R., Magnetohydrodynamic Equilibrium and Stability of Stellarators (Springer-Verlag, New York, 1984)

[59] HIRSHMAN, S. P., et al., Comput. Phys. Commun. **43**(1986)143.

[60] GRAD, H., Phys. Fluids **10**(1967)137.

[61] HAYASHI, T., et al., Phys. Fluids **B4**(1992)1539.

[62] REIMAN, A. H., GREENSIDE, H. S., Comput. Phys. Commun. **43**(1986)157.

[63] JOHNSON, J. L., private communication (1994).

[64] MERKEL, P., 9th IAEA International Workshop on Stellarators, Garching (1993).

[65] SUGAMA, H., WAKATANI, M., J. Phys. Soc. Jpn. **58**(1989)1128.

[66] DOMINGUEZ, N., et al., Nucl. Fusion **29**(1989)2079.

[67] MERCIER, C., Nucl. Fusion **1**(1960)47.

[68] VARIAS, A., et al., Nucl. Fusion **30**(1990)2597.

[69] ALEJALDRE, C., et al., Fusion Technol. **17**(1990)131

[70] NÜHRENBERG, J., et al., Plasma Phys. Control. Fusion **35**(1993)B115.

[71] GARDNER, H. J., BLACKWELL, D. B., Nucl. Fusion **32**(1992)2009.

[72] MOECKLI, R., COOPER, W. A., Nucl. Fusion **33**(1993)1899.

[73] NÜHRENBERG, J., ZILLE, R., in Theory of Fusion Plasmas (Proc. Workshop Varenna, 1987) Editrice Compositori, Bologna (1987)3.

[74] NAKAMURA, Y., WAKATANI, M., ICHIGUCHI, K., J. Plasma Phys. and Fusion Research **69**(1993)41.

[75] ICHIGUCHI, K., private communication (1996).

[76] OHYABU, N., et al., Nucl. Fusion 34(1994)387.

[77] WAGNER, F., et al., Phys. Rev. Lett. 49(1982)1408.

[78] NÜHRENBERG, J., et al., 6th Int. Toki Conf. for Plasma Physics and Controlled Fusion 1994, Transactions of Fusion Technology, 27(1995)71.

[79] SOLOV'EV, L. S., SHAFRANOV, V. D., Reviews of Plasma Physics, Vol.5, Consultants Bureau, New York (1970)p.1.

[80] YOSHIKAWA, S., Nucl. Fusion 23(1983)667.

[81] GARABEDIAN, P. R., private communication (1993).

[82] SYDNEY, M., et al., Fusion Technol. 17(1990)123

[83] ICHIGUCHI, K., NAKAJIMA, N., GARDNER, H. J., to be published in Nucl. Fusion (1996).

[84] CARRERAS, B. A., et al., Nucl. Fusion 28(1988)1195.

[85] KATO, A., NAKAMURA. Y., WAKATANI, M., J. Phys. Soc. Jpn. 60(1991)494.

[86] HANATANI, K., PENNINGSFELD, F, -P., Nucl. Fusion 32(1992)1769.

[87] SOLANO, E. R., et al., Nucl. Fusion 28(1988)157.

[88] KIKUCHI, M., et al., Nucl. Fusion 30(1990)343.

[89] KIKUCHI, M., AZUMI, M., Plasma Phys. Control. Fusion 37(1995)1215.

[90] SHAING, K. C., et al., Phys. Fluids B1(1989)1663.

[91] SHAING, K. C., CALLEN, J. D., Phys. Fluids 26(1983)3315.

[92] ZUSHI, H et al., Nucl. Fusion 28(1988)433.

[93] RITZ, C. P., et al., in Plasma Physics and Controlled Nuclear Fusion Research 1990 (Proc. 13th Int. Conf. Washington, 1990), Vol.2, IAEA, Vienna (1991)589.

[94] SHAING, K. C., CRUME, E. C. Jr., Phys. Rev. Lett. 63(1989)2369.

[95] SHAING, K. C., et al., Phys. Fluids B2(1990)1492.

[96] ITOH, K., ITOH, S. -I., Nucl. Fusion 32(1992)2243.

[97] BERK, H. L., MOLVIG, K., Phys. Fluids 26(1983)1385.

[98] HASEGAWA, A., WAKATANI, M., Phys. Rev. Lett. 59(1987)1581.

[99] HASSAM, A. B., et al., Phys. Rev. Lett. 66(1991)309.

[100] SAPPER, J., RENNER, H., Fusion Technol. 17(1990)62.

[101] BEIDLER, C., et al., Fusion Technol. 17(1990)148.

[102] ERCKMANN, V., et al., Phys. Rev. Lett. 70(1993)2086.

[103] HAZELTINE, R. D., WARE, A. A., Plasma Phys. 20(1978)673.

[104] SHAING, K. C., Phys. Fluids B2(1990)2847.

[105] CORONADO, M., WOBIG, H., Phys. Fluids 29(1986)527.

[106] HIRSHMAN, S. P., SIGMER, D. J., Nucl. Fusion 21(1976)1079.

[107] SHAING, K. C., Phys. Fluids B5(1993)3841.

[108] CORONADO, M., GALINDO TREJO, J., Phys. Fluids B2(1990)530.

[109] CORONADO, M., TALMADGE, J. N., Phys. Fluids B5(1993)1200.

[110] SHAING, K. C., Plasma Phys. Control. Fusion 36(1994)A75.

[111] SHAING, K. C., private communication (1996).

[112] OGAWA, Y., et al., Nucl. Fusion 32(1992)119.

[113] SHAING, K. C., YOKOYAMA, M., WAKATANI, M., HSU, C. T., Phys. Plasmas 3(1996)965.

[114] HIRSHMAN, S. P., WHISTON, J. C., Phys. Fluids 26(1983)3553.

[115] GARABEDIAN, P. R., Math. Tables Aids Comput. 10(1956)183.

[116] GARDNER, H. J., private communication (1993).

[117] STRINGER, T. E., Nucl. Fusion 33(1993)1249.